Colloidal Crystals on Conical Surfaces

GERRAND, ADAM,FINLAY

A Thesis submitted for the Degree of

MSc by Thesis in Physics

Colloidal Crystals on Conical Surfaces

Adam Finlay Gerrand

Soft Matter Theory Group

Professor Halim Kusumaatmaja and Dr Mark Miller

Department of Physics

Durham University

September 2021

MSc by Thesis in Physics

Colloidal Crystals on Conical Surfaces

Adam Finlay Gerrand

Abstract

The curvature of surfaces affects the organisation of condensed matter upon them. In biology, the curvature of cell membranes affects how proteins are arranged within them and the growth of virus capsids is affected by their curvature, for example. Curvature is also used to guide colloidal self-assembly in industrial nanoscale manufacturing processes, to produce, among other things, drug delivery systems, biosensors and photonic crystals.

An open question in the field concerns how two-dimensional crystalline systems deal with the closure constraint imposed by finite curved surfaces. A crystal on a conical surface is a good model for studying this as the curvature strain associated with surfaces of non-zero Gaussian curvature is eliminated and the closure constraint is variable, unlike on, for example, cylindrical surfaces. In this work, putative global minimum energy structures of two-dimensional, model colloidal crystals confined on conical surfaces of a range of angles are generated using basin-hopping and visualised with Voronoi tessellation. The colloidal particles interact via an isotropic Morse potential. The defect patterns observed in these model, minimum energy crystals are discussed and analysed. The interparticle potential range and the cone angle affect whether any defects are seen in the minimum energy structures, and, if defects are produced, what they are. Both wedge-shaped defects reported in experiment and novel bulk-terminating helical defects are observed. At small cone angles, the type of defect is very sensitive to changes in angle, as different defects can alleviate different amounts of strain. A phase diagram of preferred defect type against cone angle and interparticle potential range is produced for near-cylindrical conical surfaces. Another interesting feature of the crystal is the vertical position on the cone that it prefers to occupy; a preliminary line energy model is constructed which explains this behaviour qualitatively.

Acknowledgements

Many thanks to my supervisors, Professor Halim Kusumaatmaja and Dr Mark Miller, for the opportunity and of course for all their time this year. Their help and patience has been invaluable, both within the bounds of this project and beyond. In such strange times, they have been willing to help me out at the drop of a hat. It was fantastic to meet Mark for the first time at the conclusion of the project!

Thank you to Jack Law, whose work I continued and whose guidance was much appreciated, especially in the early part of the year.

I would also like to thank Professor Vinothan Manoharan and Jessica Sun of Harvard University for their contributions and the constructive discussions we had.

And thank you lastly to my family, who have put up with twelve months of a full time masters student working all over the house, including, unhelpfully, during a complex house move to the other end of the country!

Contents

1. Introduction

This thesis aims to add to the existing body of knowledge on the effect of confining curved surfaces on the organisation of condensed matter. In particular, the effect of conical surfaces on the ground state configurations of colloidal crystals is investigated. Colloidal systems lend themselves well to computational modelling, and here minimum energy configurations of colloidal crystals on confining conical surfaces are investigated using global energy minimisation techniques.

In this introductory chapter, curvature and colloidal systems will be discussed and an overview of colloidal systems confined upon spherical, cylindrical and other curved surfaces will follow. The chapter will conclude with an outline of the structure of the rest of the thesis.

1.1 Curvature

1.1.1 Curvature in Biology and Materials Science

Curvature is an important geometrical feature in numerous biological and engineered systems. At the most basic level, curvature can be understood as any deviation of a surface from a flat plane. In biology, the behaviour and order of biological membranes and their constituents is strongly influenced by the curvature of the membrane.[1,2] Figure 1.1 illustrates some examples of the role of curvature in structures in animal and plant cells.[3] Membrane curvature plays a role in cell division, cellular endocytosis (the intake of macromolecules into cells) and viral replication.[4–7] The understanding of membrane budding and pinching, important stages in these processes, has led to a more complete picture of cell mechanics and growth.[8] Membrane curvature can also act as a signalling mechanism between and within cells.[1,9] Mechanosensitive ion channels

are vital in proper cell function; the MscL family of channel proteins are well-studied proteins which open and close depending on the local curvature of the membrane within which they sit, allowing for the entry and exit of crucial cellular substances. They have been shown to prevent *E. coli* bacteria from exploding by opening when the intracellular pressure gets too high.[10,11]

Recently, functionalised nanoparticles (NPs) have been used to generate curvature in cell membranes as part of a process in which other, nonfunctionalised NPs are delivered into the cells.[12,13] Processes like this could be crucial in enabling the controlled delivery of nanomedicines. Curvature as a signalling mechanism has also been exploited in the development of novel biosensors and in potential *de novo* drug delivery systems.[9,14]

Beyond biology, curvature is also important in the understanding and manufacture of novel materials, such as in the development of functional metamaterials. The mechanical and electronic properties of the two-dimensional 'wonder material' graphene are affected by its curvature.[15,16] For example, the local electrochemical potential in rippled graphene has been shown to be proportional to the square of the local curvature.[15] Carbon nanotubes (CNTs) are essentially rolled up graphene sheets and their curvature, determined by how tightly rolled they are and quantified by considering their radius, determines their electronic, mechanical and magnetic properties.[17–19]

Curvature also plays a role in the properties of nanostructured materials. Nanomaterials with structures that have negative Gaussian curvature (see Section 1.1.3) are of particular interest and include nanocavities, nanotubes, groove nanostructures and hollow nanospheres. These types of structures can provide good model systems in which to study nanoconfined processes like electrical and thermal transport.[20] Furthermore, nucleation is favoured inside nanostructures of negative curvature which is useful in certain industrial applications.[20] Curvature has also been shown to affect the direction of contact-electrification, with negative charge accumulating on surfaces with positive curvature and positive charge on surfaces of negative curvature.[21]

1.1.2 Curvature and Self Assembly

Imparting curvature onto self-assembling systems can be a way to control or direct self assembly. Self assembly is the spontaneous organisation of a larger, ordered structure

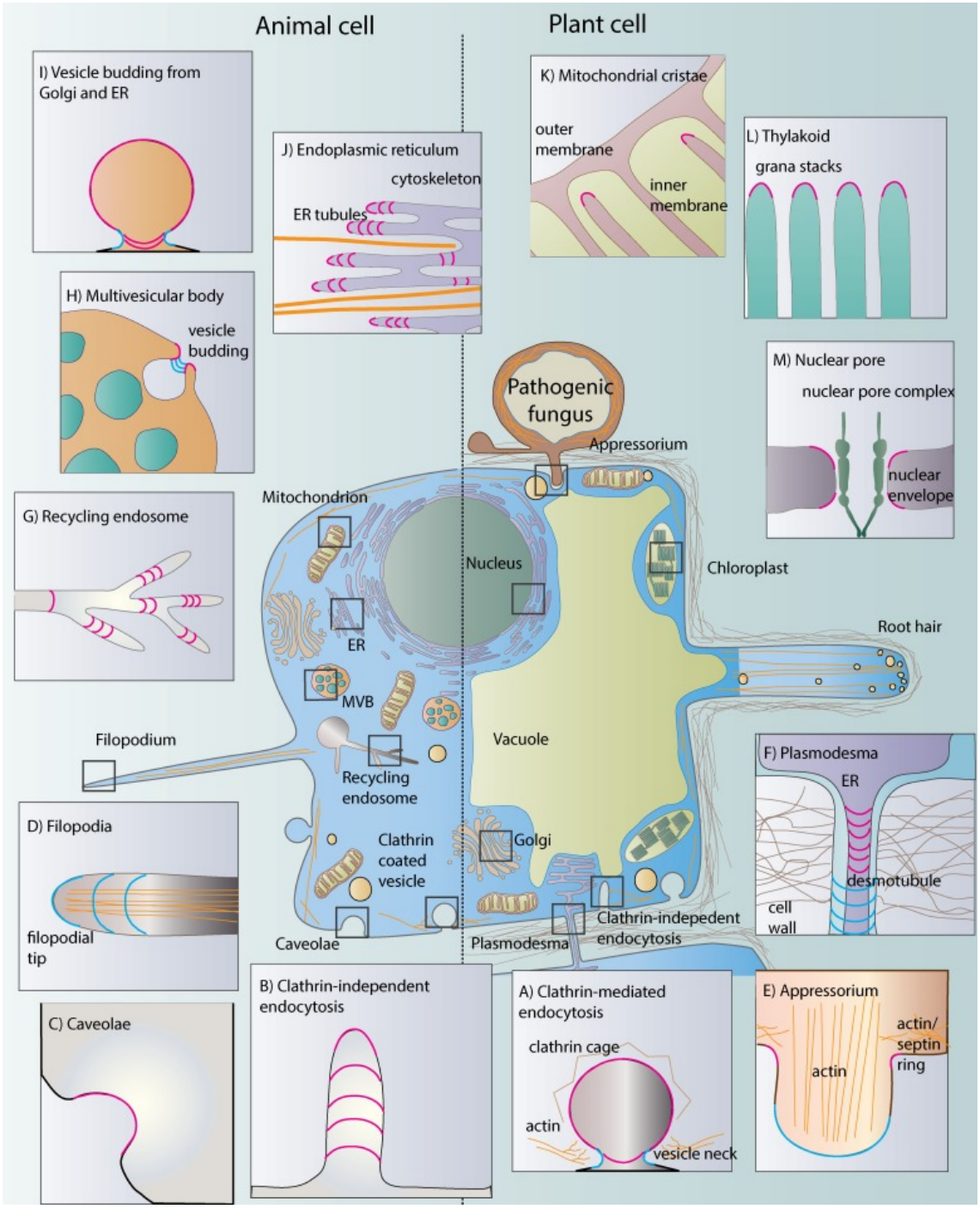

Figure 1.1: *Prominent examples of membrane curvature in cells where recent progress has revealed insights into the underlying molecular mechanisms. Convex curvature (with respect to the cytoplasm) is shown in pink lines, and concave curvature is shown in blue. Image taken with permission from work by Jarsch et al.*[3]

from component parts and is ubiquitous across all length scales; from the development of weather patterns and the formation of galaxies to the growth of cancer cells, the formation of viral capsids and protein and nucleic acid folding.[22–25] Self assembly is also utilised in industry in the synthesis of molecular crystals, monolayers and colloidal systems.[22,26]

Curvature can have a significant effect on the shape of the potential energy surface (PES) of a system (see Section 2.2) and the routes across it that the system can take. Making use of this, curvature has been used to guide the self assembly of nanoparticles and of molecular monolayers on nanoparticles.[27,28] A better understanding of the potential energy surfaces and minimum energy configurations of nanoscale systems can help in the cost-efficient development of novel, tailored, self-assembled structures.[25,29,30]

1.1.3 Defining Curvature

To deal with curvature formally, a mathematical definition is required. The curvature of a surface at a given point can be defined using its two principal radii of curvature, R_1 and R_2. These are the largest and smallest radii of all the possible circles occupying planes orthogonal to each other and to the surface. The circles follow exactly the local curvature of the surface at that point. If there is no curvature in one of the two directions, then that radius of curvature is infinite. From R_1 and R_2 two types of curvature can be defined: mean curvature H,

$$H = \frac{1}{2}\left(\frac{1}{R_1} + \frac{1}{R_2}\right),$$

and Gaussian curvature K,

$$K = \frac{1}{R_1}\frac{1}{R_2}.$$

The sign of the Gaussian curvature depends on whether the principal radii are on the same side of the surface or not, independent of which side that is. If the radii are on the same side, then the Gaussian curvature is positive, if they are not then it is negative.

Gaussian curvature in particular is useful when categorising surface curvature. Figure 1.2 illustrates three different cases, as defined by their K: where $K > 0$, where $K = 0$ (where one or both of the radii of curvature are infinite) and where $K < 0$. Spherical and ellipsoidal surfaces have positive curvature at all points; flat planar,

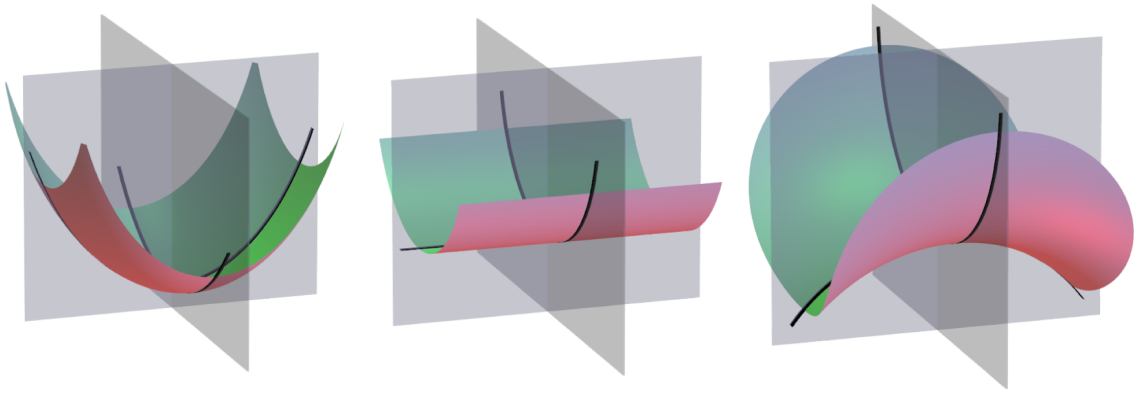

Figure 1.2: *An illustration of three surfaces with different Gaussian curvatures. The black lines indicate the intersection of the surface with the planes containing the principal radii of curvature. The point on the surface at which the lines cross is the point at which the curvature is being measured. From left to right: a surface with positive Gaussian curvature; a surface with zero Gaussian curvature; a surface with negative Gaussian curvature. Image courtesy of Mark Miller.*

cylindrical and conical surfaces have zero Gaussian curvature all over; and a hyperbolic surface (often referred to as a saddle surface) has negative Gaussian curvature.

1.2 Colloids and Colloidal Systems

Colloids are particles of one phase uniformly dispersed in a second phase with dimensions on the order of nanometres or micrometres.[31] A schematic colloidal suspension is shown in Figure 1.3. The definition can vary depending on the source, but the key attributes of non-crystalline colloidal systems are their length scale and that they are under the influence of Brownian motion.[32,33] Colloidal systems are distinct from solutions in that the particles are large enough to be considered to be in their own phase, i.e. they are not just molecules. The phases in colloidal systems are known as the dispersed phase and the continuous phase (the medium in which the particles are dispersed), both of which can take many different forms. Emulsions, liquid crystals (both liquid in liquid), gels (liquid in solid), sols (solid in liquid), foams (gas in liquid) and aerosols (liquid in gas) are all considered to be colloids, where the dispersion medium (within which the colloidal particles sit) and the particles themselves are dis-

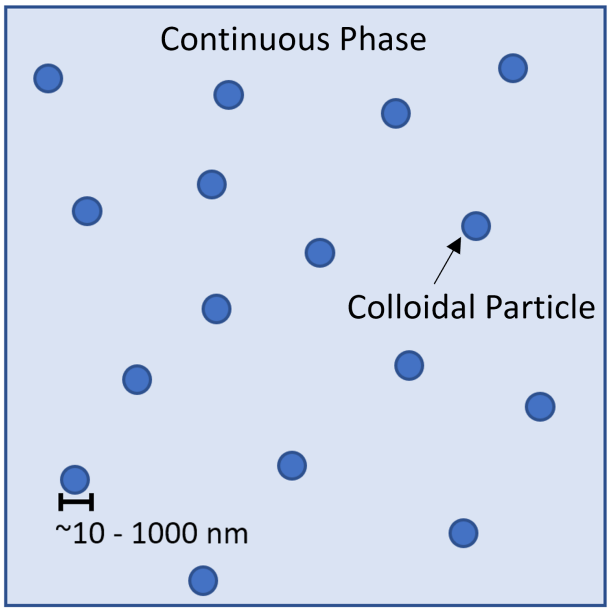

Figure 1.3: *The structure and scale of a typical colloidal suspension. Particles of one phase of diameter order 10–1000 nm are suspended in a second, continuous phase.*

tinct phases. Everyday examples of these types of colloidal systems include milk (an emulsion), shaving cream (a foam), hairspray (an aerosol), smoke (a solid aerosol — solid in gas), pigmented ink (a sol), aerogels (solid foams — gas in solid) and gelatin (a gel). This reflects the wide array of applications available for colloidal systems.

Colloids can also provide a platform for creating complex, hierarchical structures, with increasingly complex particles able to combine to form unique forms of matter, much in the way that atoms do.[34,35] A benefit of using colloidal particles in the development of new materials is the ease with which they can be modified; they can be treated as 'designer atoms' in the sense that their properties, shapes and interactions can be controlled with high precision in the lab.[34] Many different shapes and types of colloids have been synthesised; dumbbell, cubic, lock-and-key, prismatic, ellipsoidal and bowl shaped particles have all been successfully characterised, among others.[36–41] On top of tweaking the physical properties of the particles themselves, the interactions between them can also be tuned. Altering the geometries is one way of doing this, and chemically modifying their surfaces is another. Types of inter-particle interactions that have been achieved in colloidal systems include screened Coulomb, depletion, short-range attractive and ionic.[42–45] Colloids have also been made to interact anisotropically,

by constructing particles with 'patches' of different chemical properties on their surfaces.[46,47] One specific type of this kind of colloid is the so-called Janus particle, which is a particle split into two halves, each with distinct properties.[48] By manipulating the ways the particles interact with each other, the way they assemble can be modified.

1.2.1 Colloidal Crystals

In a colloidal crystal, the particles have order. They are analogous to molecular and atomic crystals in their ordering but, in general, differ in scale as the repeating subunits of the crystals are colloidal particles and not atoms or small molecules.[32,49] Colloidal crystals can be found in nature; natural opals, for example, consist of closely-packed silica particles formed over years of hydrostatic and gravitational compression.[49] Many man-made colloidal crystals are thus referred to as synthetic opals.

Colloidal crystals are the subject of active research due largely to the way they can cooperatively organise themselves into useful structures, which lends them well to cost-efficient manufacturing on the nanoscale. They can also be manipulated to undergo controllable phase transitions under the right conditions.[50] They have varied applications, including as photonic and phononic crystals, in catalysis, in display technologies, as bio- and chemical sensors and as templates in cell culturing, chemical synthesis and nanofabrication.[49,51] In photonics, colloidal crystals are of interest as, due to their size, they can act as photonic crystalline band gap materials and also as templates for manufacturing them.[49] The ease of chemical modification of colloids means that, for example, the band gaps in these materials can often be tuned conveniently.[52]

Three-dimensional colloidal crystals can be used as sacrificial templates in the manufacture of three-dimensional ordered macroporous materials (3DOM materials), materials that contain highly ordered networks of macropores connected by small channels.[49] The materials that are formed from manufacturing techniques using these templates, often referred to as inverse opals, maintain the optical properties of the colloids as the ordered network of voids created as the colloids are removed exactly replicate the shapes of the colloids that were used to template them.[53] 3DOM materials could have applications in making photonic crystals, catalysts, electrodes, sensors and more.[54]

Colloidal crystals make good systems for modelling and studying general crystalline behaviour (such as that of atomic and molecular crystals). This is because the size

of the colloidal particles allows them to be imaged in real time with standard light microscopy.[49] The larger particle sizes also mean that the organisational timescales are slower and more straightforward to track experimentally. Nucleation rates of colloidal crystals, for example, are much easier to measure than those of atoms or molecules.[55,56] There is an overlap between the forces that determine the behaviour of colloidal systems and those that govern atomic matter (electrostatics, depletion interactions etc.); colloidal particles have, for example, been used both to demonstrate the theory of crystallisation of hard spheres and the Kosterlitz-Thouless-Halperin-Nelson-Young (KTHNY) theory of melting in two dimensions experimentally.[57,58]

1.2.2 Two-Dimensional Colloidal Crystals

In the lab, colloids can be adsorbed onto surfaces, creating monolayer or thin film colloidal systems. These systems can have markedly different properties from their one- and three-dimensional counterparts. Crystalline two-dimensional colloidal systems, unlike one- and three-dimensional colloidal crystals, can be used as masks or templates for colloidal lithography where they impart their crystalline order on a substrate in the cost-effective manufacture of ordered, thin, nanostructured materials.[49] Patterned two-dimensional colloidal crystals also have potential applications as bio- and chemical sensors and in electronic and optoelectronic devices.[49] Lipids, proteins and other molecules diffusing within biological membranes could also be considered to constitute polydisperse colloidal-like liquid crystals, although the precise local order within these types of biological structures is more transient due to the constant diffusion within them. Defects in the packing of these kinds of two-dimensional crystals play a key role in the self assembly of structures such as viral capsids.[23]

Two-dimensional colloidal crystals lend themselves to synthesis on a substrate or surface.[29] Patterned two-dimensional colloidal crystals can be manufactured on substrates using techniques including transfer printing and template-directed or surface-induced assembly.[49] Assembling large, defect-free two-dimensional crystals is particularly challenging, although in some cases defects can be beneficial; for example, some purposefully engineered, artificial defects can act as photonic dopants in functional photonic devices.[59]

1.3 Colloidal Crystals on Curved Surfaces

Spatially confining colloidal crystals to specific geometries can allow the properties and function of the material to be tuned by perturbing the stable structure in a controlled way.[60] A two-dimensional crystal of identical spherical particles with a fixed density on a plane is most stable when arranged in a hexagonal pattern with each crystalline unit surrounded by six others and all particles equally spaced. For example, consider a sheet of graphene, or how layers of spherical fruit can be most efficiently packed in boxes, both of which are shown in Figure 1.4. When that hexagonal structure is transferred to an extended surface with non-zero Gaussian curvature, however, the angles between the 'bonds' joining neighbouring units can no longer be $\frac{\pi}{3}$ as in equilateral triangles, and thus strain is introduced.[25] This is also demonstrated by considering the parallel lines of units in the hexagonal packing arrangement — these can no longer be parallel when the arrangement moves to such a surface. Therefore a trade-off arises between system curvature and the local order of the particles. When it is large enough, the curvature strain can disrupt the ordered crystalline structure and produce imperfect, defective crystals. Thus, understanding the effect of curvature on these systems is another step towards controlling the packing and therefore the properties of two-dimensional crystalline materials.

1.3.1 Spherical Surfaces

The simplest curved surface to consider when confining two-dimensional colloidal crystals with curvature is the sphere, which is a surface with constant Gaussian and mean curvature (a sphere of radius r has $K = r^{-2}$ and $H = r^{-1}$ everywhere on its surface). The general problem of packing on a sphere is a well studied one. In 1904, J. J. Thomson introduced what is now known as 'the Thomson problem' where, in his plum pudding model of the atom, electronic point charges are uniformly spread across the 'surface' of the atom in a minimum energy configuration.[62] In biology there are also numerous examples of the packing of particles on a sphere; molecules or proteins packed on metazoan epithelia, viral capsids, spherical radiolaria, to name a few, are all cases where particles are confined to spherical or near-spherical surfaces, or the systems concerned can be modelled as such.[63–66] The effect of the energetic trade-off between

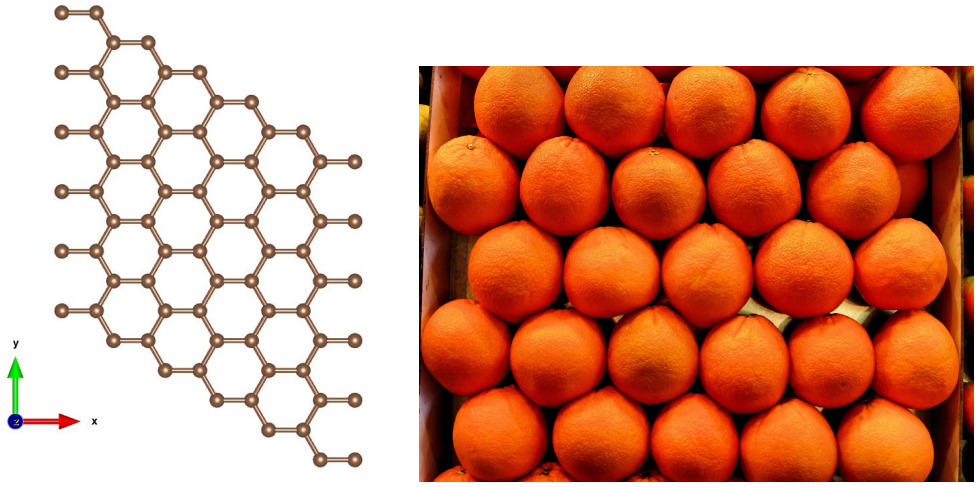

Figure 1.4: *An illustration of the hexagonal packing of a two-dimensional system on a flat surface. Left: a visualisation of the atomic structure of a small section of graphene, a single sheet of covalently bonded carbon atoms; right: a picture of oranges packed in a box at a market in Spain.*[61]

local order and longer range curvature is also a key consideration in, for example, the structure of fullerene carbon clusters and the even the ordering of electrons trapped on liquid helium bubbles.[67–69]

Defective Packing on Spherical Surfaces

Spherical confinement of colloids is of high interest given spheres offer uniform, controlled curvature with which the effects of curvature on packing and self-assembly can be studied.[60] Even in the simplest cases, finding the lowest energy arrangement of particles in spherical confinement is not a straightforward problem, and has not been fully solved even more than a century after Thomson introduced the problem for the first time in 1904. It is listed as problem seven in Smale's Problems - a list of eighteen of the most potentially consequential unsolved problems for the 21st century.[70] It has been solved analytically for only a few discrete numbers of particles (all below 12).[71,72]

The exact hexagonal packing arrangement preferred on a planar surface cannot be directly translated to the sphere, as demonstrated by Euler's formula for convex polyhedra. In 1758, Euler defined the Euler characteristic or Euler number χ, a topological invariant (a descriptor of a 3D shape that is unchanged when the surface is contin-

Figure 1.5: *An association football on Texas grass, from work by Kroto et al.*[67] *The spherical surface of the ball is completely tiled with both hexagonal and pentagonal panels, as it cannot be tiled by hexagonal panels alone.*

uously deformed), to be $\chi = V - E + F$, where V is the number of vertices on the surface, E is the number of edges and F the number of faces.[73] For all closed, convex surfaces, χ must be 2. For a surface tiled only by hexagons, χ is equal to 0, and therefore hexagons alone cannot cover a convex polyhedron; all convex polyhedra must have some non-hexagonal faces. This means that a hexagonal lattice on a spherical surface must incorporate some defects (some sites of five-fold coordination). The example of an traditional association football, as in Figure 1.5, demonstrates this in practicality.

In hexagonal lattices, two types of local topological defect are possible: *disclinations*, which are points of local five- or seven-fold symmetry (particles with coordination numbers of five or seven) and *dislocations*, which are a pair of neighbouring points, one of which has local five-fold symmetry and the other local seven-fold symmetry.[74] These defects can also be categorised by their topological charge relative to the most stable, six-fold environment (defined as $6 - m$, where m is the number of nearest neighbours): a point with coordination number of five has a topological charge of $+1$ and one with seven has a -1 topological charge. Thus the disclinations have a net, non-zero charge, and the dislocations do not (as the immediately neighbouring charges cancel each other out). A $+1$ disclination is shown in parts A and B of Figure 1.6. Above a certain system size, disclinations can combine and *scars* (high-angle grain boundaries) can form, which are defined by their excess topological charge.[75] Further, dislocations can appear lined up with variable spacing in so-called *pleats*, which have no net topological charge, depending on the underlying curvature.[74] These can also be observed in planar crystals, but tend to terminate at the edges of the crystal, whereas in spherical crystals

they terminate freely in the bulk.[75] Some pleats are shown in parts C and D of Figure 1.6.

Despite the difficulty in finding analytical solutions to the problem of arranging particles on a spherical confining surface, the problem is well studied, both experimentally with colloidal systems and computationally.[60,76–79] The net topological charge of the defects on a sphere always comes to +12, which corresponds to the simplest way of obeying Euler's rule on a sphere (and achieve $\chi = 2$), where 12 pentagons (local sites of five-fold symmetry and of +1 topological charge) are used in combination with hexagons to tile the surface. Computational approaches to the problem have shown this: Wales et al., who generated putative global minima for particle numbers N up to and including $N = 972$ using the basin-hopping algorithm, and Bowick et al., who applied continuum models to systems of up to $N = 2000$ in size, have both shown this, for example.[78,79] Studies agree that 12 defects are present on minimum energy spherically confined crystals and that individual defects are dominant at small N, while more complex defect structures become prevalent at larger system sizes. At low N, twelve isolated disclinations appear equally spaced around the sphere, and at high N these become twelve equally spaced scars, each with a net topological charge of +1.[78,79] In some cases scars can combine, radiating from individual disclinations, forming *button* defects.[79,80] Pleats are not observed in spherical systems. Experimental verification of these predictions has been quite successful, with simple, individual defects observed to be prevalent in smaller systems and twelve distinct scars observed to be prevalent in larger systems.[76,77]

For crystals of area much less than the total area of a confining spherical surfaces (often referred to as a crystal on a spherical cap), the line energy of the edge of a crystal is in competition with the strain imparted on the crystal by the surface. For surfaces of high enough curvature, the crystal forms 'ribbons' across the surface from a common point, like those shown in Figure 1.7.[25,81] These ribbons contain as close to ideal local packing as is possible on a surface with Gaussian curvature. For high enough curvature, the energy associated with forming an edge of a crystal is less than the energy associated with disrupting the preferred crystal packing. Ribbons will not form on surfaces with lower curvature as the line energy associated with forming an edge of the crystal is greater than the strain energy which the surface curvature adds to the regular lattice.

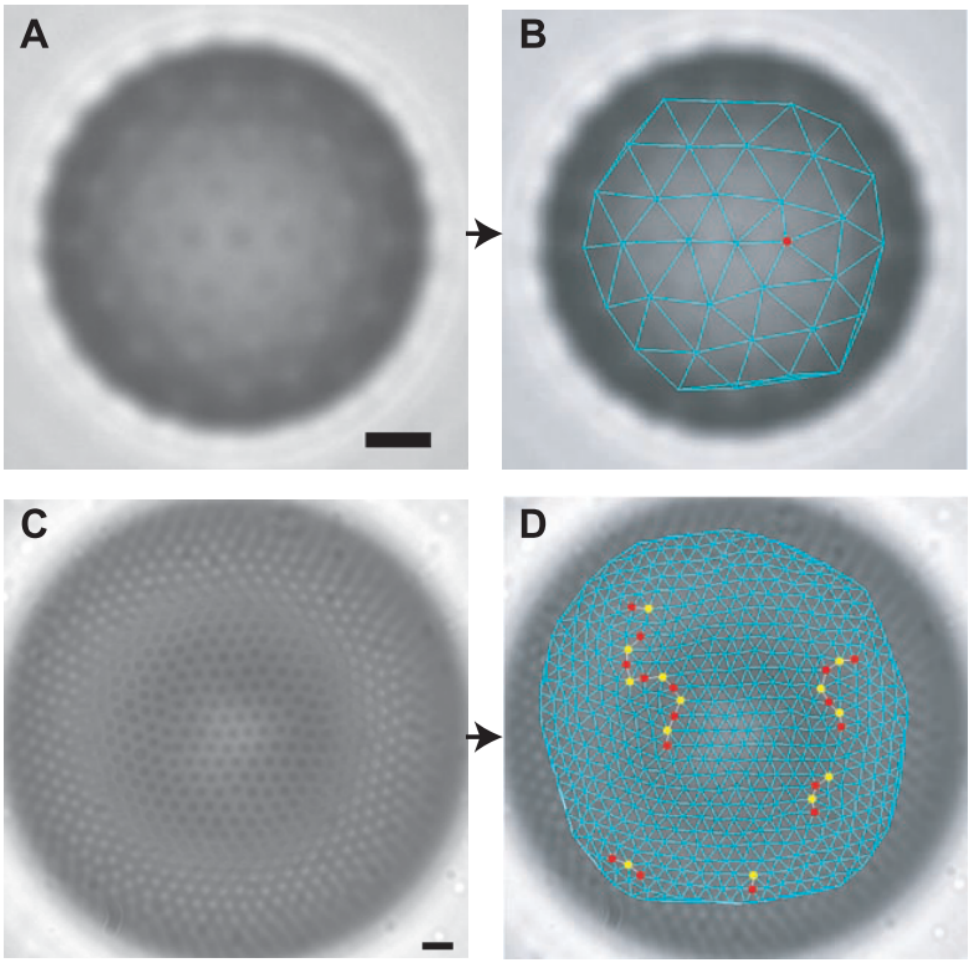

Figure 1.6: *Light microscope images of packing of particle-coated droplets on larger spherical droplets from work by Bausch et al.*[75] *In A and B: a +1 disclination with and without overlaid triangulation; in C and D: the joining of dislocations of zero topological charge to form pleats with and without overlaid triangulation.*

Figure 1.7: *A spherical droplet formed in a water-in-oil system with radius 17.6 μm partially coated in particles. The droplets in the system encapsulate an aqueous mixture of 1.0 mm polystyrene (PS) spheres and 80 nm poly(N-isopropylacrylamide) [poly(NIPAM)] particles. Ribbon-like crystals can be seen on the surface. From work by Meng et al.*[81]

Figure 1.8: *The fruit of the monstera deliciosa or Swiss cheese plant, demonstrating packing on a non-spherical surface in nature.*[82]

1.3.2 Non-Spherical Curved Surfaces

Real curved surfaces are often not simply spherical; biological systems can adopt much more complex curved shapes. One example of packing on a non-spherical surface in nature, the packing of seeds on the surface of the fruit of a Swiss cheese plant, is shown in Figure 1.8. To take some further examples from biology, the Golgi apparatus, mitochondria, tubular networks, and the endoplasmic reticulum all take specialised curved shapes more complex than spheres.[4]

Experimentally, solid, non-uniformly curved surfaces can be challenging to manufacture to a high level of precision. It is similarly challenging to produce a stable non-spherical fluid-fluid interface — droplets tend to a spherical shape given the shape's stability. There are some techniques that can be used, however. Toroidal shapes have been generated successfully in the lab: yield stress fluids have been employed to trap toroidal droplets in their non-spherical shape, and toroidal liquid films have been generated using hydrophilic and hydrophobic patterning on a substrate.[83,84] Non-spherical fluid-fluid interfaces have also been produced by pinning droplets to posts and by creating capillary bridges between opposing solid surfaces.[85,86]

Manipulating existing surfaces can be one way of producing solid shapes with a desired curvature. Holding glass needles under tension and stretching them can be one way of producing conical surfaces, for example.[87] Further, solid shapes can be milled out by using precision etching techniques like the focused ion beam (FIB),

although problems arise in the deposition of waste material and the width of the incident beam.[87,88] Advances have been made in the field of 3D printing recently, although on the microscale there are still issues with rough edges due to the definition required to print at such a small length scale.

Defective Packing on Non-Uniformly Curved Surfaces

Different kinds of defects are observed in crystals on non-spherical surfaces. As discussed earlier, spherical crystals can host disclinations with topological charge of $+1$ and scars. However, disclinations with a topological charge of -1 are not observed, as seven-fold coordination is favourable only in regions of negative Gaussian curvature. Pleats can also only be observed on non-spherical crystals, particularly in regions of low curvature.[89]

For crystals with areas much smaller than the available area on the confining non-uniformly curved surface, there is another factor to consider than defective packing: the location at which the crystal prefers to exist. On a torus, it has been shown that the location of a crystal depends on its size, its perimeter to area ratio, the local curvature and the local crystalline frustration (and thus the interparticle interaction range).[90,91] Active particles confined within a flat annulus have also been shown to prefer to accumulate on the outer concave boundaries than the inner convex boundaries.[92] Moreover, similar coupling of curvature with crystal location has been shown on sinusoidal surfaces.[91]

Packing on Curved Surfaces with Zero Gaussian Curvature

Surfaces with zero Gaussian curvature have the ability to host defect-free crystals as a two-dimensional crystal can be draped over the surface without the requirement of in-plane stretching.[93] This is the case even when the mean curvature of the surface is non-zero. Consider cylindrical surfaces, for example; at certain cylindrical radii and crystal orientations, when the periodic structure is commensurate with the circumference of the cylinder, a hexagonally packed crystal can be wrapped onto itself maintaining perfect periodicity. This is demonstrated in CNTs. The network of carbon-carbon bonding in CNTs cannot support fractional bond lengths and so CNTs can only exist with quantised values of their radii. Crystals on surfaces with zero Gaussian curvature

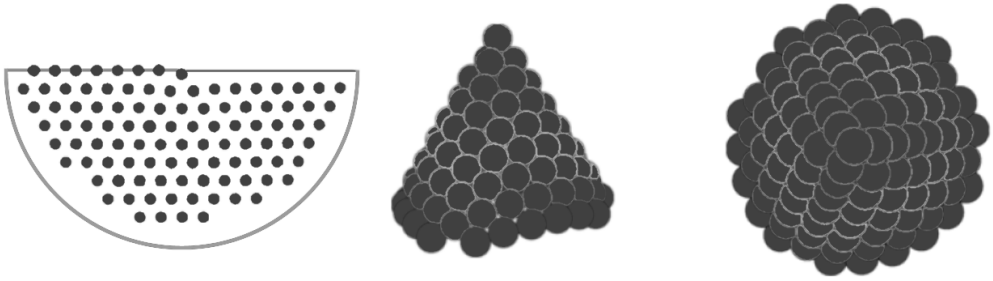

Figure 1.9: *A simulated two-dimensional colloidal crystal packed on a cone with a 'magic' net angle of 180°. From left to right, the net of the cone, side view of the cone and top view of the cone. At this net angle, a perfect, defect-free crystal can be hosted by the cone. Image adapted from Jack Law's work.*[90]

can be perfect, but they can also be made to host defects when confined in a system of finite size.[93] Cylindrical crystals, for example, can host chiral seams, or 'line slips', at values of the cylinder circumference not commensurate with the periodicity of the crystal lattice.[93] On the kinetics front, the 'closure' constraint of the periodicity in cylindrical crystals can also be responsible for so-called closure catastrophes, where the crystal growth is halted by the accumulation of topological defects which appear as the crystal wraps around the surface and reaches its own edge.[94,95] Work by Tanjeem et al. has demonstrated the line slip phase forming in confined, cylindrical colloidal crystals, where the hard cylindrical surface they used was a heated, stretched glass optical fibre.[95] They also identified kinetically trapped kinked line slips with partial vacancies which arise due to the closure constraint.

1.4 Colloidal Crystals on Conical Surfaces

Moving from the cylindrical surface with zero Gaussian curvature and constant mean curvature, conical surfaces also have zero Gaussian curvature but variable, non-zero mean curvature, the value of which depends on the distance from the apex of the cone. Hence, conical surfaces should be expected to host defect-free crystals in some situations. One situation where a defect free crystal is hosted on a cone is shown in Figure 1.9.

The work in this thesis is motivated in part by recent experimental work by Jessica

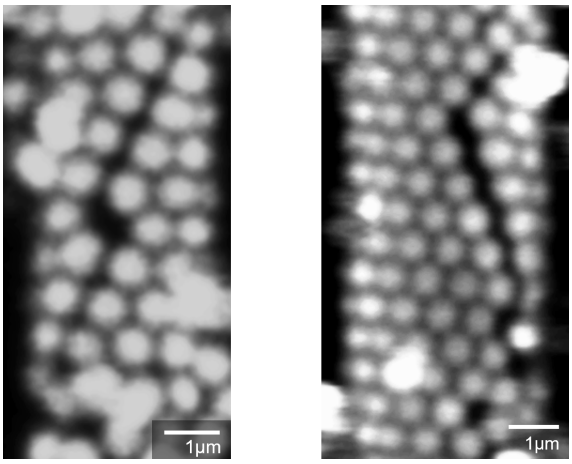

Figure 1.10: *Unpublished light microscopy images of colloidal crystals on confining conical surfaces, left of* $\theta_p = 0.2°$ *(*$\theta_{max} = 0.011°$*), right of* $\theta_p = 0.9°$ *(*$\theta_{max} = 0.049°$*), generated by Jessica Sun in the Manoharan Lab at Harvard University.* θ_p *is the angle of the three dimensional cone, as illustrated in Figure 2.2 in Section 2.1, and* θ_{max} *is the angle of the net, as illustrated in the same figure. A line slip can be seen in the left image, and a wedge-like void can be seen in the right image. Used with permission.*

Sun in the Manoharan Lab at Harvard University and considers the ground state configurations of two-dimensional colloidal crystals on confining conical surfaces. Here, large-angle cones were investigated first to reproduce previous results.[90] Crystals on small-angle cones were then investigated, where the conical surface tends to cylindrical. The cone angles accessible in the experimental work were generally small, and so this provided the motivation for the small-angle cone investigation. One aim was to complement the experimental work, in part by reproducing and rationalising certain defect structures such as line slips and wedge-like voids, both shown in Figure 1.10. The main aim, however, was to pursue a general understanding of the packing of two-dimensional crystals on conical surfaces including: defect shape and behaviour; the effect of cone angle and interparticle interaction range; and preferred crystal location.

In Chapter 2, the methodology is outlined. The model system for the colloidal crystal and the basin-hopping method used to find the putative global minima are introduced. Voronoi tessellation, the visualisation method employed to assist in the structural analysis of the putative global minima, is also discussed.

In Chapter 3, the results are presented. The first set of results to be explored

are crystals on large angle cones. Defect patterns in crystals on conical surfaces of certain 'magic' (angles that can host defect-free crystals), near-'magic' and intermediate (halfway between successive magic angles) angles are discussed. The structural differences between crystals with long and short range interparticle potentials are also discussed. Next is the investigation of crystals on small-angle cones. A wide range of possible defect structures are found. A 'phase diagram' illustrating the relationship of the defect structures with the cone angle and the potential range is then constructed, and the defect types are analysed in detail. The last sections of the chapter outline two further investigations. The first involves the construction of a model that attempts to explain the preferred position of a crystal band on a conical surface, and the second investigates the effect of a fixed ring of particles at the truncated end of the cone. Finally, in Chapter 4, the overarching conclusions and potential directions for future work are laid out.

2. Methodology

In this chapter, the methodology used in the work described by this thesis is outlined. In Section 2.1, the model for the colloidal crystals is discussed, followed by both the implementation of the confining curved conical surfaces and the boundary conditions applied to constrain the particles to the surfaces. The minimum energy structures were generated in this work by basin-hopping, a technique first proposed by Li and Scheraga in 1987 and then further developed by Wales and Doye in 1997.[96,97] Basin-hopping is outlined in Section 2.2. Finally, in Section 2.3, there is an overview of the Voronoi tessellation method used to visualise the structures and prepare them for analysis.

2.1 The Model System

A computational model of a colloidal crystal constructed from isotropically attractive Morse particles was used in this work. Real colloidal systems are rarely monodisperse but, for simplicity, the model crystals here are, meaning that every particle in each system is the same size and shape. The number of degrees of freedom in each monodisperse, conical, two-dimensional Morse crystal of N particles considered in this work is $2N-1$ (-1 due to rotation of the crystal about the cone axis). In the model system, each particle is defined by the coordinates of its centre. A pairwise Morse potential acting between particle centres determines the equilibrium separation and thus the particle diameters. The Morse potential energy U_{M} of two particles separated by a distance r is defined as

$$U_{\mathrm{M}}(r) = \epsilon\, e^{-\rho(r-r_0)}(e^{-\rho(r-r_0)} - 2),$$

where ρ is the parameter that defines the range of the potential, r_0 is the equilibrium interparticle distance (the minimum in the potential, see Figure 2.1) and ϵ is the unit

of energy and the energy of the system at $r = r_0$. Both the energy unit ϵ and the interparticle equilibrium distance r_0 were set to 1 for this work. Figure 2.1 illustrates the shape of the potential.

Although the functional form of the Morse potential is empirical, it captures the key features of a steep, repulsive core and a well of conveniently adjustable depth and range that may be used to describe attractive interactions between colloidal particles where present.[98,99] For example, the Morse potential has been fitted to the Asakura-Oosawa potential in modelling colloid-polymer mixtures in three dimensions.[100,101] By tuning the range parameter, the Morse potential has also been used to rationalise experimental statistics on structural isomerism in colloidal clusters.[102,103] Furthermore, the extensive body of computational studies on Morse-based models provides a well established context for interpreting new results.[102–105]

The range of the potential (linked to the width of the potential well) is easily adjusted: $\rho = 18$ was used as an approximation to short range interactions and $\rho = 6$ represents the longest range interactions used here. The shorter the range of the potential, the 'harder' the particles in the model system. In past works, $\rho = 30$ has been used to approximate interactions in real colloidal systems.[102–105] Here, $\rho = 18$ is employed, which represents a trade-off between computational time (as shorter range interactions make the structures harder to converge) and having a short enough range to approximate real systems. The effect of these values of ρ on the shape of the potential is shown in Figure 2.1.

Here, the Morse particles are confined to truncated conical surfaces defined by cylindrical coordinates of $[\phi, z]$, where ϕ is the angle around the z axis, and z is the height on the cone, as shown in Figure 2.2. The midpoint of the axis of the cone is set as $z = 0$ and ϕ is measured about its axis. By using this coordinate system, the particles are confined to the conical surface in ϕ, but not in z. The particles must also be confined in z and different approaches to this problem are discussed in Section 3.1. The dimensions with which the surfaces are defined are shown in Figure 2.2: θ_p and θ_max are the angles of the cone and the net of the cone respectively, h is the height of the truncated cone, and r_b and r_t are the radii of the base of the cone and the truncated top of the cone respectively. In this work, the cone angle (θ_p or θ_max) is varied at constant area and, in most cases, a constant truncation radius r_t of 1.0.

The dimensions of the cone and the net of the cone are related by the following

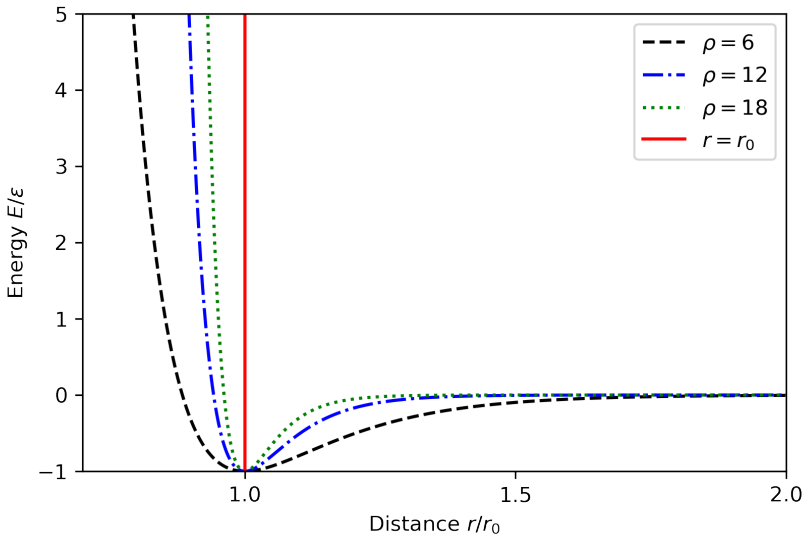

Figure 2.1: *The Morse potential and the effect of the range parameter ρ on its shape.*

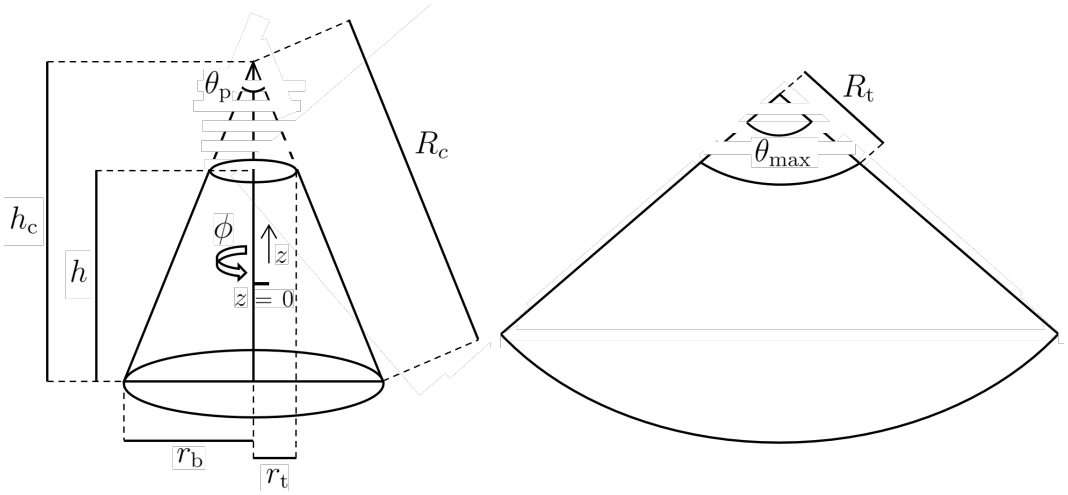

Figure 2.2: *The dimensions of the truncated conical surface on which the colloidal crystal was confined, left, and the net of the surface, right. The $[\phi, z]$ coordinate system is shown.*

expressions:

$$h_{\mathrm{c}} = \frac{h}{1 - \frac{r_{\mathrm{t}}}{r_{\mathrm{b}}}}$$

$$R_{\mathrm{c}} = \sqrt{h_{\mathrm{c}}^2 + r_{\mathrm{b}}^2}$$

$$R_{\mathrm{t}} = \sqrt{(h_{\mathrm{c}} - h)^2 + r_{\mathrm{b}}^2}$$

$$\theta_{\mathrm{max}} = \frac{r_{\mathrm{b}}}{R_{\mathrm{c}}}$$

$$\theta_{\mathrm{max}} = 2\pi \sin\left(\frac{\theta_{\mathrm{p}}}{2}\right) \tag{2.1}$$

In transforming from the cone to the net of the cone, a cut is made at some arbitrary $\phi = 0$ and the conical surface is 'unrolled'. The surface of the cone has periodicity 2π in ϕ, but no periodicity in z.

2.2 Global Optimisation

In this work, putative global minimum energy structures of the model crystals described in Section 2.1 were generated. Globally optimising these types of structures is not a straightforward task. The problem of global optimisation, finding the lowest minimum out of all of the turning points (minima, maxima and saddle points) of a function or functions, is found across mathematics, science and engineering. Global optimisation appears in mathematical problems such as in finding minimum path lengths (e.g. the travelling salesman problem), fitting or packing objects and curve fitting; in engineering problems such as the design of microprocessors; and in scientific problems like in protein or molecular structure prediction (through minimising energy functions).[106,107] In this work, the focus was on finding global minima. While finding local minima (those nearest to the point at which the procedure is initiated) is often a well-defined task, success in the more challenging global optimisation problem (finding the absolute lowest minimum of the function independent of the starting point) cannot be guaranteed and methods usually only provide best guesses — putative global minima.

Monte Carlo Approaches

A popular way of approaching global optimisation problems is with a Monte Carlo (MC) algorithm. MC algorithms are diverse, but all include some aspect of randomness — the approach was named after the grand casino in Monaco at Monte Carlo by Nicholas Metropolis in 1947.[108] Such algorithms use stochastic sampling (random sampling from a given probability distribution) to solve problems numerically. MC algorithms are important in a number of fields; an MC algorithm was named the most influential algorithm of the 20$^{\text{th}}$ century by *Computing in Science and Engineering*.[109] Applications range from computer graphics (as a way of solving the rendering equation used in path tracing three-dimensional image rendering), to evaluating the impact of risk in business and finance (including in derivative valuation).[110,111]

In condensed matter physics, MC algorithms are useful tools for efficiently exploring the configuration space of complex systems in cases where dynamics are not needed. They are used to investigate many-body structure problems on the quantum, atomic and molecular scales, where the high dimensionality of the configuration spaces of the systems prove too computationally costly to be dealt with by non-stochastic means. The Monte Carlo Metropolis-Hastings (Metropolis MC) algorithm is commonly used to explore potential energy surfaces in these cases.[112] It proceeds as follows:

1. The system energy is calculated;

2. A small, random perturbation is applied to the system coordinates;

3. The new system energy and thus the change in energy due to the move ΔE are calculated. If the move reduces the system energy (and $\Delta E < 0$) then the move is accepted; if it does not (and $\Delta E > 0$) then the move is accepted with a probability P defined by the temperature T and ΔE. This acceptance criterion can be compactly written as

$$P = \min\left[1, \exp(-\frac{\Delta E}{k_{\text{B}}T})\right],$$

where k_{B} is the Boltzmann constant.

A common adaptation of this approach employed to find the lowest energy configuration of the system is simulated annealing.[113] In a similar way to the physical

annealing process used in materials science, the method proceeds with a steadily decreasing temperature T. In terms of the above steps, steps 2 and 3 are repeated with an incrementally lower temperature T each time.

Potential Energy Surfaces

The structure of a many-body system exists on an n-dimensional potential energy surface (PES), sometimes referred to as an 'energy landscape', where n is the number of degrees of freedom of the system.[107] Finding the point of lowest energy on the PES is equivalent to finding the most stable configuration of the system. Surveying a PES comprehensively to find its global minimum efficiently is tough, especially when the surface is complex and has many local minima.

Different kinds of surfaces provide different challenges. 'Structure-seeker' surfaces have a gentle funnel-like structure which leads to the global minimum. Annealing MC is successful at optimising systems with this kind of PES, i.e. surfaces that are smooth and have low energy barriers and multiple paths that converge to the global minimum, but systems with 'glassy' surfaces, which have a large number of distinct potential low energy configurations sitting in funnel-like local minima separated by high energy barriers, are much harder to optimise.[97] For example, simple MC annealing methods have been shown to successfully find global potential energy minima of simple Lennard-Jones clusters, but fail to find minima for more complex clusters.[97] They also fail in more complex cases such as protein structure prediction.[114] Systems with short range interparticle interactions such as those investigated in this work tend to have glassier, more complex PESs. Thus, the path between a random starting point and the true global minimum is likely to pass through a large number of local minima, often with high energy. This makes it much more difficult for simple MC optimisation algorithms such as simulated annealing described above, which can easily get trapped by the local minima.[115] Hence, different methods are required to effectively deal with these kinds of surfaces.

Basin-Hopping

In this work, the systems in question consist of particles with short-range attractive interactions. These are typical cases where the PES is complex, rough and difficult to

sample and so it is challenging to find the global potential energy minimum with standard MC approaches. To make better progress with this task, we use basin-hopping, a method proposed by Wales and Doye in 1997 and inspired by the work of Li and Scheraga in 1987 which removes the barriers between local minima.[96,97] It has been shown to have success in tackling complex geometry optimisation problems such as clusters and spherical crystals.[78,116] Basin-hopping transforms the complex PES at hand into a series of neighbouring 'basins'; formally, this transformation of the potential energy function $U(\mathbf{r}^N)$ is written

$$\tilde{U}(\mathbf{r}^N) = \min[U(\mathbf{r}^N)],$$

where $\min[U(\mathbf{r}^N)]$ is a local minimisation of $U(\mathbf{r}^N)$.

The basin-hopping algorithm proceeds in a similar way to the general Metropolis MC procedure outlined above, but after each perturbation the geometry is subject to a local energy minimisation. Often the limited-memory Broyden-Fletcher-Goldfarb-Shanno (L-BFGS) algorithm is used to do this and it is the algorithm used in this work. Thus every point on the surface is assigned the same energy as its local minimum, as shown in Figure 2.3. The set of points associated with each minimum is referred to as its 'basin of attraction'. The algorithm is less likely to become trapped in local minima away from the global minimum and hence more of the PES is explored and the global minimum of a complex PES is more likely to be found.

The general basin-hopping algorithm is as follows:

1. The system energy is calculated;
2. A random perturbation is applied to the system coordinates;
3. The coordinates undergo a local energy minimisation;
4. The new coordinates are accepted or rejected with a probability P which, like in Metropolis MC, is dependent on the difference between the energies of the system before and after the move $\Delta\tilde{U}$ and the temperature T of the system according to

$$P = \min\left[1, \exp(-\frac{\Delta\tilde{U}}{k_{\mathrm{B}}T})\right]$$

and the local minimum is recorded;

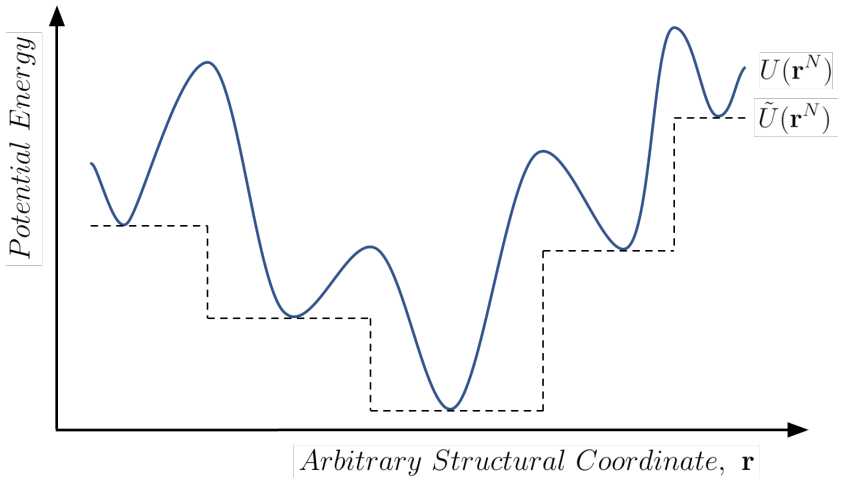

Figure 2.3: *An illustration of the basin-hopping algorithm transforming a one-dimensional potential energy surface (PES) into a surface of 'interpenetrating staircases'. The original PES, $U(\boldsymbol{r}^N)$, is shown with the solid line and the transformed PES, $\tilde{U}(\boldsymbol{r}^N)$, is shown with a dotted line.*

5. Steps 2 to 4 are repeated for a predetermined number of steps;

6. The lowest energy local minimum recorded at the end of the above steps is designated the putative global minimum.

In basin-hopping, the temperature T in the acceptance criteria is often referred to as the basin-hopping temperature. The higher it is, the more likely a move into a higher energy basin is accepted. Thus, it controls the rate of exploration of the PES.

In this work, the basin-hopping algorithm was applied using an adapted version of the open source code GMIN, developed by the Wales group at the University of Cambridge. The original code is freely available on their website.[117] In the adapted form of basin-hopping used here, the moves are implemented by placing each particle at a random point on a sphere centred on the original location of the particle. The particles are then projected back to the nearest point on the surface. This particular stepping procedure is used as the surface is curved and so standard random translation moves in Cartesian space are not straightforward. A fictitious temperature parameter of 1 was chosen. For all calculations carried out in this work, the general method for finding putative global minima involved carrying out $80,000$ total basin-hopping steps in two runs of $40,000$ (due to run time limitations run time on the high performance

computing service used). Often, the output putative global minimum energy crystal would be fragmented with some particles detached from the bulk crystal, as the random initial fragments can start too far apart to interact and so there is no gradient to drive the clusters together. To solve this problem, an initiation step was introduced. Thus, the basin-hopping was carried out as follows:

1. Within the dimensions of the surface, all of the particles are given random starting positions;

2. 10 basin-hopping steps are carried out with the range of the Morse potential set to a very long range value of $\rho = 4$ in order to coalesce the particles and pull them together at the start;

3. The lowest energy minimum found during these 10 steps is used as the starting point for the basin-hopping proper;

4. Basin-hopping is carried out as above, using the desired larger values of ρ.

This, in general, helped to generate single crystal minima. Longer range potential crystals tend to converge more quickly due to their simpler energy landscapes. This was discussed by Miller et al. in 1999.[118]

In these systems, the putative global minima can often be different across different basin-hopping runs. This is due to the complexity of the PES of a crystal size of the order of $N = 10^2$ like those considered in this work. The number of particles in the systems means that one particle move around the edges of the crystals can move the system to a different minima but, as the energy before and after the move are very similar and the bulk of the structure is the same, the minima is essentially the same. Thus, complete repeats of the above process were carried out and the lowest overall minimum across the repeats was taken as the putative global minimum. A sample input file for the main basin-hopping calculations can be seen in Appendix A.1.

2.3 Voronoi Tessellation

In order to analyse the putative global minimum energy systems generated by the above methods, visualising the structures effectively is key. A way must be found to

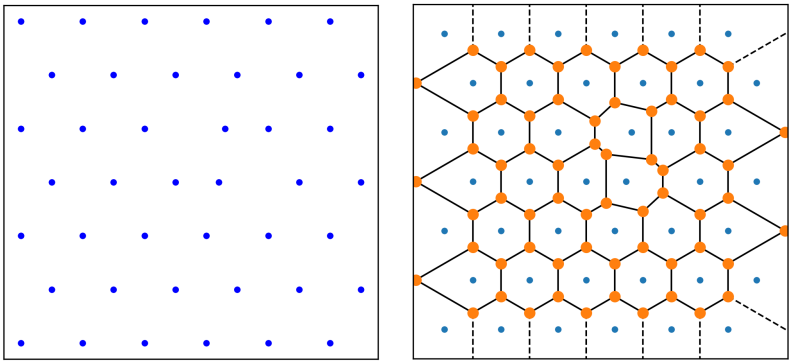

Figure 2.4: *An example of a Voronoi tessellation of a selection of points on a two-dimensional surface. Left: the points before Voronoi tessellation; right: the points after Voronoi tessellation. Vertices between Voronoi cells are shown in orange and dotted lines indicate cell boundaries which do not terminate at vertices at both ends (and thus unbounded cells). The Voronoi tessellation helps the reader to identify where order has broken down in the arrangement of the points.*

clearly identify and locate any defects in the crystalline order. A method which has been applied in the past for such a purpose is Voronoi tessellation, named after Georgy Voronoy, who first published his study of this kind of tessellation in n-dimensions in 1908.[119,120] Simply, Voronoi tessellation divides a space containing a collection of points into a set of polygons, each containing one point and all of the space closer to that point than any other. This is demonstrated in Figure 2.4. Thus, order and disorder in the arrangement of points is illustrated more clearly. Voronoi diagrams have been applied in a variety of contexts. They have been used in aviation to find nearest airfields for diversions, in assigning voting or schooling catchment areas and even as the basis for the facade of the Home of the Arts on the Australian Gold Coast.[121–123] Voronoi diagrams have also been employed effectively to visualise the order in crystalline structures.[66,78]

Here, the global minimum configurations on the net of the conical surfaces are considered and so only two-dimensional Voronoi tessellation is relevant. The steps taken to produce the Voronoi diagrams in this work are outlined in Figure 2.5. First, the program outputs the coordinates of the Morse particles. They are output by default in three dimensions and the source code was adapted so the coordinates of the particles projected onto the net of the conical surface are also output. The Voronoi diagram of the crystal on the net can then be produced from these coordinates. Lastly, the diagram

is coloured based on the attributes of the polygons: regular hexagons are coloured in green, irregular hexagons in yellow, pentagons in red and heptagons in blue. These colourations reflect the coordination environment of the particle they contain. Thus, defects in the crystal show up clearly, with the non-green polygons contrasting against the regions of 'perfect' hexagonally packed crystal in green. The irregular hexagons are determined to be irregular by considering the lengths of the sides. When any one of the sides is more than 30 % longer than any of the others, the hexagon is labelled irregular and coloured yellow. Unfortunately, the Voronoi method is not as useful for visualisation at the edges of the crystal. Although many larger cells are removed, the larger and open cells at the edges mean that red, blue and orange (orange polygons have a number of sides that is not 5, 6 or 7) polygons appear around the edges without providing any useful information about the crystalline packing. In general, these should be ignored. The coordinates are periodically repeated in ϕ to preserve the tessellation at the straight edge boundaries of the net, but at the top and bottom of the crystal in the direction with no periodicity, these artefacts still appear, as seen in Figure 2.5.

In this work, the Voronoi diagrams were generated using the Python3 (version 3.7.9) spatial package which is part of the SciPy library (version 1.6.0) and plotted using Matplotlib (version 3.4.3).[124,125] The package uses the Qhull library (version 8.0.2) to perform the Voronoi tessellation.[126]

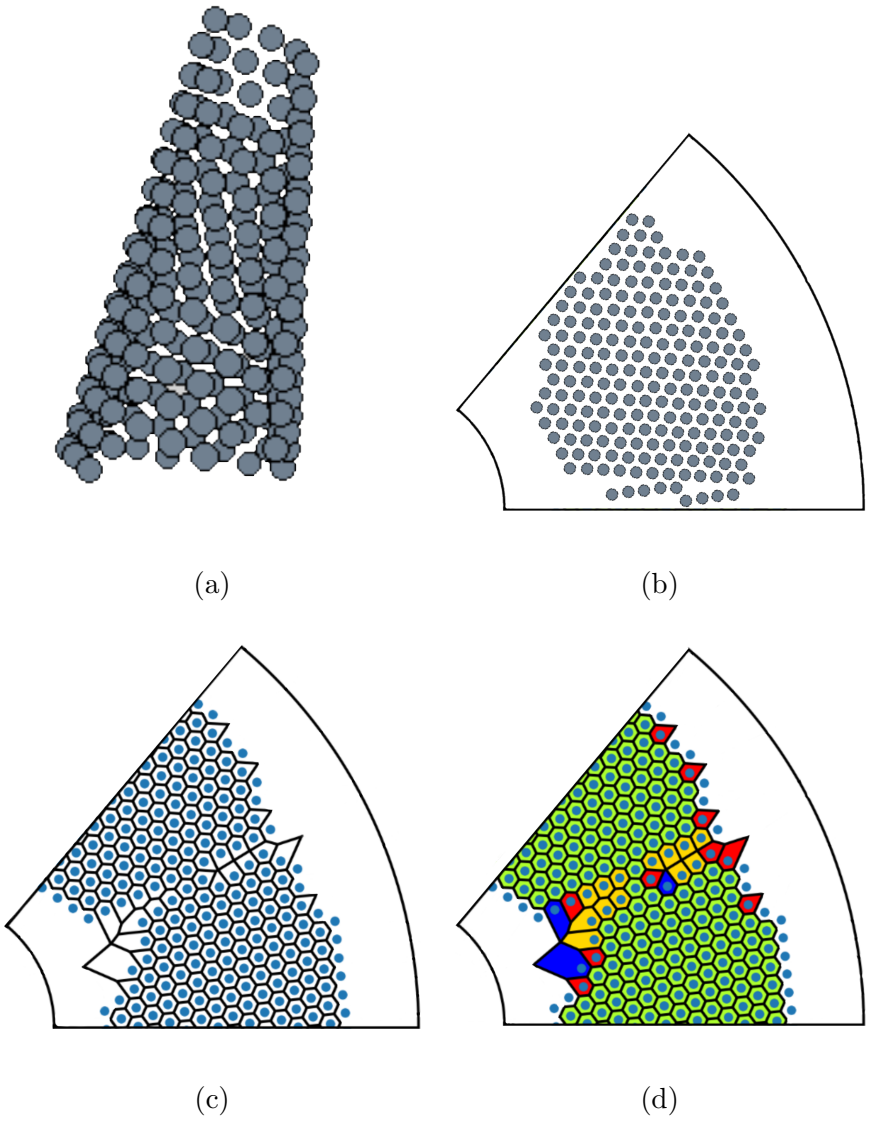

Figure 2.5: *Step-by-step visualisation of the generation of Voronoi diagrams in this work. The output Morse crystal particle coordinates in three dimensions are shown in (a); the Morse crystal coordinates transformed to the net of the cone are shown in (b); a Voronoi diagram produced from the coordinates on the net of the cone is shown in (c) (note that there has been a rotation of the coordinates in ϕ to put the defects in the centre); the Voronoi diagram coloured based on the shapes of the polygons is shown in (d). The polygons are coloured as follows: regular hexagons in green, irregular hexagons in yellow, pentagons in red and heptagons in blue. The outline of the net of the cone has been superimposed on the Voronoi diagrams and bounds them.*

3. Results and Discussion

This results chapter is structured as follows. First, in Section 3.1 potential approaches to the lack of confinement of the conical surface in the z direction, as described in Section 2.1, are discussed in Section 3.1. The section concludes with the approach used for the majority of the rest of the work. Next, in Section 3.2, minimum energy structures on large-angle cones are shown and discussed. Section 3.3 deals with small-angle (near-cylindrical) cones, where the different possible defect structures are shown, along with trends in energy and behaviour as the angle and the potential range ρ are varied. A 'phase diagram' is used to illustrate the general behaviours and then the defect structures are discussed in more detail. The chapter finishes with two other studies. Section 3.4 looks to model the ideal position of a band of crystal on the conical surface, while Section 3.5 attempts to model scenarios where some colloidal particles are pinned at the upper boundary of the truncated cone.

3.1 The Surface Boundary Conditions

Before the simulations could be started, the treatment of the boundaries had to be considered. The conical surfaces used in this work, as described in Section 2.1, are periodic in ϕ but unconstrained in z. If the system is left unconstrained in z, then particles can escape the surface when the basin-hopping steps are carried out. Here, three approaches to dealing with this problem were trialled.

3.1.1 A Cyclical Coordinate System

In previous work, the conical surface was constrained in z through the use of a cyclical coordinate system, $[\phi, \psi]$.[90] By the nature of using an angular coordinate ψ to define

the position in the z dimension, the position on the cone smoothly changes direction at the boundary of the cone and so the particles cannot escape the cone. Under this cyclical coordinate system, a position on the cone in three-dimensional space $[x, y, z]$ is calculated as follows:

$$x = r_{\mathrm{b}} \frac{h_{\mathrm{c}} - (\frac{h}{2}) \cos\psi + \frac{h}{2}}{h_{\mathrm{c}}} \cos\phi,$$

$$y = r_{\mathrm{b}} \frac{h_{\mathrm{c}} - (\frac{h}{2}) \cos\psi + \frac{h}{2}}{h_{\mathrm{c}}} \sin\phi,$$

$$z = \frac{h}{2} \cos\psi,$$

where h is the height of the truncated cone, r_{b} is the radius of the base of the cone and h_{c} is the height of the untruncated cone, all dimensions as defined in Figure 2.2 in Section 2.1. From these relations the interparticle distances and thus Morse interaction energies and gradients could be calculated within this coordinate system.

The cyclical coordinate system is useful in that it naturally constrains the particles on the surface, but its application is more computationally intensive than that of the cylindrical coordinate system described in Section 2.1. As uniform changes in vertical position z do not generate uniform changes in the cyclical coordinate ψ, it is more challenging for the algorithm to converge and thus basin-hopping steps take longer. A new approach was thus required to allow larger systems to be investigated than in previous work.[90] A comparison of the cyclical coordinate system with an alternative confinement approach using boundary potentials in the $[\phi, z]$ coordinate system (which will be discussed in Section 3.1.2) is shown in Table 3.1.

3.1.2 Simple Repulsive R^{-12} Potential

The second approach that was trialled was the implementation of a simple, repulsive boundary potential acting at the top and bottom boundaries of the conical surface. Here, the $[\phi, z]$ coordinate system discussed in Section 2.1 is in use. The energy E_{boundary} of the boundary potential was defined as

$$E_{\mathrm{boundary}} = \frac{A}{(\frac{h}{2} - z)^{12}} + \frac{A}{(\frac{h}{2} + z)^{12}}$$

Approach	Mean steps/B-H Step	Mean time/B-H step
Cyclical Coordinates	1641	1.601 seconds
Simple R^{-12}	891	0.707 seconds

Table 3.1: *A comparison of the computational cost of two different approaches to confining the system in z. The comparison was carried out over 100,000 basin-hopping (B-H) steps on a system of 100 Morse particles with potential range $\rho = 6$ on a surface of $r_t = 0.1$ and $\theta_{max} = 60°$.*

and the gradient as

$$\frac{dE_{\text{boundary}}}{dz} = \frac{12A}{(\frac{h}{2} - z)^{13}} - \frac{12A}{(\frac{h}{2} + z)^{-13}},$$

where h is the height of the truncated cone as defined in Figure 2.2 in Section 2.1 and A is some constant (which was set to 0.001 to keep the function small at values far from the boundaries).

This twelfth-power potential is at its minimum at $z = 0$ and increases quickly as the top and bottom boundaries of the cone at $\pm\frac{h}{2}$ are approached. This potential has advantages in computation time and simplicity of implementation over the cyclical coordinate system approach discussed in Section 3.1.1, as shown in the comparison in Table 3.1. However, there is a small, non-zero gradient at all values of z except at exactly $z = 0$ which could affect the minimum energy structures and so an improved approach was devised.

3.1.3 Truncated, Shifted, Smoothed Repulsive R^{-12} Potential

To minimise any potential for the boundary treatment to affect the minimum energy structures generated in this work, the simple R^{-12} potential was adapted. To address the non-zero value of the potential for all values of z, the potential was truncated to force it to zero at some values $(\frac{h}{2} - z_{\text{cut}})$ and $(-\frac{h}{2} + z_{\text{cut}})$, where z_{cut} is some cutoff distance from the boundaries, so the boundary only contributes to the system energy at the very top and bottom on the conical surface. This was done using equal and opposite Heaviside (step) functions, $\theta(z)$. This, however, creates two problems. Firstly, the potential does not smoothly go to zero at the cutoff values (it is no longer continuous). Secondly, discontinuities are also introduced into the gradient of the potential. To

address these issues, two further adaptations were made to the potential: the function was shifted down in energy so that the energy reaches zero continuously and then smoothed to ensure the gradient was also continuous. The energy associated with the adapted R^{-12} boundary potential was defined as

$$E_{\text{boundary}} = \left[\frac{A}{(\frac{h}{2}+z)^{12}} - \frac{A}{(\frac{h}{2}+z_{\text{cut}})^{12}} + \frac{12A(\frac{h}{2}-z_{\text{cut}}+z)}{(\frac{h}{2}+z_{\text{cut}})^{13}}\right]\theta(z_{\text{cut}}-\frac{h}{2}-z)+ \left[\frac{A}{(\frac{h}{2}-z)^{12}} - \frac{A}{(\frac{h}{2}-z_{\text{cut}})^{12}} - \frac{12A(\frac{h}{2}+z_{\text{cut}}-z)}{(\frac{h}{2}-z_{\text{cut}})^{13}}\right]\theta(z_{\text{cut}}-\frac{h}{2}+z),$$

and the gradient as

$$\frac{dE_{\text{boundary}}}{dz} = \left[\frac{-12A}{(\frac{h}{2}+z)^{13}} + \frac{12A}{(\frac{h}{2}+z_{\text{cut}})^{13}}\right]\theta(z_{\text{cut}}-\frac{h}{2}-z)+ \left[\frac{12A}{(\frac{h}{2}-z)^{13}} + \frac{12A}{(\frac{h}{2}+z_{\text{cut}})^{13}}\right]\theta(z_{\text{cut}}-\frac{h}{2}+z),$$

where z_{cut} is the positive cutoff value of the potential in z (set to $z_{\text{cut}} = 1.0$ going forwards in this work, the diameter of one particle, to keep the effect of the potential localised to the boundary), h is the height h of the truncated cone as defined in Figure 2.2 in Section 2.1 and A is a scaling factor (set to 0.001 again, the same as in the previous potential). The shapes of the potential and its gradient are shown in Figure 3.1. This boundary potential was used for the majority of the calculations in this thesis, unless specified otherwise.

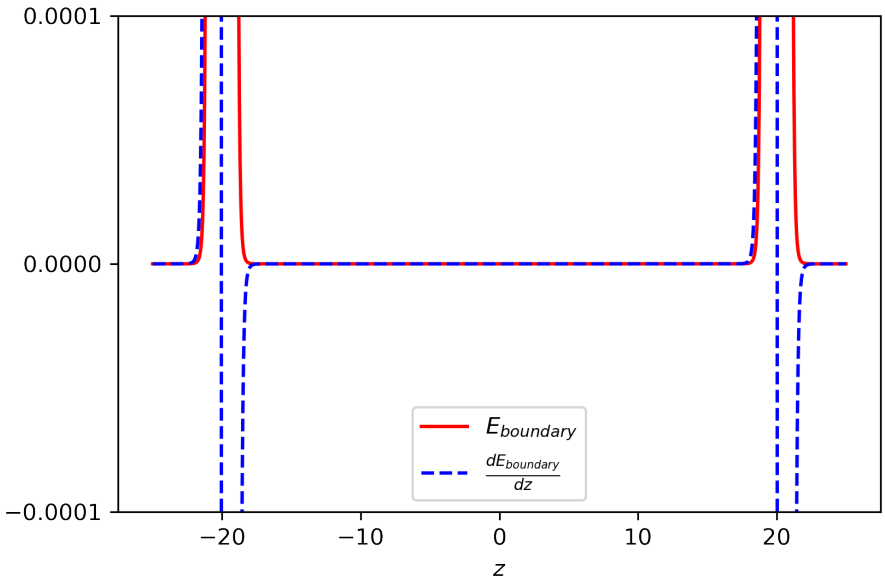

Figure 3.1: *The shape of the truncated, smoothed, shifted R^{-12} potential applied at the top and bottom of the truncated conical surface (here of height $h = 40$) to confine the Morse particles. Here, the cutoff value z_{cut} is set to 5.0 and not 1.0 to better show the shape of the potential. Both the energy $E_{boundary}$ and the gradient of the potential $\frac{dE_{boundary}}{dz}$ are shown.*

3.2 Large-Angle Cones: Magic, Intermediate and Near-Magic Angles

With the new treatment of the boundary conditions at $z = \pm\frac{h}{2}$ established, larger systems could be studied, here of up to $N = 200$. To begin with, conical surfaces of large angles were studied in an attempt to reproduce results from previous work but for a larger system size.[90] Angles of $\theta_{\text{max}} = 30°$ and above are considered large in this work. Cones of angles larger than those around $\theta_{\text{max}} = 120°$ are not discussed in this work as, for the system sizes employed here, conical surfaces of larger angles tend to create crystalline bands that are too narrow to analyse in terms of their defects. Cone angles on the net that are a multiple of 60° are special as they are commensurate with the rotational symmetry of a hexagonal lattice and can therefore host defect-free crystals, as noted by Law.[90] These cases are referred to as 'magic angles'.

Firstly, putative global minima of systems of size $N = 200$ on magic-angle cones were generated. These runs were carried out with Morse particles of potential range $\rho = 6$ and $\rho = 18$, and a truncation of $r_{\text{t}} = 1.0$ was used as standard in an attempt to separate out the effect of the peak of the cone. In agreement with previous work, minima on magic-angle cones of $\theta_{\text{max}} = \frac{n\pi}{3}$ (here $\theta_{\text{max}} = 60°$ and 120°, where $n = 1$ or 2) were defect free.[90] Visualisations of the putative global minima for the crystals on magic angle cones of $\theta_{\text{max}} = 60°$ using Voronoi tessellation are shown in parts (a) and (b) of Figure 3.2. The same but for cones of $\theta_{\text{max}} = 120°$ are shown in parts (a) and (b) of Figure A.1 in Appendix A.2. It can be seen in these figures that the defect-free nature of the crystals is independent of the range of the potential. As a reminder of and a reference for the colouration of the polygons:

- RED polygons are *pentagons*;
- GREEN polygons are *regular hexagons*;
- YELLOW polygons are *irregular hexagons*;
- BLUE polygons are *heptagons*;
- ORANGE polygons have a number of sides other than 5, 6 or 7 (although these are in almost all cases only a product of the visualisation method and not relevant

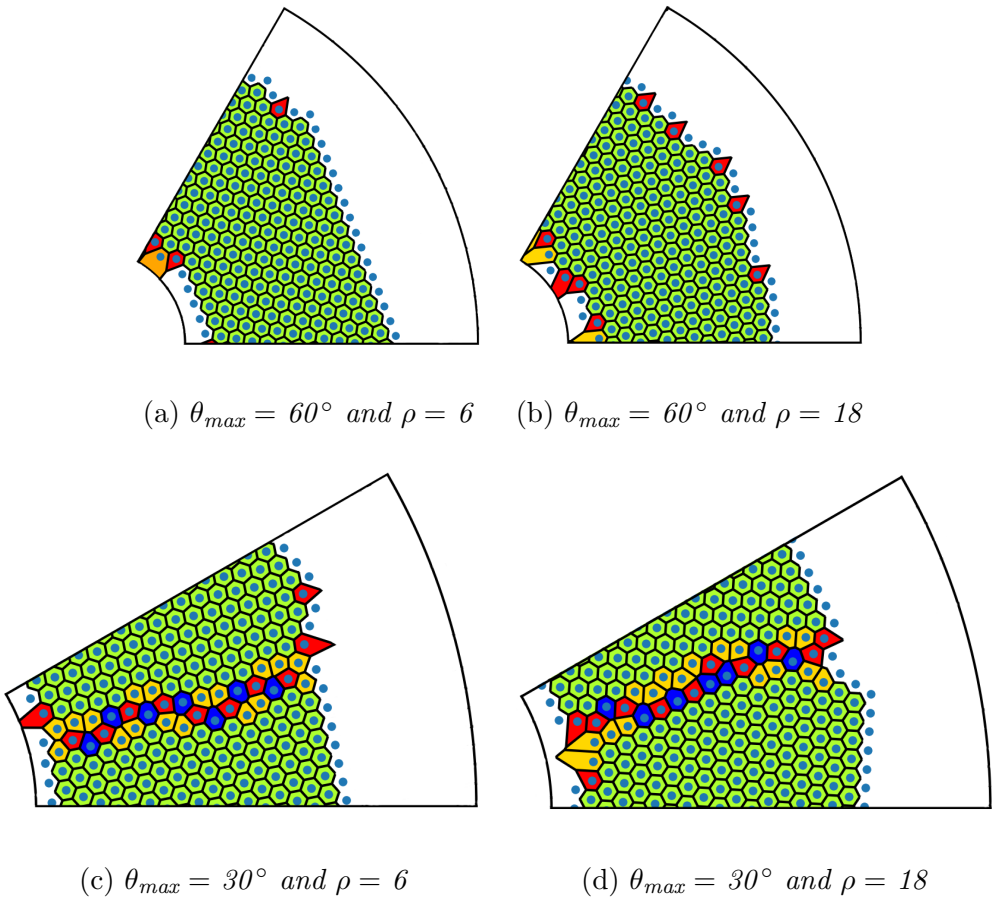

(a) $\theta_{max} = 60°$ *and* $\rho = 6$ (b) $\theta_{max} = 60°$ *and* $\rho = 18$

(c) $\theta_{max} = 30°$ *and* $\rho = 6$ (d) $\theta_{max} = 30°$ *and* $\rho = 18$

Figure 3.2: *Visualisations of the structures of crystals on magic and intermediate angle cones of* $\theta_{max} = 60°$ *and* $30°$ *with truncation radius* $r_t = 1.0$*. Each crystal is made of 200 particles. Equivalent visualisations of systems on cones of angle* $\theta_{max} = 120°$ *and* $90°$ *are shown in Figure A.1 in Appendix A.2.*

to the analysis of the crystal packing).

Recall that non-green polygons at the top and bottom edges (the top and bottom boundaries of the crystals in z) of the crystals that do not form part of a bigger defect in the crystal are, in general, anomalies that arise due to the visualisation method and should be ignored.

Minima on 'intermediate' angle cones (of angle halfway in between magic angles) were also produced. Cones of the intermediate angle $\theta_{\max} = 30°$ are shown in parts (c) and (d) of Figure 3.2. Conical surfaces have zero Gaussian curvature. Hence, the crystal packing on a section of a cone can be ideal, as seen on the magic angle cones in

parts (a) and (b) of Figure 3.2. However, when the end of the crystal wrapping around the cone and onto itself is not commensurate with itself, a complete, ideal crystal cannot be hosted. Thus, defects are introduced. On these intermediate angle cones, they consist of a complete chain of dislocations up and down the crystal. In effect, there is a tear in the crystal structure. Similarly to at magic angles, the structures of the defective crystals on the intermediate cone angles of $\theta_{\max} = 30°$ were seen to be qualitatively independent of the Morse potential range. The same is the case on conical surfaces of the next intermediate angle $\theta_{\max} = 90°$, which can be seen in parts (c) and (d) of Figure A.1 in Appendix A.2.

Subsequently, the same calculations were carried out at near-magic angles of $60° \pm 10°$ and $120° \pm 10°$. As before, they were carried out with two values of the range of the Morse potential, $\rho = 6$ and $\rho = 18$. The putative minima for cones of near the magic angle of $\theta_{\max} = 60°$ are shown in Figure 3.3 and those on cones of near the magic angle of $\theta_{\max} = 120°$ are shown in Figure 3.5. Angles of magic angle $\pm 10°$ were chosen to ensure that the wrapping of the crystal is sufficiently incommensurate to create defects; at angles nearer to the magic angle, often the crystals remained defect free, particularly in systems with the longer range potential. Considering first the longer range potential crystals with $\rho = 6$ on cones of angle $\theta_{\max} = 50°$ and $70°$, it can be seen that disclinations with topological charge of 0 are introduced by the crystal to deal with the non-commensurate nature of the overlap of the crystal edges. These appear as a neighbouring pair of red and blue polygons. In contrast, the short potential Morse crystals on surfaces of the same dimension deal with the strain in a different way; wedge-shaped voids, similar to those observed in experiment (see Figure 1.10), open up in the crystal packing. Below the magic angle, the wide end of the wedge points towards the narrow end of the cone and above the magic angle the opposite is the case. At the larger angles of $\theta_{\max} = 110°$ and $130°$, the same types of wedge-shaped voids appear in the short range potential crystal. However, the long range potential crystals on cones of these angles appear defect free. The differences in defect patterns in the systems with different interaction ranges is due to the way the strain is spread throughout the systems. The longer range potential distributes the strain throughout the system, while the shorter potential localises the strain. This is illustrated by the particle energy histograms in Figures 3.4 and 3.6. It can be seen that in the longer range potential crystals, the distribution of particle energies is more spread, whereas in

the crystals of shorter potential range the particle energies are more discretised around the integer values of energy. This reflects the way that the strain is localised by the shorter range potential by changing the coordination environments of a smaller number of particles drastically, rather than changing the environments of a larger number of particles slightly. Plots of the particles showing their energies are shown in Figures A.4 through A.7 inclusive in Appendix A.2. It can be seen that the higher energy particles are those with non-ideal coordination environments and are those grouped around the defects and the edges, as expected. In Figure A.4 in particular, the difference between the short and long range potentials is clear, with the strain being gradually spread out towards the defect and the bottom edge for the longer range potential and localised around the defect and edges for the shorter range potential crystal.

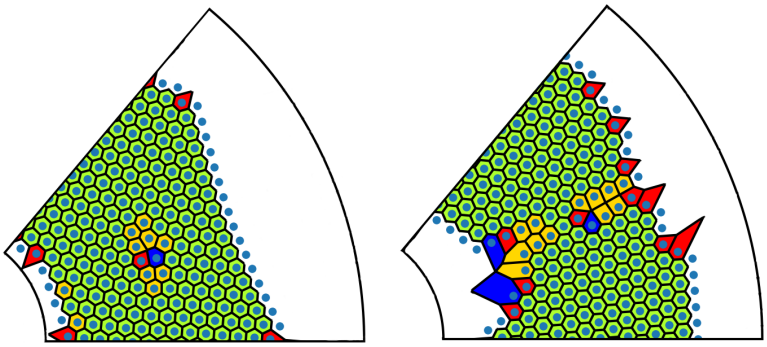

(a) $\theta_{max} = 50°$ *and* $\rho = 6$ (b) $\theta_{max} = 50°$ *and* $\rho = 18$

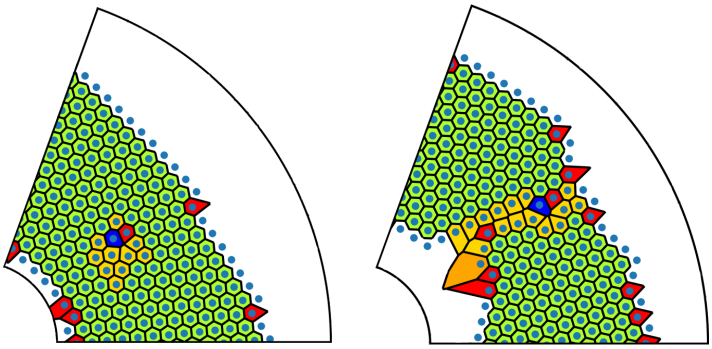

(c) $\theta_{max} = 70°$ *and* $\rho = 6$ (d) $\theta_{max} = 70°$ *and* $\rho = 18$

Figure 3.3: *Visualisations of the structures of putative global minimum energy crystals on near magic angle cones of* $\theta_{max} = 50°$ *and* $70°$*, all with truncation radius* $r_t = 1.0$*. Each crystal is made of 200 particles with Morse potential range of* $\rho = 6$ *or* $\rho = 18$*.*

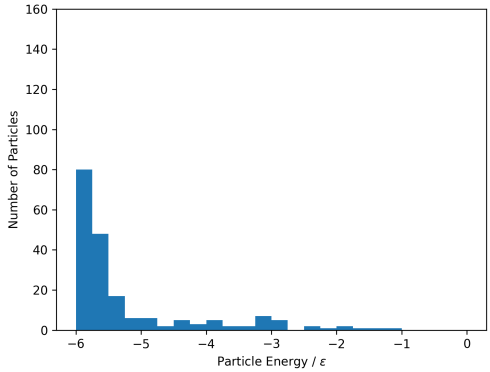

(a) $\theta_{max} = 50°$ *and* $\rho = 6$

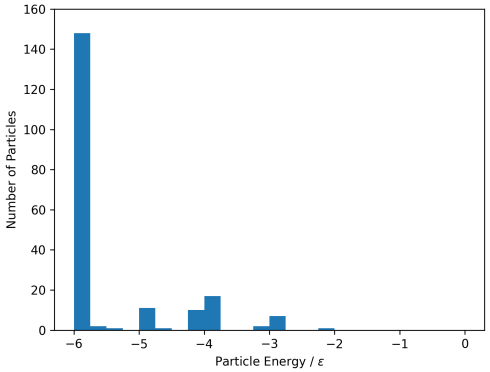

(b) $\theta_{max} = 50°$ *and* $\rho = 18$

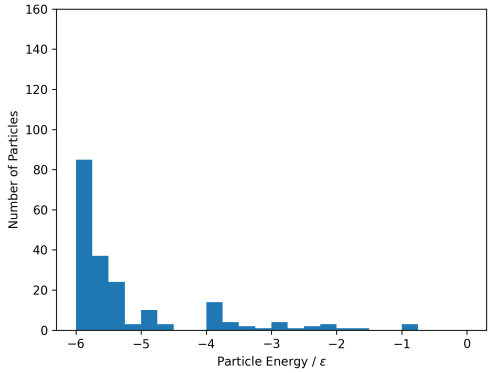

(c) $\theta_{max} = 70°$ *and* $\rho = 6$

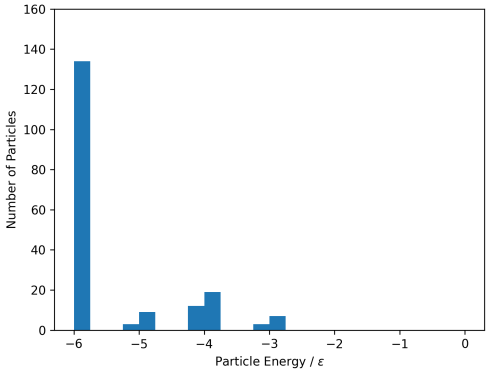

(d) $\theta_{max} = 70°$ *and* $\rho = 18$

Figure 3.4: *Histograms of particle energies in putative global minimum energy crystals of 200 particles on near-magic angle conical surfaces of* $\theta_{max} = 50°$ *and* $70°$*, all with truncation radius* $r_t = 1.0$ *with potential range* $\rho = 6$ *and* $\rho = 18$*.*

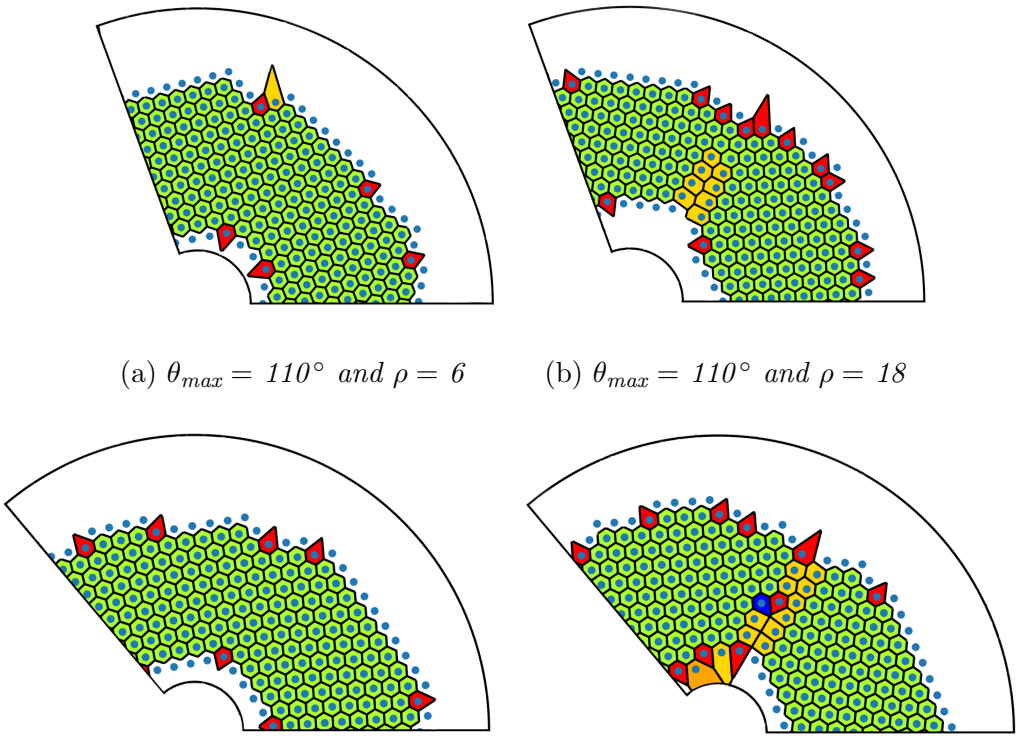

(a) $\theta_{max} = 110°$ *and* $\rho = 6$ (b) $\theta_{max} = 110°$ *and* $\rho = 18$

(c) $\theta_{max} = 130°$ *and* $\rho = 6$ (d) $\theta_{max} = 130°$ *and* $\rho = 18$

Figure 3.5: *Visualisations of the structures of putative global minimum energy crystals on near magic angle cones of* $\theta_{max} = 110°$ *and* $130°$*, all with truncation radius* $r_t = 1.0$*. Each crystal is made of 200 particles with Morse potential range of* $\rho = 6$ *or* $\rho = 18$*.*

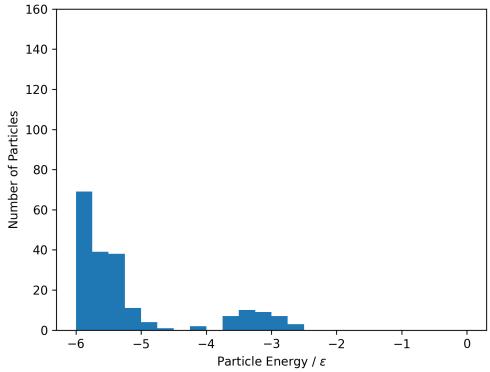

(a) $\theta_{max} = 110°$ *and* $\rho = 6$

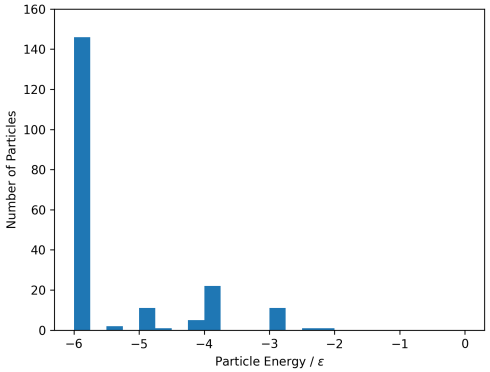

(b) $\theta_{max} = 110°$ *and* $\rho = 18$

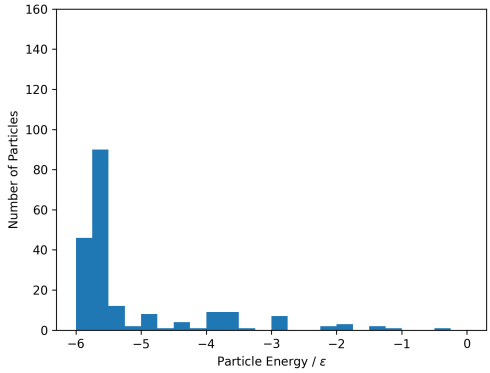

(c) $\theta_{max} = 130°$ *and* $\rho = 6$

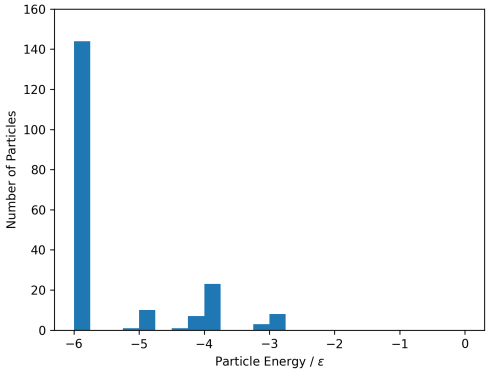

(d) $\theta_{max} = 130°$ *and* $\rho = 18$

Figure 3.6: *Histograms of particle energies in putative global minimum energy crystals of 200 particles on near-magic angle conical surfaces of* $\theta_{max} = 110°$ *and* $130°$*, all with truncation radius* $r_t = 1.0$ *with potential range* $\rho = 6$ *and* $\rho = 18$*.*

3.3 Small Angle/Near-Cylindrical Cones

After considering larger angle cones of $\theta_{\text{max}} = 30°$ and above, crystals on smaller angle cones of $\theta_{\text{p}} = 5.715°$ ($\theta_{\text{max}} = 0.313°$) and below were investigated. Note that going forwards, any cone angles referred to are θ_{p}, the angle of the cone in three dimensions and not θ_{max}, the angle of the net of the cone, as that was the convention used in the experimental work that guided this part of the investigation. The conversion between the two is shown in Equation 2.1 in Section 2.1 ($\theta_{\text{max}} = 2\pi \sin\{\theta_{\text{p}}/2\}$). To begin with, crystals on conical surfaces of similar dimensions to those investigated in the experiment were simulated with values of Morse potential range ρ from $\rho = 18$ (closest to experiment) to $\rho = 6$ (longest range).

3.3.1 Analysis and Categorisation of Defect Structures

There were a number of different defect types observed in these small-angle systems. Except for the edge-terminating helical defect in part (b) of Figure 3.9, all of the defects on the conical surfaces originate from dislocations, or red-blue polygon pairs, as the surfaces have zero Gaussian curvature. Examples of the observed types are shown in Figures 3.7 through 3.10. They include: simple dislocations (Figure 3.7); wedge-shaped voids (Figure 3.8); edge- and bulk-terminating helices (Figure 3.9); and compound/hybrid defects including 'L-shapes' and double wedges (Figure 3.10).

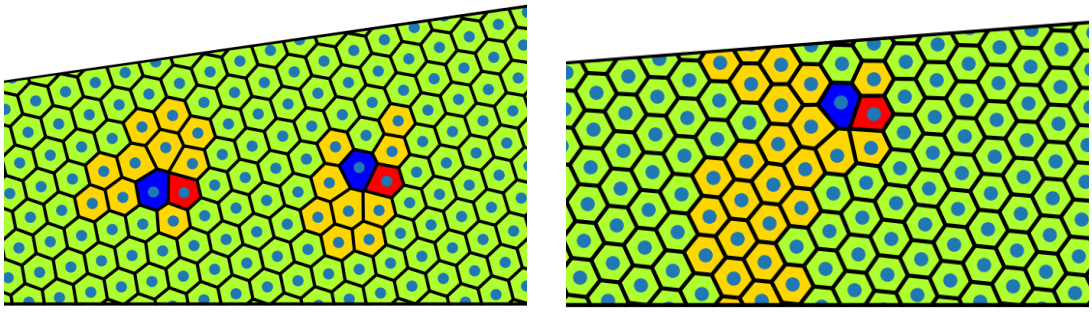

(a) $\theta_p = 2.6°$ ($\theta_{max} = 0.143°$) and $\rho = 6$ (b) $\theta_p = 1.4°$ ($\theta_{max} = 0.077°$) and $\rho = 6$

Figure 3.7: *Examples of dislocation defects observed in small-angle, minimum energy Morse crystal structures. Two localised dislocation defects are shown in (a) and one extended dislocation defect is shown in (b).*

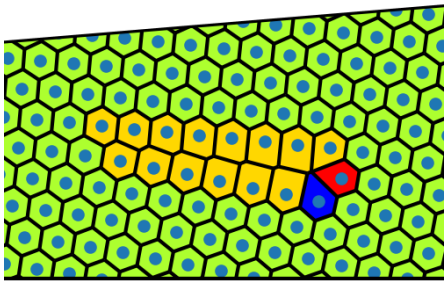

Figure 3.8: *A wedge defect observed in small-angle, minimum energy Morse crystal structures. This defect was observed at* $\theta_p = 1.5°$ *(*$\theta_{max} = 0.082°$*) and* $\rho = 15$*.*

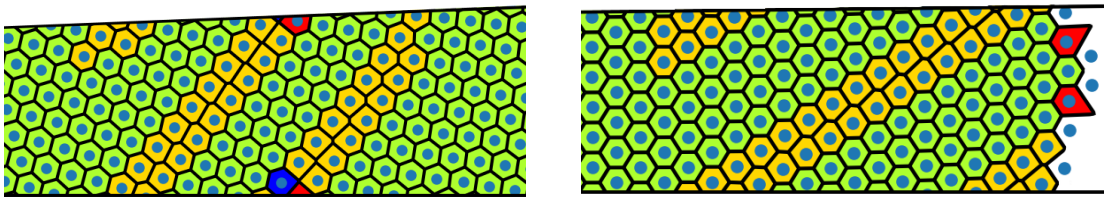

(a) $\theta_p = 0.7°$ *(*$\theta_{max} = 0.038°$*) and* $\rho = 15$ (b) $\theta_p = 0.3°$ *(*$\theta_{max} = 0.016°$*) and* $\rho = 15$

Figure 3.9: *Examples of helical defects observed in small-angle, minimum energy Morse crystal structures. A complete, bulk-terminating helical defect is shown in (a) and an incomplete, edge-terminating helical defect is shown in (b).*

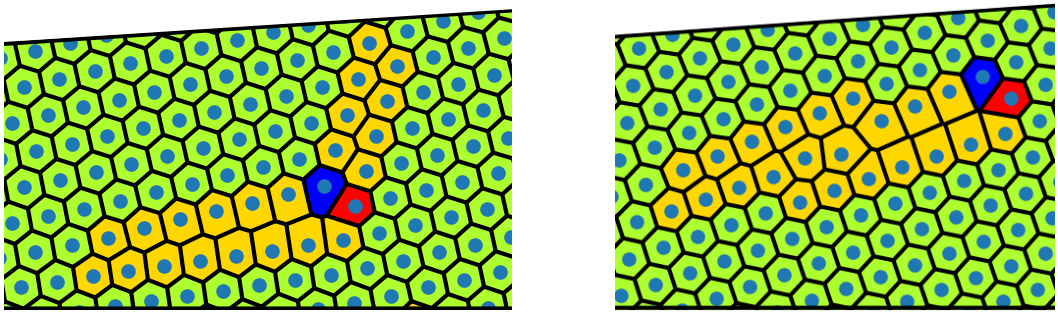

(a) $\theta_p = 1.2°$ *(*$\theta_{max} = 0.066°$*) and* $\rho = 15$ (b) $\theta_p = 1.3°$ *(*$\theta_{max} = 0.071°$*) and* $\rho = 18$

Figure 3.10: *Examples of hybrid/compound defects observed in small-angle, minimum energy Morse crystal structures. A hybrid 'L-shaped' defect is shown in (a) and a compound double wedge defect is shown in (b).*

To deal with the variety of structures observed, an automatic analysis and categorisation algorithm was developed. It proceeds as follows:

1. Voronoi analysis of the minimum energy structure is carried out on its net;
2. The largest collection of neighbouring non-green polygons on the surface is identified as the primary defect. If the defect is not complete in one copy of the net (i.e. it wraps around the cone) then a complete version is reconstructed by periodically repeating the net;
3. The largest complete defect is analysed. Analyses include:
   (a) Calculating the location of the centre of mass of the defect;
   (b) Calculating the total moment of inertia of the system;
   (c) Calculating the directions of all of the vectors between every pair of particles in the defect;
   (d) Identifying the all chains of three or more particles in a line in the defect;
   (e) Determining if the defect contains a red/blue polygon pair;
   (f) Calculating the angle between all of the neighbouring chains of particles three or more particles long;
4. The defect is categorised using the above information gathered about the defect.

The decision tree applied to categorise the minima is shown in Appendix A.3. Using this categorisation procedure, a kind of phase diagram was constructed to more comprehensively illustrate the effect of cone angle θ_{p} and potential range ρ on the types of defect structure observed in the putative global minimum crystals. The diagram is shown in Figure 3.11. Note that in cases where multiple defect types coexist, the structures were confirmed manually.

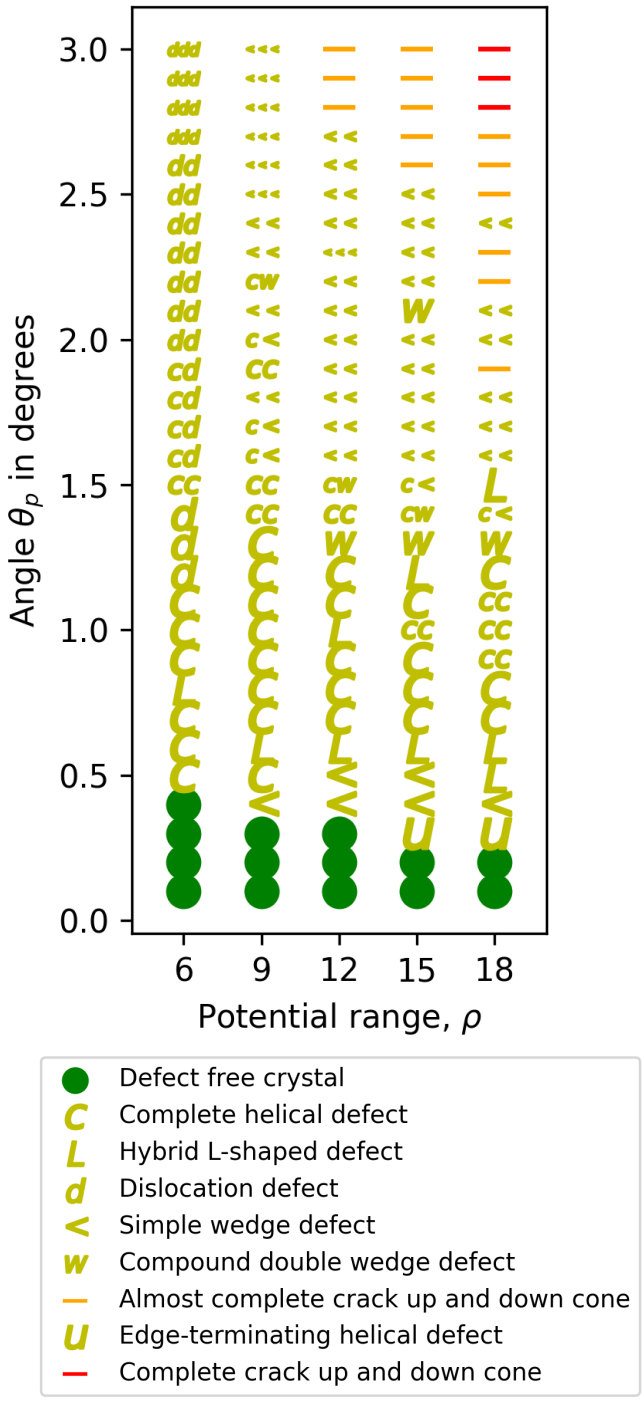

Figure 3.11: *An effective 'phase diagram' showing effect of potential range ρ and cone angle θ_p on the defect type observed in putative global minimum energy Morse crystals. For a point on the diagram labelled with two or three distinct defects, the two or three listed types were seen to coexist in the structure.*

3.3.2 Trends

Although the 'phase diagram' in Figure 3.11 is complex, there are some clear trends to be observed. For all values of the potential range ρ, the crystal minima go from defect free at low θ_{p} to a succession of defects that line up from the top to the bottom of the crystal band. At shorter range potentials, at $\theta_{\mathrm{p}} = 3.0^{\circ}$ ($\theta_{\mathrm{max}} = 0.164^{\circ}$), these merge to form a complete crack in the crystal structure and indeed for $\rho = 18$, the structures tend to those seen at the intermediate angle of $\theta_{\mathrm{max}} = 30^{\circ}$ (shown in Figure 3.2). At longer range potentials, at $\theta_{\mathrm{p}} = 3.0^{\circ}$ ($\theta_{\mathrm{max}} = 0.164^{\circ}$) the defects stay distinct and the crystal stays more intact. It can be expected that the structures with $\rho = 6$ would also tend to the structure observed for that potential range at $\theta_{\mathrm{max}} = 30^{\circ}$ if the angle were increased beyond $\theta_{\mathrm{p}} = 3.0^{\circ}$ ($\theta_{\mathrm{max}} = 0.164^{\circ}$).

At the intermediate values of angle in Figure 3.11, the defect structures are more interesting. In general, at lower values of θ_{p}, singular defects appear in the crystal structure to alleviate the strain created by the closure constraint on the cones, and then at higher values of θ_{p}, more than one defect is introduced to deal with the greater amount of strain. The longer the range of the potential, the larger angle at which the first, second and then third defects are introduced to the structure.

As with the crystals on large angle cones, there is a trend in the way the strain is dealt with against the range of the potential of the Morse particles. The shorter the range of the potential, the more localised the strain. The loss of defect-free crystals as the putative global minimum also depends on the range of the potential. At $\rho = 6$, a defect-free crystal is observed at angles as large as $\theta_{\mathrm{p}} = 0.4^{\circ}$ ($\theta_{\mathrm{max}} = 0.022^{\circ}$), whereas for a crystal with $\rho = 18$ the defect free crystal only persists at angles as large as $\theta_{\mathrm{p}} = 0.2^{\circ}$ ($\theta_{\mathrm{max}} = 0.011^{\circ}$).

The energies of the putative global minima structures are plotted in Figure 3.12 against the angle of the surface. It can be seen that the shorter the range of the potential in the Morse crystals, the higher energy the putative global minimum structure has at a given angle θ_{p}. Further, it can be seen that for all values of ρ investigated here, in general, the larger the angle of the conical surface, the higher the energy of the global minimum. This makes sense as the higher angle conical surfaces introduce a greater amount of strain energy into the system. From $\theta_{\mathrm{p}} = 0.1^{\circ}$ ($\theta_{\mathrm{max}} = 0.005^{\circ}$) to $\theta_{\mathrm{p}} = 3.0^{\circ}$ ($\theta_{\mathrm{max}} = 0.164^{\circ}$), the overlap of the crystal around the cone and onto itself only gets

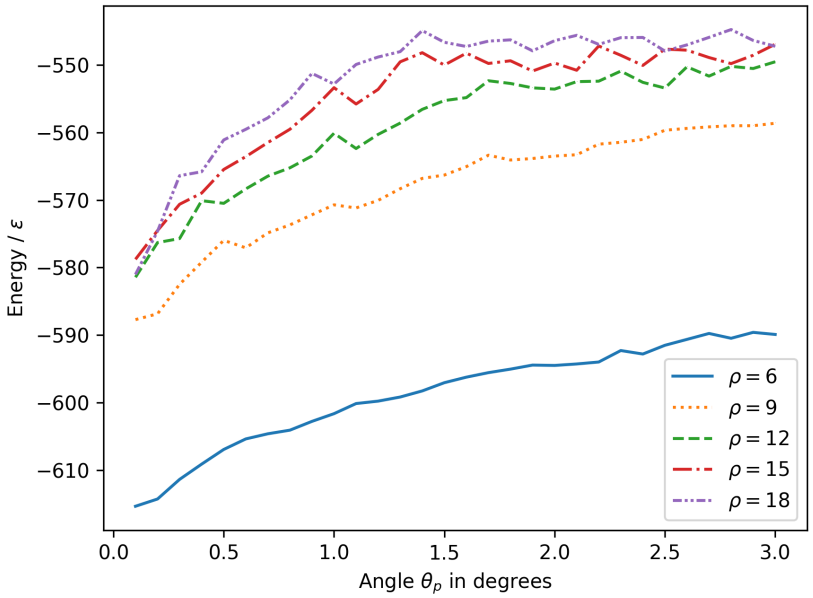

Figure 3.12: *A plot to show the relationship between the overall system energy of putative global minimum energy Morse crystals of 200 particles confined on truncated conical surfaces and the angle θ_p of the conical surfaces for five values of potential range ρ.*

more incommensurate; if the angle were increased beyond $\theta_{\mathrm{p}} = 3.0°$ ($\theta_{\mathrm{max}} = 0.164°$) it would reach a maximum at $\theta_{\mathrm{max}} = 30°$ and reduce to zero the next value of magic angle at $\theta_{\mathrm{max}} = 60°$, where it can overlap with itself perfectly again. It appears that for all values of ρ, the increases in energy of the systems begin to tail off at higher angles, as once the structure introduces a full tear into the crystal, more strain does not further disrupt the structure. The shorter the range of the potential, the lower the angle at which this tailing off starts to occur.

It is also worth noting that the energy plots for longer range potentials are smoother than those for short range values of ρ. This reflects the ease with which the true global minimum can be found — the longer the range of the potential, the smoother the PES and the easier the system is to converge.

3.3.3 Defect Analysis

As discussed earlier, defect-free crystal structures are present on the very smallest angle conical surfaces across the whole $\rho = 6$ to $\rho = 18$ potential range. Conical surfaces of such small angle are near-cylindrical, and cylindrical surfaces can also host defect free crystals. There is still strain in these structures, however, despite the lack of defects. The strain is spread throughout the structures, warping them slightly. The lattice can be warped in one of two ways: by stretching the 'bonds' between the particles and holding them in tension, or by squeezing the particles closer together, in compression. This tension or compression of the lattice can occur in any of the three lattice directions. A defect-free crystal is shown in Figure 3.13 with bond vectors visualised. The bond vectors are coloured based on the angle within their sector. It can be seen that all angles pointing down the cone are slightly larger than those pointing up the cone; the strain is incorporated into the crystal structure all the way through it. This can be seen as a spreading of the bond angles moving down the cone; bond lengths are slightly larger at the bottom of the cone than they are at the top. This can be seen qualitatively as the cluster of red angles being centred closer to 30° (between 28 and 29°) than the cluster of blue angles (between 32 and 33°). It is likely that if the system was larger, at some point a defect would be introduced to the structure, as the lattice would continue to spread down the cone and the bond lengths would become too large to be stable. In the third direction, around the cone circumference, there is no change in vector moving up and down the cone. An alternative defect-free structure with a different overall lattice rotation at the larger cone angle of $\theta_{\mathrm{p}} = 0.2°$ ($\theta_{\mathrm{max}} = 0.011°$) is shown in Figure A.8 in Appendix A.4. The defect-free structure on this larger-angle surface is of higher energy due to the increased strain created by the larger angle. The strain in the two defect-free structures is dealt with slightly differently; the lattice in the structure on the $\theta_{\mathrm{p}} = 0.1°$ ($\theta_{\mathrm{max}} = 0.005°$) cone gradually spreads out down the cone giving three separate clusters of angles (different angles pointing up, down and across the cone), whereas the rotation of the lattice on the cone of $\theta_{\mathrm{p}} = 0.2°$ ($\theta_{\mathrm{max}} = 0.011°$) means the lattice cannot spread out symmetrically in the direction of the circumference of the cone in the same way. The rotation must allow the structure to accommodate the strain differently, as shown by the fact that there are two clusters of angles rather than three. It seems that the rotation is better at dealing with the strain than the spreading

of the lattice given it occurs at higher θ_p.

Localised dislocations are observed at longer range potentials. An example of two localised dislocations is shown in part (a) of Figure 3.7. They appear as a pair of red and blue polygons. At higher angles, more of these defects appear lined up in the crystal lattice to relieve the greater strain energy. At a few values of θ_p at $\rho = 6$, namely $\theta_p = 1.2°$, $1.3°$ and $1.4°$ ($\theta_{max} = 0.066°$, $0.071°$ and $0.077°$), extended versions of these defects appear, as shown in part (b) of Figure 3.7. They create a zig-zag pattern of irregular hexagonal environments that loops all the way around the conical surface.

At shorter range potentials, these localised dislocations are not observed. Instead, wedge-shaped voids form in the crystal lattice, not unlike those observed in experiment (see Figure 1.10). These are the same type of defect as are observed in the short range potential near-magic angle structures discussed in Section 3.2 and shown in Figure 3.3. An example of the type of wedge-shaped void seen at these small angles is shown in Figure 3.8. It was observed that the wedges form pointing around the circumference at lower θ_p and up and down the cone axis at higher θ_p.

At small angles, another kind of defect is observed: helical defects, which are long and wrap around the cone. These are referred to as helices or helical defects in this work but are sometimes referred to line slips elsewhere. These helices are observed to both terminate freely in the bulk at two ends, or terminate in the bulk at one end and the edge at the other. An example of each of these types of helix are shown in Figure 3.9. The edge-terminating helices do not contain a five-/seven-fold coordination environment pair dislocation, whereas the complete helices do. The edge-terminating helix, which are like a tear in the crystal lattice, has been observed in experiment by Jessica Sun in the Manoharan Lab. Helical defects that are as long as the crystal and that do not terminate in the bulk have been observed in cylindrical crystals.[127] These defects are not seen at high θ_p and so it can be inferred that they resolve the strain in a less severe way than the wedges, dislocations and scars seen at higher θ_p. In Figure 3.14, it can be seen that the helical defect facilitates a gradual rotation of the lattice vector down the cone axis. When these defects appear at higher values of θ_p, the helix angle relative to the cone axis becomes larger and the helix is 'tighter'. This is because the system must alleviate the greater strain more dramatically with a more rapid rotation of the lattice vector along the cone axis. In Figure 3.15, the bonds

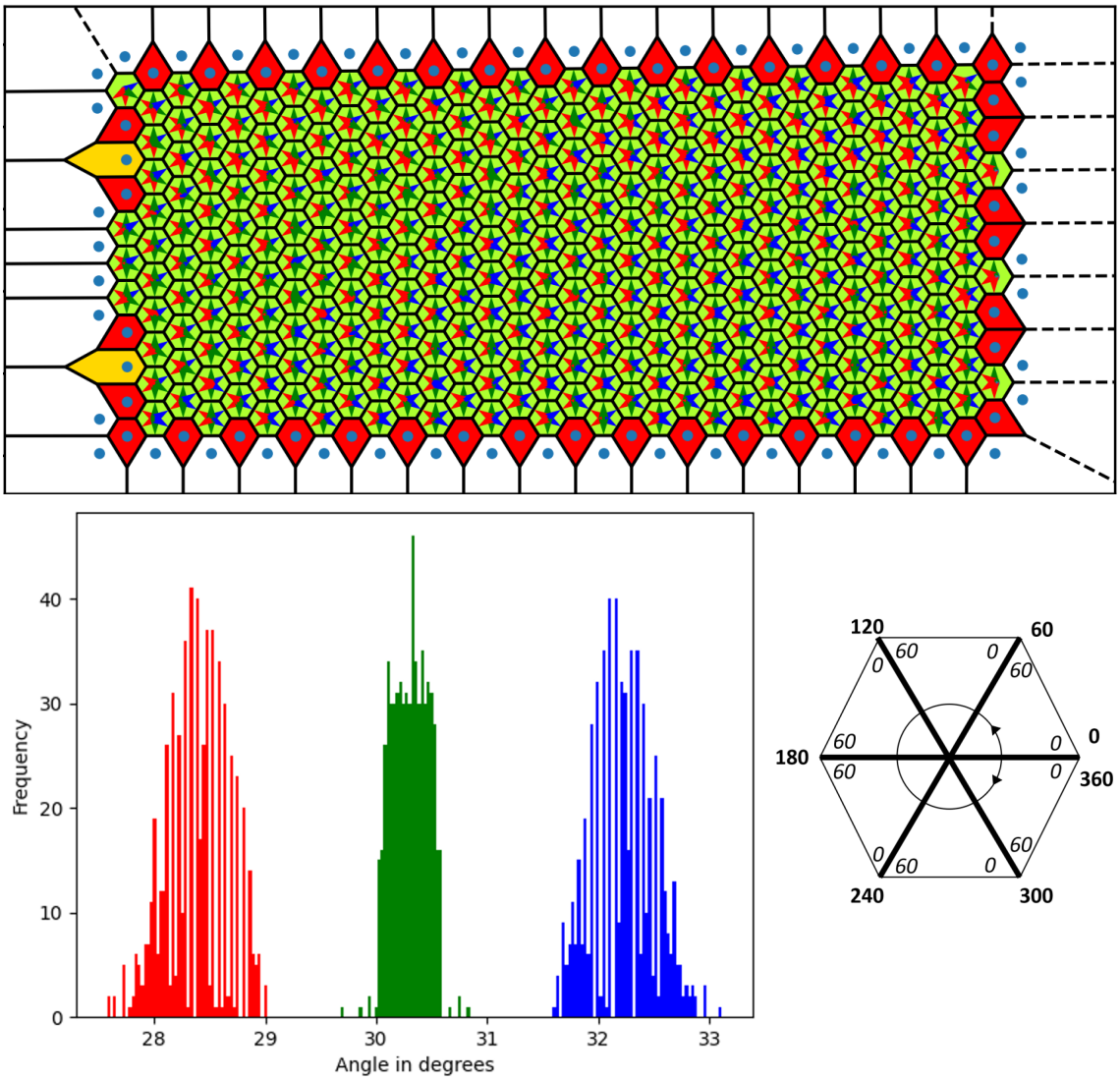

Figure 3.13: *A plot of bond vectors in a defect-free crystal observed at $\rho = 18$ and $\theta_p = 0.1°$ ($\theta_{max} = 0.005°$). The accompanying histogram shows the frequency of angles and the chosen colour scheme. Here, the angles are measured within their local 60° sector in a clockwise direction for those in the top half of a cell and anticlockwise for those in the lower half. A diagram showing how the angles are measured is also shown. The structure on the net is periodically repeated in ϕ by 2π to better illustrate the defect pattern.*

between each pair of particles (where one of the pair is in a green cell) are plotted and coloured by their length. This visualisation shows that, moving down the cone, more tension is introduced in one lattice direction (shown by longer bonds) and also that the helical defect alleviates that increased tension through a 'reset' of the bond lengths. This is done by facilitating a step increase in the number of particles in each row across the defect.

Although the above defect types form the basis for almost all of the defective structures observed across the minimum energy structures of 200 particle Morse crystals of $\rho = 6$ to $\rho = 18$ on conical surfaces of angle $\theta_{\mathrm{p}} = 0.1^{\circ}$ ($\theta_{\mathrm{max}} = 0.005^{\circ}$) to $\theta_{\mathrm{p}} = 3.0^{\circ}$ ($\theta_{\mathrm{max}} = 0.164^{\circ}$), often they do not appear in the idealised forms discussed above. Hybrid defects appear in local minimum structures frequently. One such structure appears to be a combination of a wedge-like void and a helical defect. Such an 'L-shaped' defect is shown in part (a) of Figure 3.10. Another type of hybrid defect that appears is the compound wedge defect (where two or more wedge-shaped voids link up), shown in part (b) of Figure 3.10.

All of the above defect types are in competition with each other. At certain values of angle, certain defects dominate. The lack of distinction between defect 'phases' can be attributed in part to how close in energy the competing defect structures often are. It can be challenging, given all the degrees of freedom in play, for very similar energy minima to be distinguished. Attempts were made to determine the energy of each defect type across a range of values of angle by seeding the defect structures and thus determining the precise ranges of angle over which each defect is dominant, but the difficulty of separating the defect energy from the position and rotation of the crystal on the cone prevented this from being done effectively. This is because by performing basin-hopping steps at each new value of angle, a shift in crystal location or rotation prevents the structures from being directly comparable.

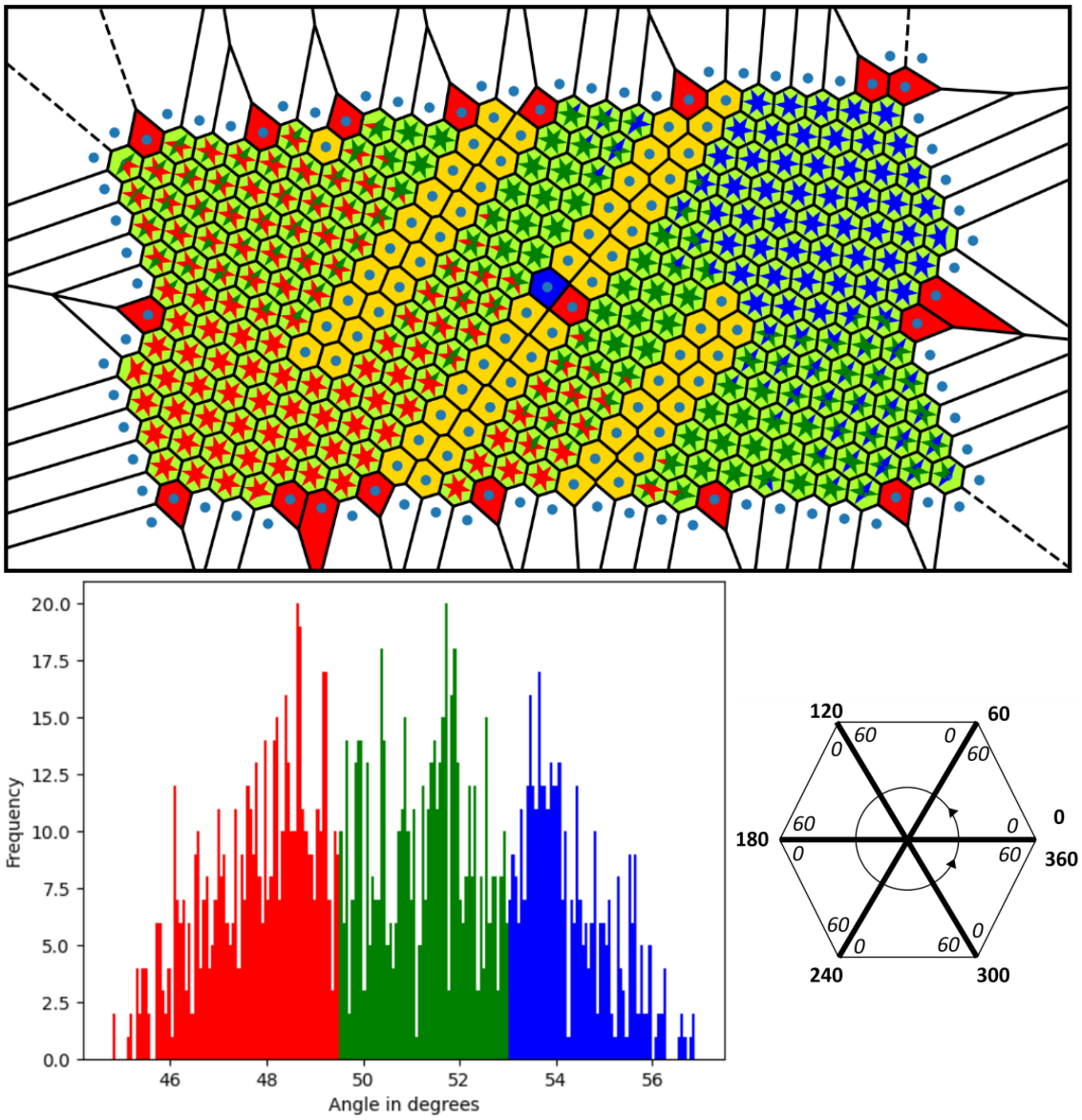

Figure 3.14: *A plot of bond vectors in a crystal hosting a helical defect observed at $\rho = 18$ and $\theta_p = 0.7°$ ($\theta_{max} = 0.038°$). The accompanying histogram shows the frequency distribution of angles and the chosen colour scheme. Three distinct colours are chosen here to illustrate the variation in angle through the structure, not to show three distinct sets of angles. Here the angles are all measured in a clockwise direction within their 60° sector. A diagram showing how the angles are measured is also shown. The structure on the net is periodically repeated in ϕ by 2π to better illustrate the defect pattern.*

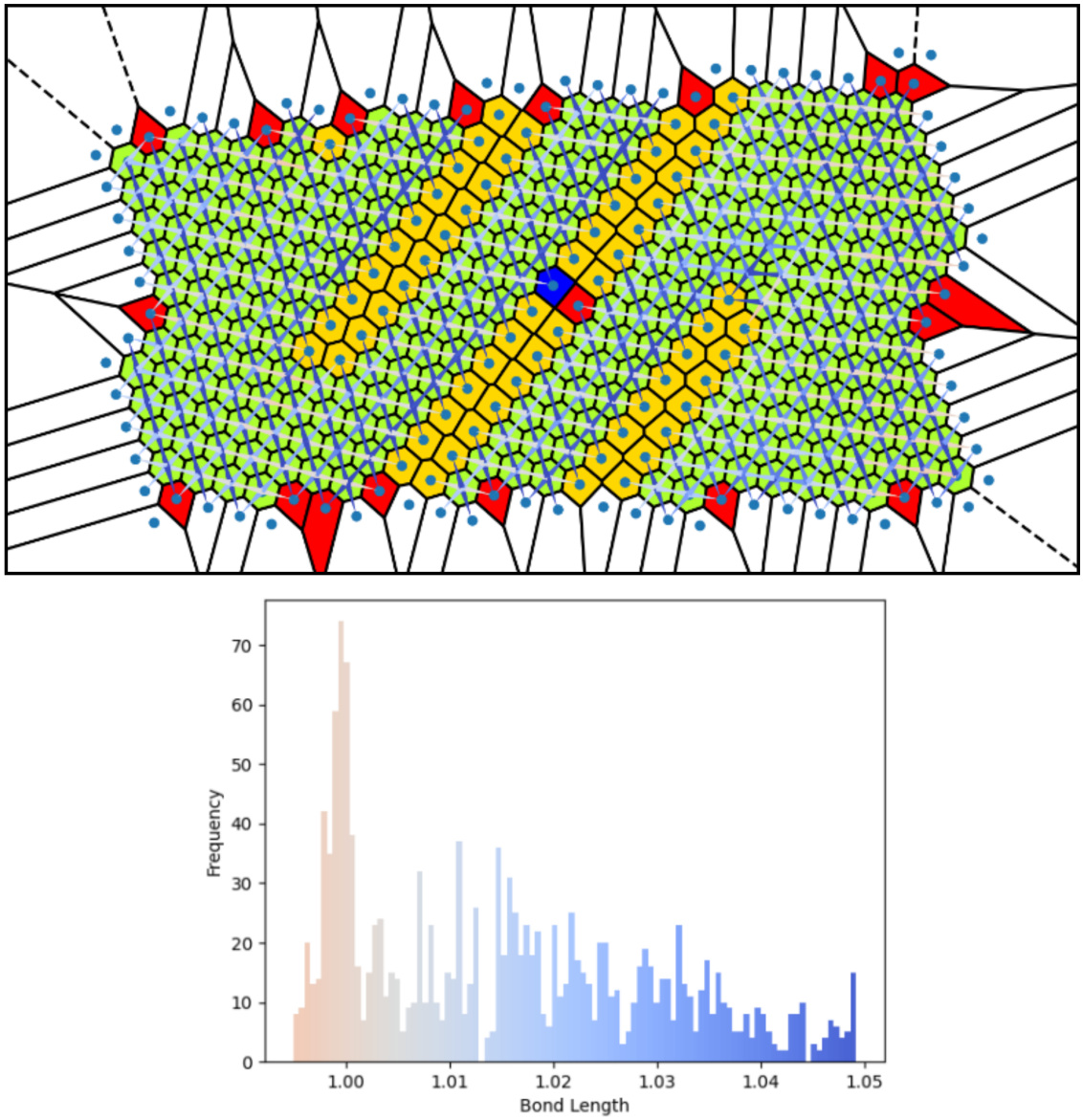

Figure 3.15: *A plot of bond lengths in a crystal hosting a helical defect observed at* $\rho = 18$ *and* $\theta_p = 0.7°$ *(*$\theta_{max} = 0.038°$*). The accompanying histogram shows the frequency distribution of bond lengths and the chosen colour scheme. The structure on the net is periodically repeated in* ϕ *by* 2π *to better illustrate the defect pattern.*

3.4 The Effect of the Dimensions of the Conical Surface on the Crystal Location - A Simple Model

All of the Morse crystal systems generated in this work sit on a surface larger than the size of the condensed crystal system. To approximate the area which the crystal takes up, the following was used:

$$Area = N(\pi r^2)\left(\frac{6}{\pi\sqrt{3}}\right) \tag{3.1}$$

where N is the number of particles in the crystal, r is their radius and $\frac{\pi\sqrt{3}}{6}$ reflects the proportion of space taken up by spheres when they are ideally packed on a two-dimensional surface. Thus for $N = 200$ and $r = 1.0$, an ideal crystal of 200 particles would therefore occupy approximately 173 squared units. In reality, the non-ideal crystal packing means the area of the crystal will be slightly larger, but not by much. The system area is set to just over 292 squared units as standard. Thus, the crystal has a reasonable amount of room within which it can move, so during the basin-hopping it can move up or down the cone.

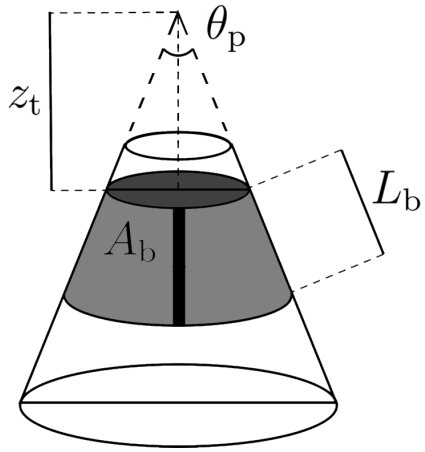

Figure 3.16: *An illustration of the simple band model of the crystal with key dimensions labelled. The band of crystal is shown in grey and has area A_b. The thick black line up and down the band is the model defect and its length corresponds to L_b.*

To try to explain the behaviour observed in the simulations, a simple model was developed. It was postulated that the position of a crystal of fixed area on the cone represents a trade-off between the length of the edges of the crystal (and the line energy associated with that length) and the length of a scar defect through the crystal (and the line energy associated with that length), from the top to the bottom of the band. The higher up the conical surface a band of constant area sits, the shorter the edges of the crystal and the longer the scar is through it. Also, the larger the angle of the cone, the thinner the band at a given height on the cone. This model is clearly only relevant for values of θ_p which are high enough that a complete scar forms through the crystal. An illustration of this simple model is shown in Figure 3.16.

The thickness of the band L_b (equal to the length of the defect in this model) as a function of the distance from the top of the cone to the top of the crystal band z_t, the area of the band A_b and the cone angle θ_p was found to be

$$L_\mathrm{b} = \frac{A_\mathrm{b}}{\pi \tan\frac{\theta_\mathrm{p}}{2}\left[z_\mathrm{t} + \sqrt{\frac{A_\mathrm{b}\cos\frac{\theta_\mathrm{p}}{2}}{\pi\tan\frac{\theta_\mathrm{p}}{2}} + z_\mathrm{t}^2}\right]} \tag{3.2}$$

and the total length of both edges of the crystal band L_c as a function of the same parameters was calculated to be

$$L_\mathrm{c} = 2\pi\tan\frac{\theta_\mathrm{p}}{2}\left[z_\mathrm{t} + \sqrt{\frac{A_\mathrm{b}\cos\frac{\theta_\mathrm{p}}{2}}{\pi\tan\frac{\theta_\mathrm{p}}{2}} + z_\mathrm{t}^2}\right]. \tag{3.3}$$

The derivations for Equations 3.2 and 3.3 are shown in Appendices A.5 and A.6 respectively.

Thus, by weighting these two functions with their energy per unit length and finding the minimum energy of the sum of the two functions for a given area A and cone angle θ_p, an approximation of the preferred position of the band on the cone can be found. To find approximations of the energy per unit length of the model defect and the edges of the crystal band, calculations were made based on a range of crystals produced by basin-hopping calculations. The energy per length of the edges and of the defects were calculated from the crystal structures as follows:

1. The Voronoi tessellation procedure was carried out on the structure on the net;

2. The particles in pentagonal, heptagonal and irregular hexagonal Voronoi cells were identified (these particles are all of those in the defect or at the edge of the crystal);

3. The edge and defect particles were differentiated. This was done as follows:

   (a) An edge/defect particle was selected;

   (b) A second, neighbouring edge/defect particle was selected;

   (c) The midpoint between the neighbours was found;

   (d) The number of other particles within 0.9 distance units of the midpoint between the pair was counted. If the number is one, then the particle is on the edge. If it is two, then the particle is in the defect.

4. The average energy of all line and defect particles was calculated;

5. The length of the edges and the defect were calculated. This was done as follows:

   (a) The edge particles were split into particles on the top edge and those on the bottom edge by finding which were above and below the average of the z values of the particles with the highest and lowest values of z;

   (b) The average z of the particles on each edge were calculated;

   (c) The circumference of the cone at the average z of the top and bottom edges was calculated and taken as the lengths of the top and bottom edges;

   (d) The slope length between the average z of the top edge particles and the average z of the bottom edge particles was taken as the defect length.

6. The average number of particles per unit length in the defect and on the edges were calculated;

7. The energy per length of the edges were calculated from the average edge particle energy and the average number of particles per unit length in the edge with the following formula:

$$E_{\text{per length, Edges}} = N_{\text{per length, Edges}} E_{\text{per particle, Edges}}$$

	No. Particles/Length	**Energy/Particle**	**Energy/Length**
Defect	1.96	1.53	3.01
Edges	1.01	2.09	2.11

Table 3.2: *Values of energy per length, energy per particle and particles per length for the line defect in and the edges of the crystal band gathered from 11 200 particle putative global minimum energy crystal structures on conical surfaces of $r_t = 1.0$–2.0.*

8. The energy per length of the defect was calculated from the average defect particle energy and the average number of particles per unit length in the defect with the following formula:

$$E_{\text{per length, Defect}} = N_{\text{per length, Defect}} E_{\text{per particle, Defect}}$$

With this method, the average values shown in Table 3.2 were calculated from 11 different crystal structures with potential range $\rho = 18$ of $N = 200$ on cones of $\theta_{\text{p}} = 5.715°$ ($\theta_{\text{max}} = 0.313°$), $A = 292.1681168$ and values of r_{t} from 1.0 to 2.0. These values were used as the line energies of the crystal defects and edges. The resulting model is plotted in Figure 3.17. The minimum energy position of the crystal predicted by this model is shown in Table 3.3.

To check the validity of the model, the true global minimum position of the crystal on the cone at given angles would ideally be required. However, this is difficult given the complexity of the PES; the basin-hopping algorithm does not find it easy to translate the full crystal up and down the cone. Instead, in this analysis, values of total system energy against crystal position as measured from a series of different crystal minima on surfaces with $\theta_{\text{max}} = 5.715°$ ($\theta_{\text{max}} = 0.313°$) sitting at different points on the cone are used. A plot of these values is shown in Figure 3.18, and a simple second order polynomial fit is overlaid to illustrate how the minimum energy position was found. The minimum energy position is given in Table 3.3.

The model successfully captures the qualitative behaviour of the crystals, but the minimum energy position of the model is different to that calculated from the putative minimum energy structures by a factor of 1.43. This discrepancy could reflect a number of assumptions made by the model including: the straightness of the line defect (in every putative global minimum energy structure it is not perfectly straight and in

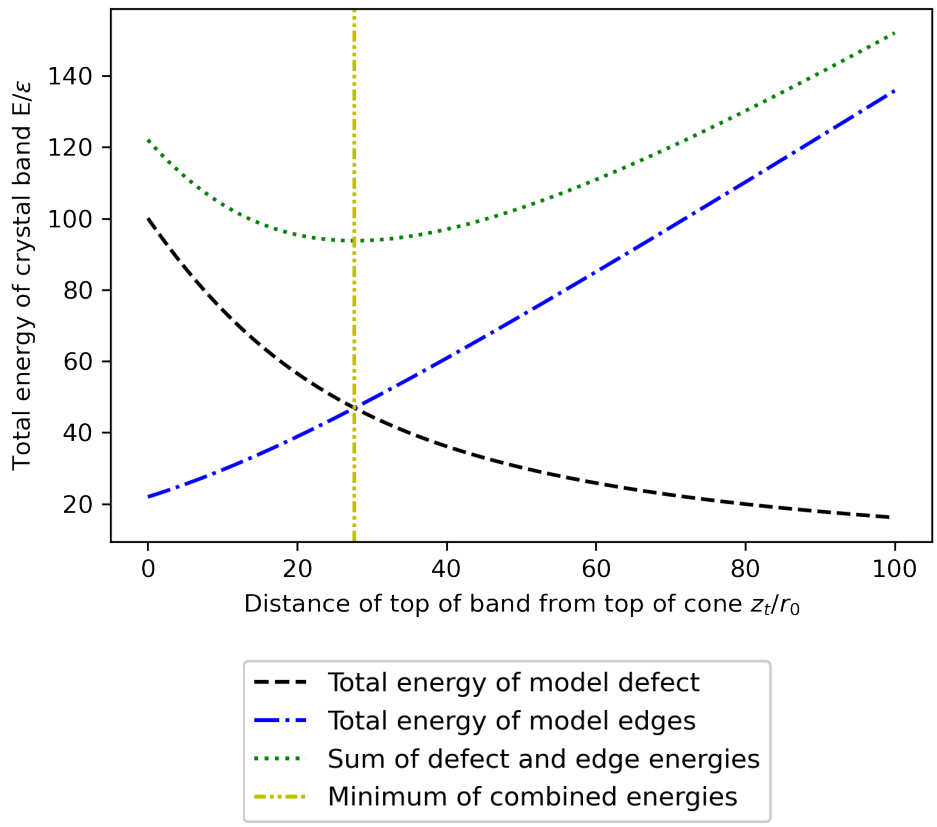

Figure 3.17: *The simple band model of the cone, showing the weighted energies of the defect, the edges and the sum of the two. The model is applied to a surface of* $\theta_p = 5.715°$ *(*$\theta_{max} = 0.313°$*), and the available surface shown has* $r_t = 1.0$ *and* $A = 292.1681168$*. The minimum energy position of the top of the crystal band according to this model is 27.671.*

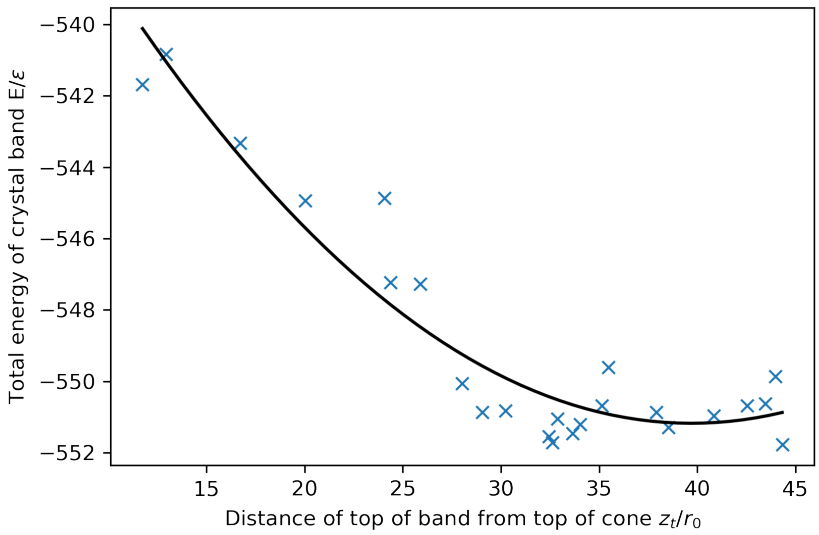

Figure 3.18: *A plot of total energy against crystal position of a number of putative global minimum energy Morse crystals of size $N = 200$ on conical surfaces of $\theta_p = 5.715°$ ($\theta_{max} = 0.313°$) and $A = 292.1681168$. A simple, second order polynomial fit is superimposed onto the data and was used to find the minimum energy position. The minimum energy position of the top of the crystal band according to the model is at 39.699. For all crystals the Morse potential range is set to $\rho = 18$.*

	Minimum Energy Position of Top of Band
Model	27.7
Simulation	39.7

Table 3.3: *Minimum energy positions of the top of a band of crystal on a conical surface of $\theta_p = 5.715°$ ($\theta_{max} = 0.313°$) as calculated from putative global minimum energy structures and a simple band model based on line energies.*

some cases is far from it); the straightness of the edges (similar to the line defects the crystals rarely have straight edges and even if they do they are perpendicular to the cone axis as assumed by the model); and the area of the crystal (this is larger than the approximated value shown in Equation 3.1 as the packing in the band is not perfect). Further, to consider the position of the crystal for other values of ρ, new values for the line defect and edge energies would need to be found from relevant data. Additionally,

the model breaks down when there is no complete crack present in the crystal, so is not directly applicable when any other defect type is present.

3.5 Approximating a Cluster at the Upper Boundary

Further to the above investigations, an attempt was made at approximating the effect of a cluster of particles sitting at the truncated peak of the cone. This was motivated by experimental observations of such a phenomenon by Jessica Sun in the Manoharan Lab at Harvard University. A demonstration of the kind of clustering observed is shown in Figure 3.19.

The presence of a cluster was approximated by introducing a ring of particles around the top of the conical surface. The particles were implemented by introducing a new potential, the sum of a given number of Morse potentials originating at equally spaced points around the top of the cone, in place of the R^{-12} potential described in Section 3.1.3 acting at the upper boundary (the truncated end) of the cone. The potential acting at the bottom of the cone was left unchanged. Due to this implementation, the cluster 'particles' were fixed at $z = h/2$ and could not be moved in the basin-hopping steps. At each step at which the energy and gradient of the energy of the system were calculated, the energy of the ring of Morse particles were added instead of the previously discussed upper R^{-12} boundary potential.

Two distinct cluster-related investigations were carried out. Both used Morse particles with a potential length of $\rho = 18$ to best simulate the real systems.

First, a ring of six regularly spaced Morse particles were placed around the top of the cone. They were spaced at the ideal Morse equilibrium distance from each other, 1.0, at a truncated radius of $r_{\mathrm{t}} = 1.0$. For this investigation, systems of 150 particles were used as the implementation of the ring of particles was more computationally intensive and so computation times increased. Cones of angle $\theta_{\max} = 50°$ through $70°$ were tested to see the effect on the ideal packing at magic angles and on the known defect structures at near-magic angles. Visualisations of the putative global minima are shown in Figure 3.20. It can be seen that the addition of the ring pulls the bulk crystal up to the top of the cone to be in contact with it. It can also be seen that the

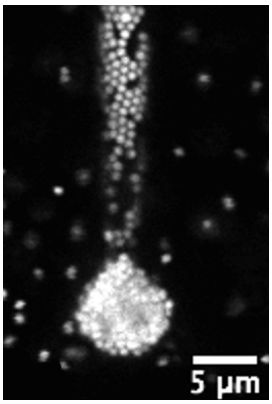

Figure 3.19: *Unpublished light microscopy image of colloidal particles clustering at the tip of a conical surface from work by Jessica Sun in the Manoharan Lab at Harvard University. Used with permission.*

defect structures in the bulk are not greatly affected by the addition of the rings; there is only a change in structure around the top of the cone. Given the rings are horizontal with respect to the vertical axis of the cone, it is not possible for a perfect crystal to be seeded by or incorporate the ring. Hence, some disorder is observed at the top of the bulk crystal where it meets the ring in each case.

Second, the truncation radius of the cone, r_{t}, was varied. Thus the radius of the ring of six particles was also varied, and the effect of changing the spacing between the particles in the ring was investigated. Consider the limiting cases: when the particles have low separation, the shape of the potential at the ring tends to a Morse well around the top boundary, and when the particles have high separation, particles can escape from the cone between them. Neither of these limits could be investigated effectively here due to computational constraints, so ring radii from $r_{\mathrm{t}} = 0.6$ to $r_{\mathrm{t}} = 1.4$ were implemented. Visualisations of the putative global minima are shown in Figure 3.21. A first observation might be that, for all values of r_{t}, the crystal is pulled to the top of the surface and exists in contact with the ring as seen in the first investigation. Second, blue polygons are observed at smaller values of r_{t} and not at higher values. Conversely, red polygons are seen at higher values of r_{t} and not at lower values. The tighter packing of the particles in the ring compared to in the bulk at smaller r_{t} leads to the formation of heptagonal (blue) environments in the bulk crystal, and the looser packing at higher r_{t} does the opposite, creating more pentagonal (red) environments. Lastly, there is

not an observable difference in screening length for the disorder introduced by the ring across the values of r_t investigated here. All of the bulk crystals resolve the non-ideal packing imparted by the ring within one or two particles' environments' width.

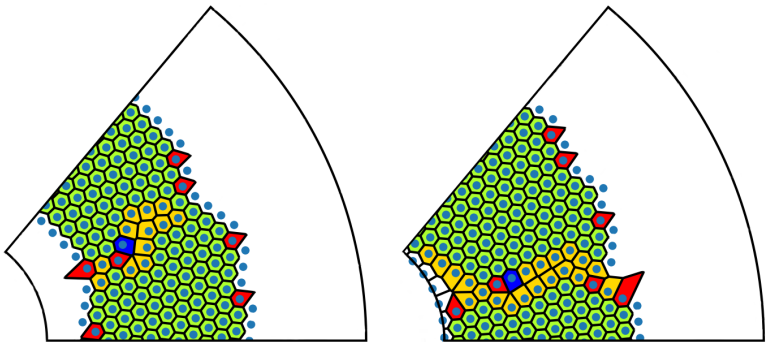

(a) $\theta_{max} = 50°$ *without ring* (b) $\theta_{max} = 50°$ *with ring*

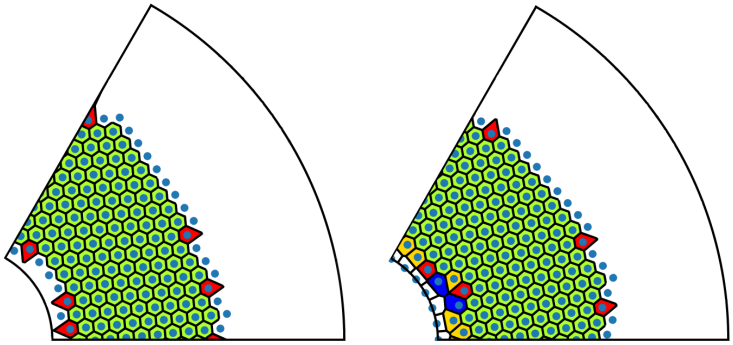

(c) $\theta_{max} = 60°$ *without ring* (d) $\theta_{max} = 60°$ *with ring*

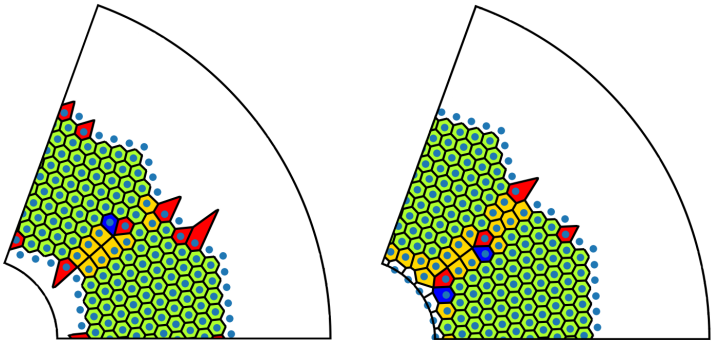

(e) $\theta_{max} = 70°$ *without ring* (f) $\theta_{max} = 70°$ *with ring*

Figure 3.20: *Visualisations of the structures of cones of angles* $\theta_{max} = 50°$, $60°$ *and* $70°$, *all with truncation radius* $r_t = 1.0$, *with and without a ring of six equally spaced particles around the peak. All Morse particles have range of* $\rho = 18$ *and there are 150 particles in each crystal.*

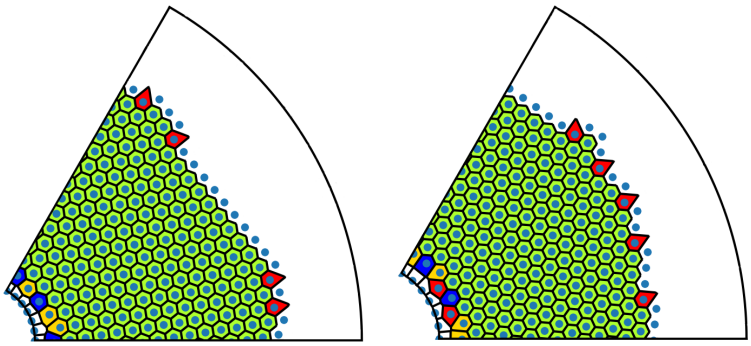

(a) $r_t = 0.6$ (b) $r_t = 0.8$

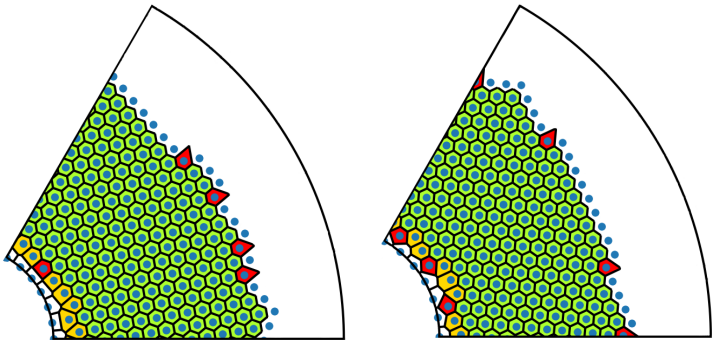

(c) $r_t = 1.0$ (d) $r_t = 1.2$

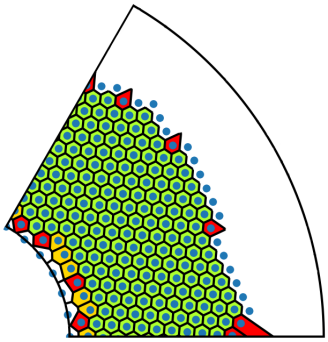

(e) $r_t = 1.4$

Figure 3.21: *Visualisations of the structures of cones of angle $\theta_{max} = 60°$ with a ring of six equally spaced particles around the peak at varying truncation radii r_t. All Morse particles have range of $\rho = 18$ and there are 200 particles in each crystal. Visualisations of $r_t = 0.7, 0.9, 1.1$ and 1.3 are shown in Figure A.3 of Appendix A.2.*

4. Conclusions and Further Work

4.1 Conclusions

This thesis aimed to pursue a general understanding of the packing of two-dimensional crystals on conical surfaces. To do this, minimum energy structures of Morse crystals with a number of different potential ranges on truncated conical surfaces of a range of different dimensions were generated using basin-hopping, a Monte Carlo inspired global energy minimisation technique. Through analysis of the putative global minima of the colloidal crystals, a few key concepts emerged.

The closure constraint: conical surfaces have zero Gaussian curvature and so can in principle host defect-free crystals. The frustration imparted on a crystal by a finite conical surface is not therefore due to the curvature but due to the closure constraint introduced by the finite size of the surface. This is explained by considering the wrapping of the crystal around the cone and onto itself. If the crystal overlaps in a commensurate way, then there is no frustration as seen in crystals on cones of 'magic' net angles of $\theta_{\max} = \frac{n\pi}{3}$, but if the overlap is not commensurate then strain is introduced. This is most clearly seen at intermediate angles of $\theta_{\max} = \frac{(n+1/2)\pi}{3}$.

Defect structures: in this work, many different defect structures were observed at different cone angles and potential ranges. Analysing the the defects seen at small angle and short potential range showed that the defects are introduced to alleviate the strain introduced by the closure constraint by allowing for a rotation in the crystal lattice or by allowing the bond lengths to 'reset' to their preferred, equilibrium length. As the cone angle is increased, different types of defects that relax the strain to different extents appear, and the larger the angle, the higher the defect frequency per unit length of the system. This is to provide the greater relief of stress required at higher angles. In ascending order, edge-terminating helical defects, across-cone wedge defects, bulk

terminating helical defects and up-and-down-cone wedge defects provide increasing levels of strain relief to a crystal. The wedge-shaped defects seen were like those observed in experiment. The bulk-terminating helical defects seen at short potential range and small cone angle are a novel type. Some hybrid defect structures were also observed that appear to be combinations of other defect types. These are double wedges, which present as two connected wedge defects, and L-shaped defects, which present as a combination of a helical defect and a wedge.

Effect of potential range: the range of the potential was observed to affect the defect structures. Generally, longer range potentials spread the strain throughout the structure and shorter range potentials localise it by creating concentrated defect patterns. This is observed in the distribution of particles energies in short and long range potential crystals; short range potential crystals have particles with energies that have discretised, near integer values, whereas long range potential crystals have a continuous range of particle energies. This produces different defect patterns on conical surfaces of a given angle at different potential ranges. It also means that, at a longer potential range, a higher cone angle is required to introduce defects to the structure and also to introduce a full crack through the structure. Furthermore, it is easier to minimise the energies of structures of longer range potential crystals, as the PESs are smoother.

Line energies: the position of a crystal on a conical surface is determined by the energies associated with making its edge and that associated with creating defects in the structure. This has been observed in previous work.[90,91] Here, a preliminary model was presented to model the crystal position using the line energies of the line defect in the crystal and the edges of the crystal, and the behaviour was successfully captured on a qualitative level.

4.2 Further Work

4.2.1 Further and Improved Methods and Analysis

In the small-angle cone studies, it was seen that there are many competing degrees of freedom that all contribute to the energy and structure of the global minimum energy structure at a given angle θ_{p} and potential range ρ which made it difficult to find the

true global minima. This was reflected in the observation of hybrid defects such as L-shaped defects which were combinations of two different defect types. These include the position of the crystal on the surface, the rotation of the crystalline lattice on the surface and the defect type present in the structure (i.e. the way the strain introduced by the non-commensurate overlap is dealt with by the structure). Ideally, some way of separating these degrees of freedom should be introduced. For example, this may be done by seeding certain crystal positions, crystal rotations and defect types. If this were done successfully, then the energy of defect types could be tracked for a given crystal position and rotation, allowing for critical crossover points at which each defect type dominates to be identified.

A better understanding of the structure of the potential energy surfaces of these systems would also contribute to a more complete picture of their behaviour. One way that a structure's PES can be studied is by generating disconnectivity graphs.[118] Disconnectivity graphs map potential energy surfaces by locating local minima and the transition states between them and thus illustrate how easily certain structures can interconvert and whether certain 'classes' of structure exist. Broadly, they can also help in categorising the surfaces as 'glassy' (multiple similar energy funnels) or 'structure-seeker' (single funnel).[118] Disonnectivity graphs have been used in the past to categorise minimum energy states of repulsive colloids on catenoids, unduloids and nodoids as dislocation-dominated or disclination-dominated.[89]

4.2.2 Beyond Structure

In this thesis, we have studied the global minimum energy structures at what is effectively zero temperature. In real systems, the observed behaviours are often influenced by the kinetics of the systems at finite temperature. A complementary study of the time-dependent formation and rearrangement of the crystals could be carried out using molecular dynamics simulations. The location and direction of nucleation and growth on the conical surfaces could affect the type of defects produced and generate structures which are kinetically trapped and not the true lowest energy structures. Kinetically trapped defect structures have been observed on cylindrical surfaces, for example.[127] This is seen in experimental work, where, when nucleation occurs in numerous locations at once, leading to small grain sizes and the overall crystal structure becoming

disordered.[87] This is because each seeded crystal is unlikely to be commensurate when it grows enough to collide with another crystal at a neighbouring site.

4.2.3 More Complex Models

In the model system studied in this thesis, the interaction of the particles with the surface are not considered explicitly. Instead, the particles are just confined to the surface by the way the model is constructed. In reality, the interactions of the particles with the surface do play a role in the behaviour of the system and thus an investigation into the effect of the surface interactions would contribute to a better understanding of real colloidal systems. Further, the assumption of monodispersity was made when constructing the model. This does not reflect real systems, in which particle sizes generally take a range of values. Interestingly, it has been shown that scars form in the arrangement of cells on spherical metazoan epithelia at a number lower than predicted for the Thomson problem and polydispersity has been suggested as a reason for this.[63,78] Thus, investigating polydisperse colloidal crystals, perhaps with some probability distribution of diameters, might help to better replicate the real systems. Another potential route for investigation is the effect of non-spherical particles on the packing. For example, cubic particles want to pack in a square lattice. If the Euler characteristic (as discussed in Section 1.3.1) is considered; a square lattice has an equal number of vertices V and faces F and twice the number of edges as faces, so $E = 2F$, it has an Euler characteristic $\chi = 0$. Thus, a square lattice on a closed, convex surface requires defective packing. It could be assumed that patterns and types of defects that would appear would be different to those observed in the hexagonal lattices studied in this work.

A. Appendices

A.1 An Example Input File

An example input *data* file is shown below. The below *data* file is combined with a *coords* file containing either starting coordinates for the system (if the GTHOMKEEPCOORDS command is present in the datafile), or a blank file with a number of lines corresponding to the number of particles in the system. In that case random starting coordinates are generated. The below file is for a run of $40,000$ basin-hopping steps on a system of Morse particles with $r_0 = 1.0$ and $\rho = 6$ on a cone of $\theta_{\mathrm{p}} = 0.1^{\circ}$ and $r_{\mathrm{t}} = 1.0$ at a fictitious temperature of 1.0. The commands can be found at reference [110] , except for GTHOMKEEPCOORDS which was an addition to the code.

```
GTHOMKEEPCOORDS
GTHOMSON 8 1.039787396934568 1.0 45.59298686956423
GTHOMSONPOT 6 1.0 6.0
SAVE 100
SORT
SLOPPYCONV 0.00001
TIGHTCONV 0.0000001
STEPS 40000 1.0
MAXIT 10000 10000
STEP 0.3
TEMPERATURE 1.0
MAXBFGS 0.01
MAXERISE 1.0D-8
```

A.2 Supplementary Large Angle Images

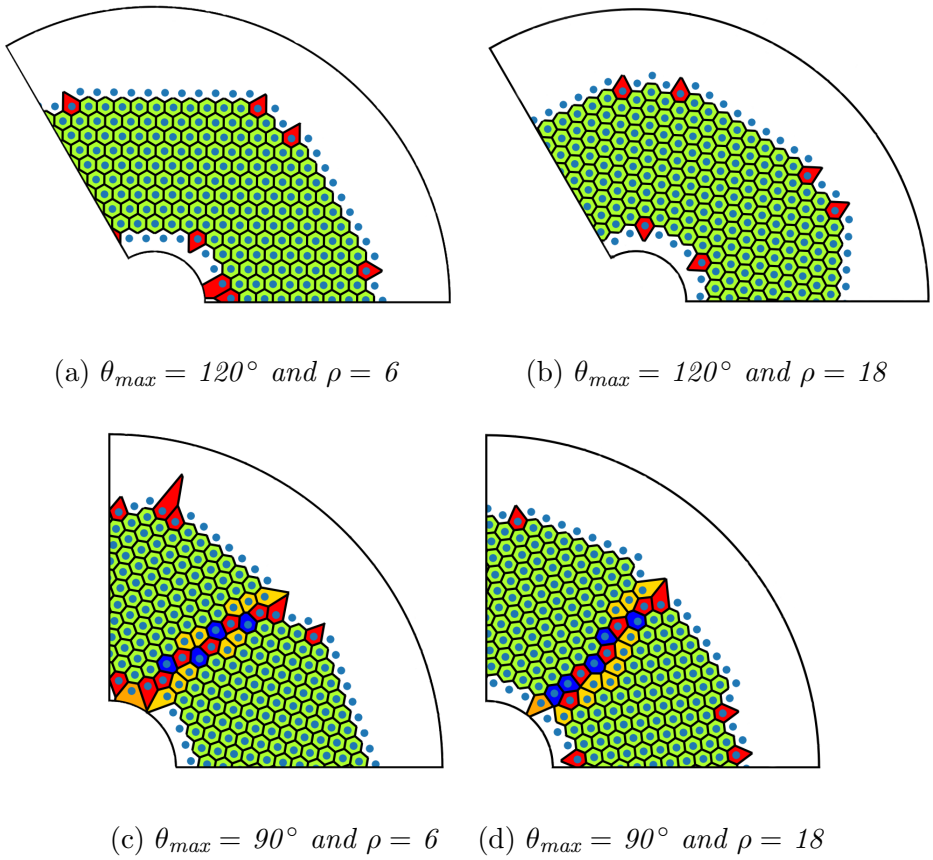

(a) $\theta_{max} = 120°$ *and* $\rho = 6$ (b) $\theta_{max} = 120°$ *and* $\rho = 18$

(c) $\theta_{max} = 90°$ *and* $\rho = 6$ (d) $\theta_{max} = 90°$ *and* $\rho = 18$

Figure A.1: *Visualisations of more structures of minimum energy crystals on cones of* $\theta_{max} = 120°$ *and* $\theta_{max} = 90°$ *with potential ranges of* $\rho = 6$ *and* $\rho = 18$*. Each crystal has 200 particles and each surface has truncation radius* $r_t = 1.0$ *and area* $A = 292.1681168$*.*

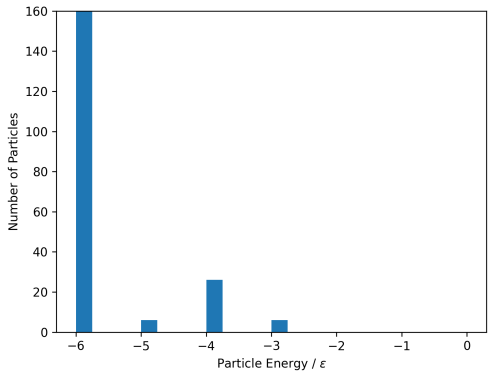

(a) $\theta_{max} = 120°$ *and* $\rho = 6$

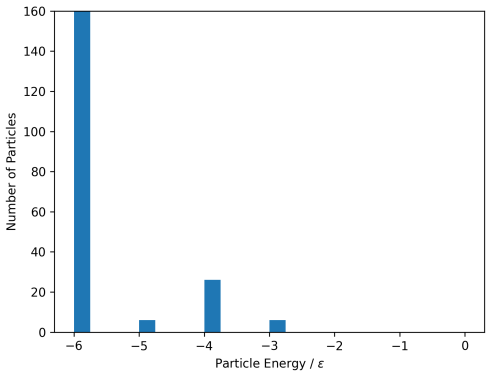

(b) $\theta_{max} = 120°$ *and* $\rho = 18$

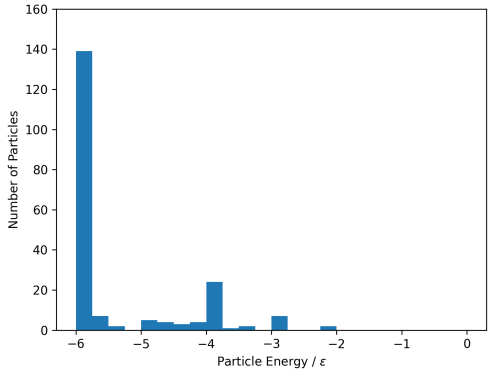

(c) $\theta_{max} = 90°$ *and* $\rho = 6$

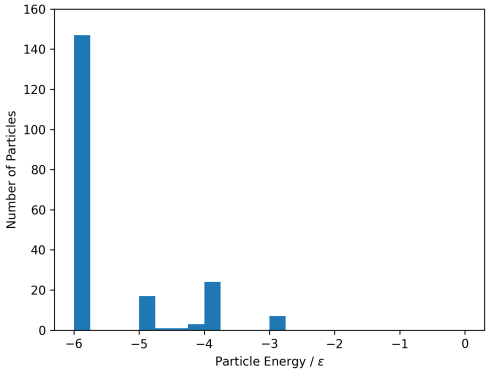

(d) $\theta_{max} = 90°$ *and* $\rho = 18$

Figure A.2: *Histograms of particle energies in the global minimum energy crystals on magic and intermediate angle conical surfaces of* $\theta_{max} = 120°$ *and* $90°$*, all with truncation radius* $r_t = 1.0$ *with potential range* $\rho = 6$ *and* $\rho = 18$*.*

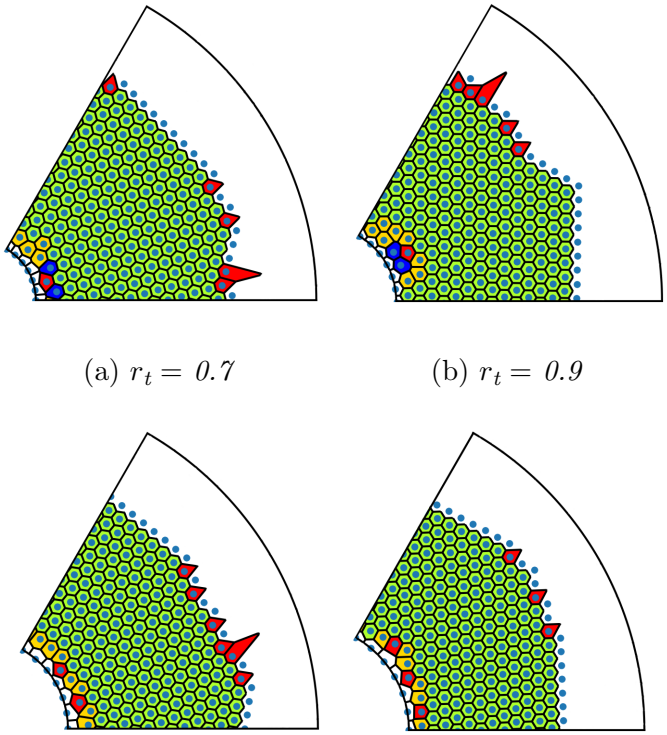

(a) $r_t = 0.7$ (b) $r_t = 0.9$

(c) $r_t = 1.1$ (d) $r_t = 1.3$

Figure A.3: *Visualisations of more structures of minimum energy crystals on cones of angles $\theta_{max} = 60°$, with a ring of equally spaced particles around the peak at varying truncation radii r_t. Each crystal is made of 200 particles with Morse potential range of $\rho = 18$ and sits on a surface of area $A = 292.1681168$.*

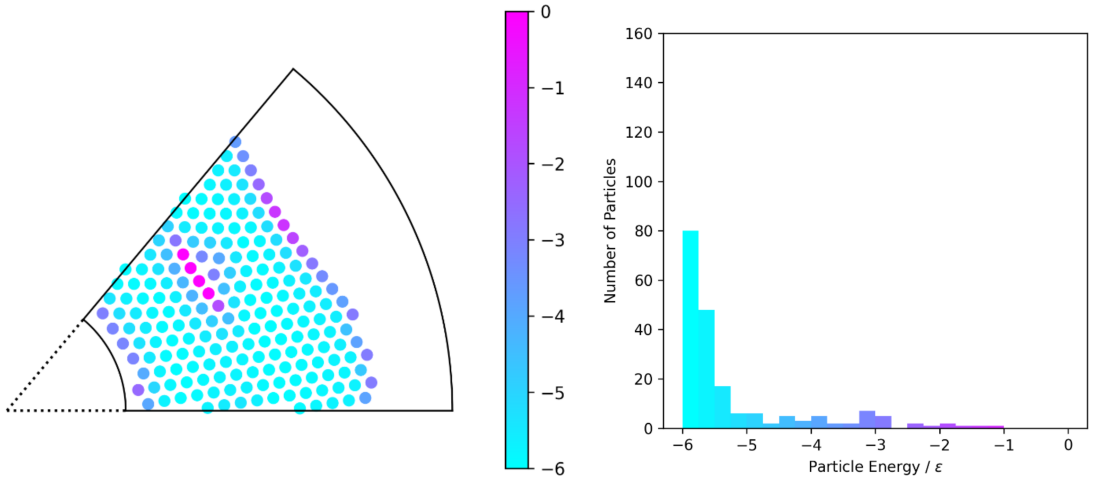

(a) $\theta_{max} = 50°$ *and* $\rho = 6$

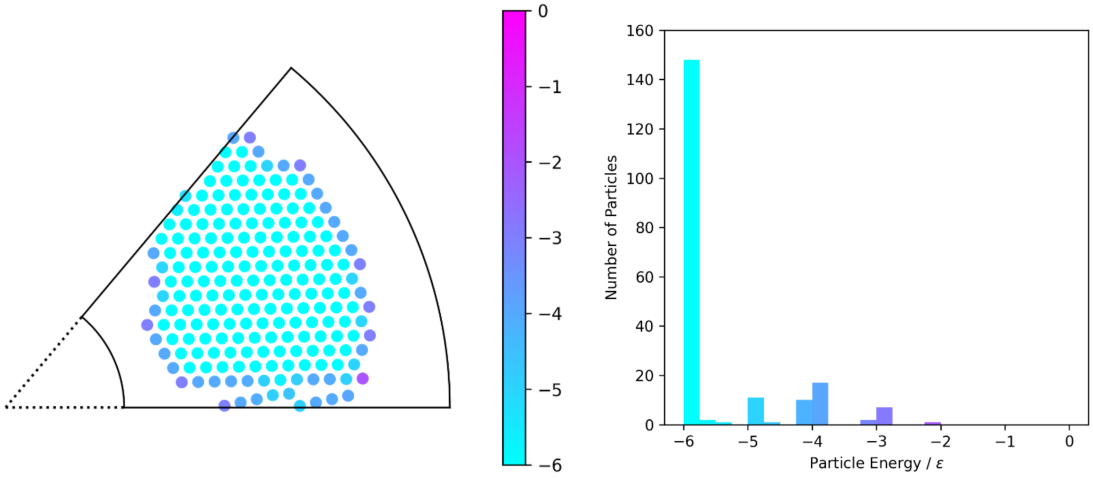

(b) $\theta_{max} = 50°$ *and* $\rho = 18$

Figure A.4: *Visualisations of structures of minimum energy crystals on cones of angles* $\theta_{max} = 50°$. *Each crystal is made of 200 particles and sits on a surface of area* $A = 292.1681168$. *The particles are coloured according to their energy, with the colour map illustrated on the accompanying colour bars and histograms.*

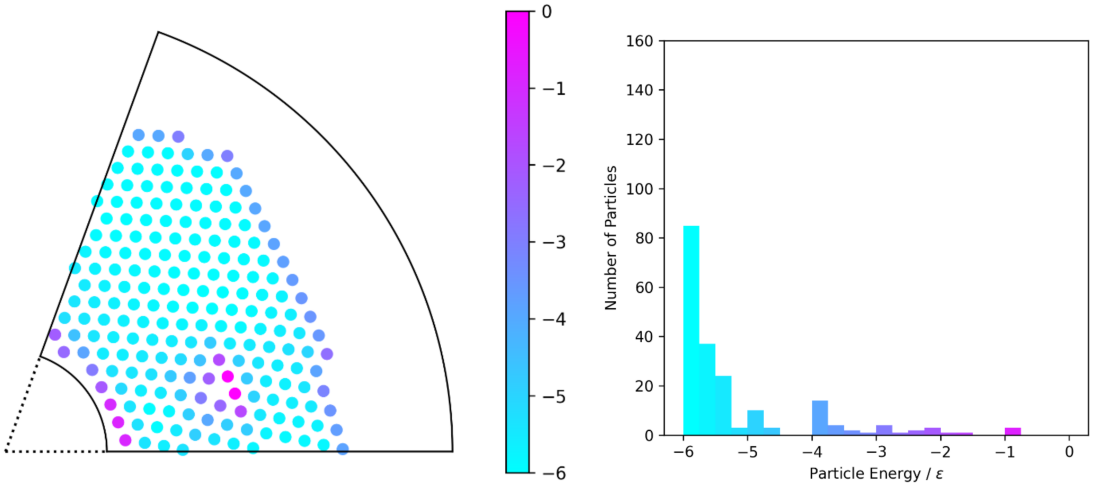

(a) $\theta_{max} = 70^\circ$ *and* $\rho = 6$

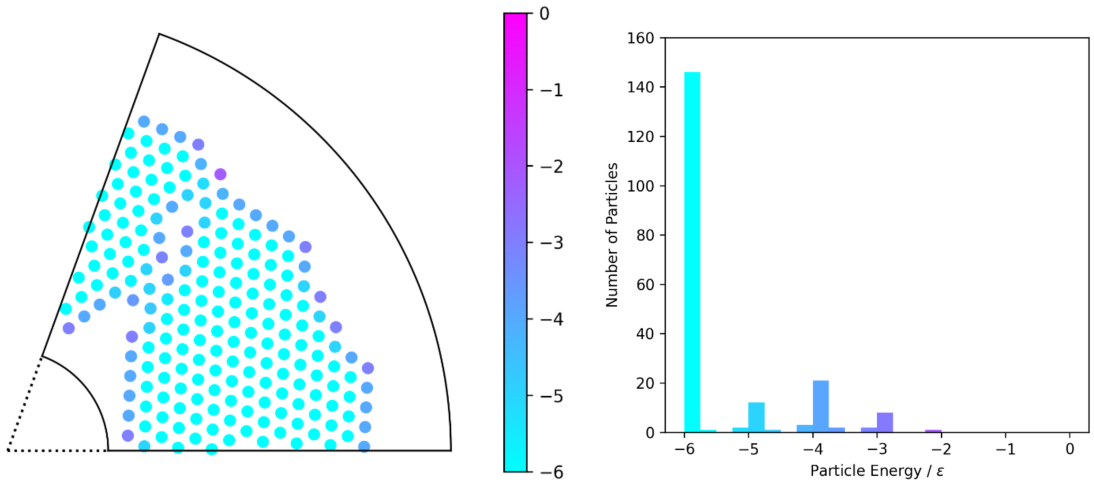

(b) $\theta_{max} = 70^\circ$ *and* $\rho = 18$

Figure A.5: *Visualisations of structures of minimum energy crystals on cones of angles* $\theta_{max} = 70^\circ$. *Each crystal is made of 200 particles and sits on a surface of area* $A = 292.1681168$. *The particles are coloured according to their energy, with the colour map illustrated on the accompanying colour bars and histograms.*

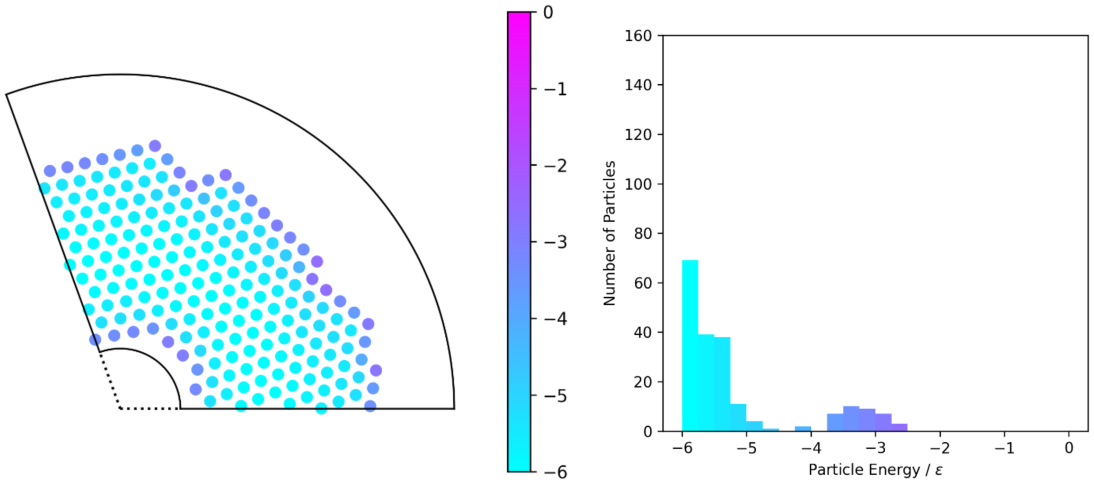

(a) $\theta_{max} = 110°$ *and* $\rho = 6$

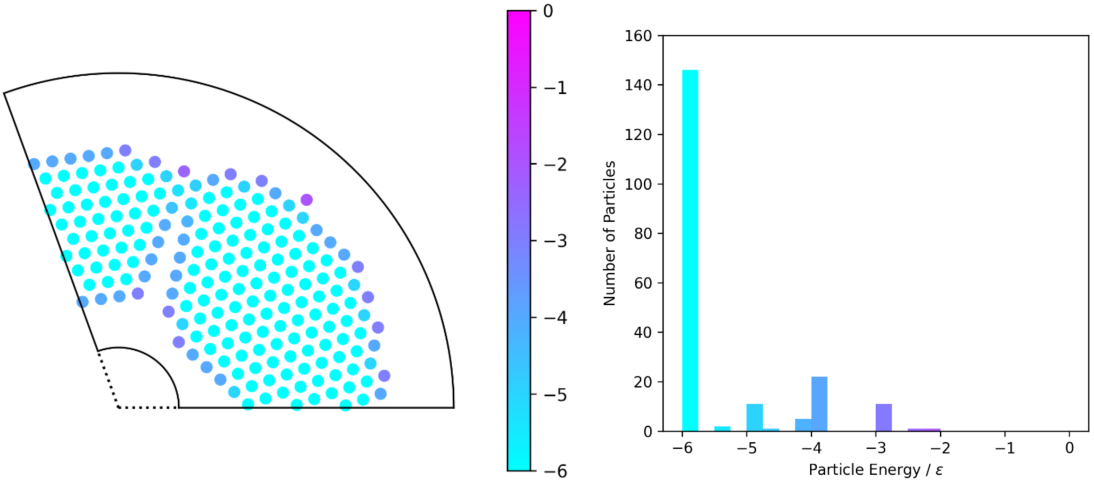

(b) $\theta_{max} = 110°$ *and* $\rho = 18$

Figure A.6: *Visualisations of structures of minimum energy crystals on cones of angles* $\theta_{max} = 110°$. *Each crystal is made of 200 particles and sits on a surface of area* $A = 292.1681168$. *The particles are coloured according to their energy, with the colour map illustrated on the accompanying colour bars and histograms.*

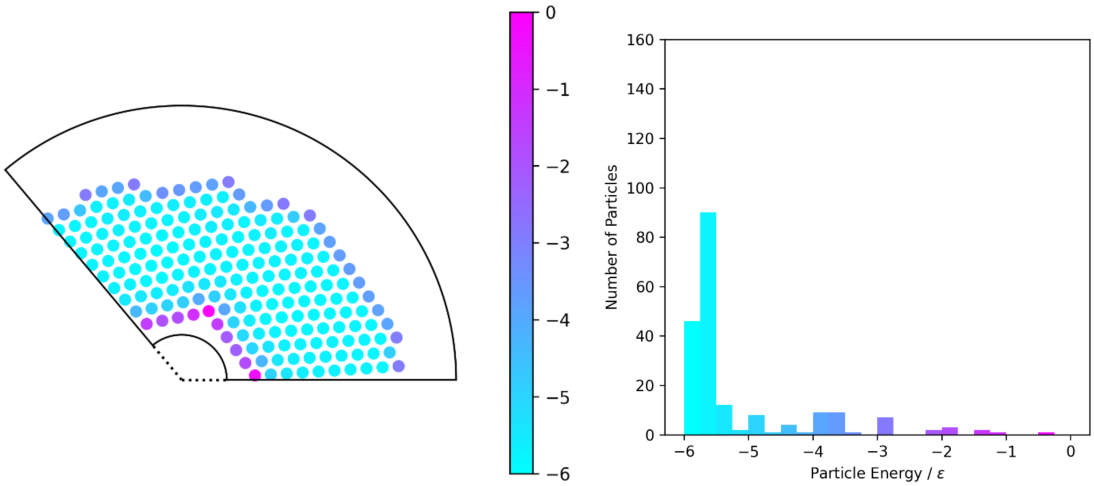

(a) $\theta_{max} = 130°$ *and* $\rho = 6$

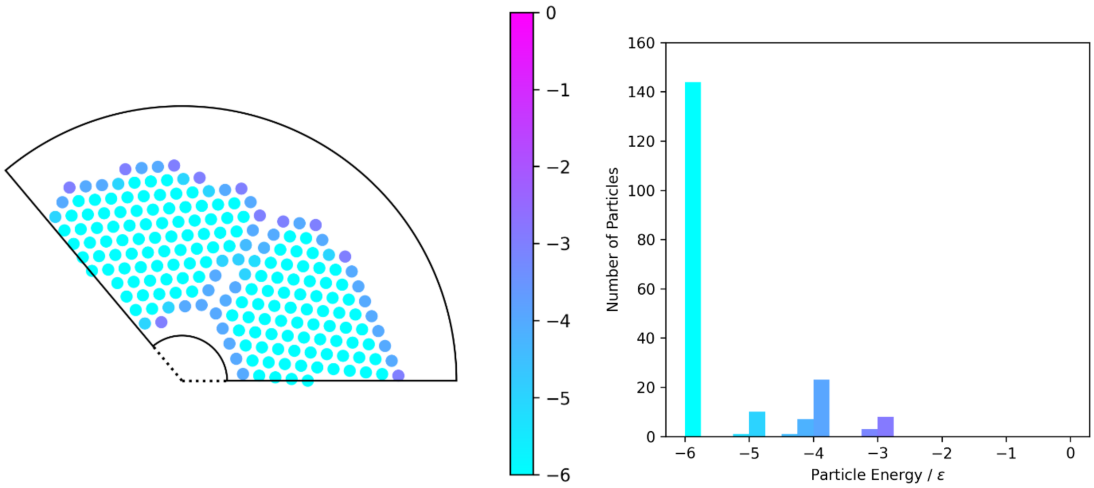

(b) $\theta_{max} = 130°$ *and* $\rho = 18$

Figure A.7: *Visualisations of structures of minimum energy crystals on cones of angles* $\theta_{max} = 130°$. *Each crystal is made of 200 particles and sits on a surface of area* $A = 292.1681168$. *The particles are coloured according to their energy, with the colour map illustrated on the accompanying colour bars and histograms.*

A.3 Defect Types and Categorisation Decision Tree

1. Does the biggest defect contain more than 1 particle? If Yes go to 2, if No then DEFECT TYPE 1

2. Is the number of neighbouring chains in the defect 0, 1, or more than 1? If 0 then DEFECT TYPE 1, if 1 go to 3, if more than 1 go to 10

3. Are the numbers of red and blue polygons each greater than 2? If Yes go to 4, if No go to 6

4. Does the defect span more than half of the available width of the cone? If Yes go to 5, if No then DEFECT TYPE 2

5. Does the defect have an inertia (normalised for particle number) of more than 10? If Yes then DEFECT TYPE 3, if No then DEFECT TYPE 14

6. Do the neighbouring chains have an angle between them of more than 1°? If Yes go to 7, if no go to 8

7. Do the neighbouring chains have angles of more than 135° or less than 45°? If Yes then DEFECT TYPE 4, if No then DEFECT TYPE 5

8. Does the defect contain a dislocation (5/7 polygon pair)? If Yes go to 9, if No then DEFECT TYPE 7

9. Does the defect contain 2 chains only, or more than two chains? If 2 chains then DEFECT TYPE 6, if more than 2 then DEFECT TYPE 13

10. Does the defect contain a dislocation (5/7 polygon pair)? If Yes go to 11, if No go to 12

11. Does the defect span more than half of the available width of the cone? If Yes then DEFECT TYPE 2

12. Is the number of neighbouring chains in the defect 2 or 3? If 2 then go to 13, if 3 then go to 15, if more than three then go to 17

13. Is the largest angle between neighbouring chains between 1 and 10 degrees and smallest less than 1 degree? If Yes go to 14, if No then DEFECT TYPE 10

14. Does the helical part of this defect point up and down or across the cone? If up and down then DEFECT TYPE 8, if across then DEFECT TYPE 9

15. Are the largest and second largest angles between neighbouring chains between 1° and 10° and the smallest less than 1°? If Yes then go to 16

16. Does the helical part of this defect point up and down or across the cone? If up and down then DEFECT TYPE 11, if across then DEFECT TYPE 12

17. Does the defect contain more than 2 dislocations (5/7 polygon pairs)? If Yes then go to 18

18. Does the defect have an inertia (normalised for particle number) of more than 10? If Yes then DEFECT TYPE 3, if No then DEFECT TYPE 14

List of Defect Types:

1. : defect-free crystal
2. : complete crack separating distinct crystals
3. : complete crack up and down cone
4. : simple wedge up and down cone
5. : simple wedge across cone
6. : complete helical defect
7. : edge-terminating helical defect
8. : simple L-shaped hybrid defect - wedge across, helical up and down
9. : simple L-shaped hybrid defect - helical across, wedge up and down
10. : compound double wedge defect
11. : complex L-shaped hybrid defect - double wedge across, helical up and down
12. : complex L-shaped hybrid defect - helical across, double wedge up and down
13. : indeterminate L-shaped hybrid defect - helical up and down, unknown across
14. : amorphous localised defect

A.4 Further Defect Analysis

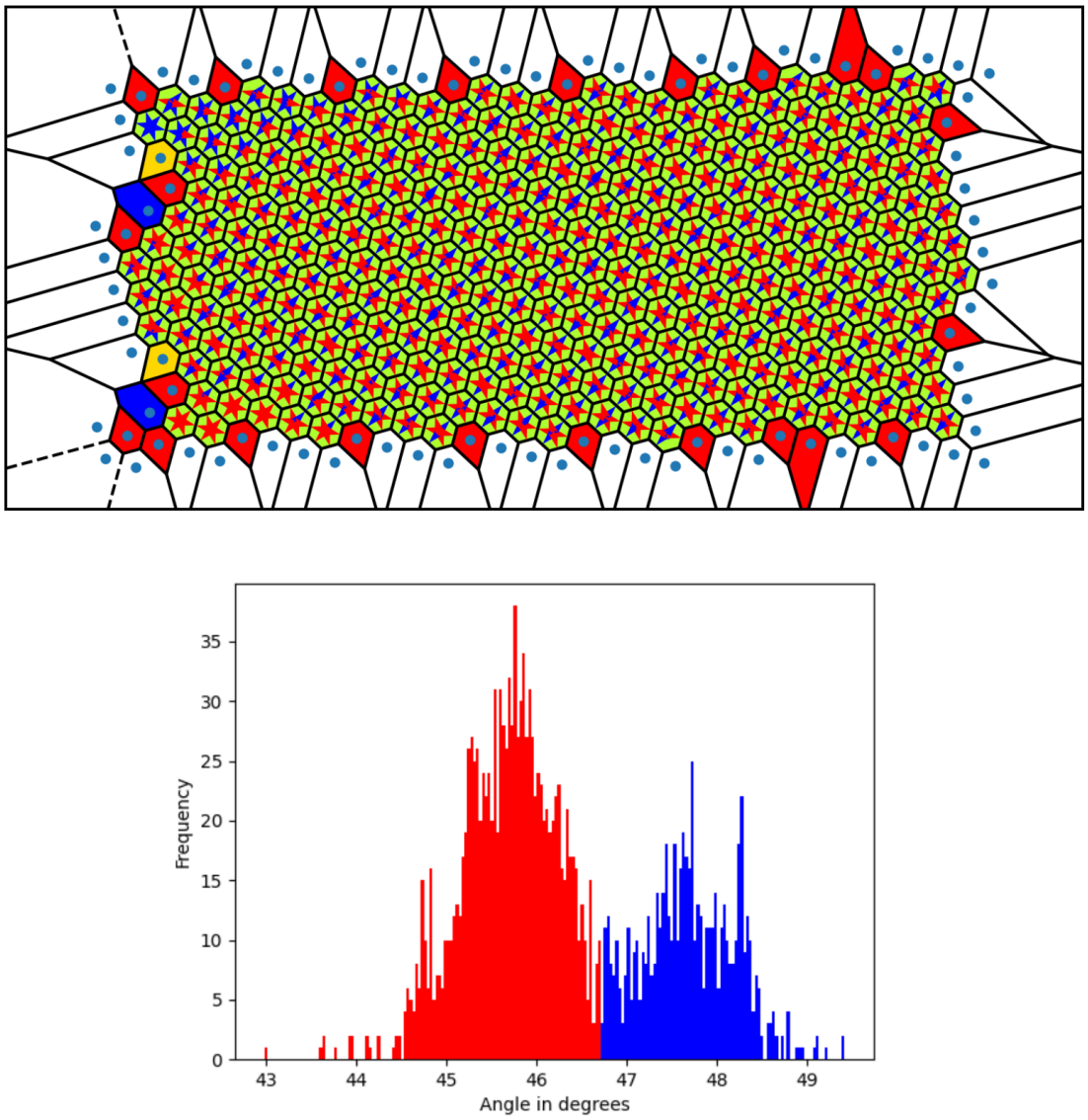

Figure A.8: *A plot of bond vectors in a defect-free crystal observed at $\rho = 18$ and $\theta_p = 0.2°$ ($\theta_{max} = 0.011°$). The accompanying histogram shows the frequency distribution of angles and the chosen colour scheme. Here the angles are measured in a clockwise direction within their 60° sector.*

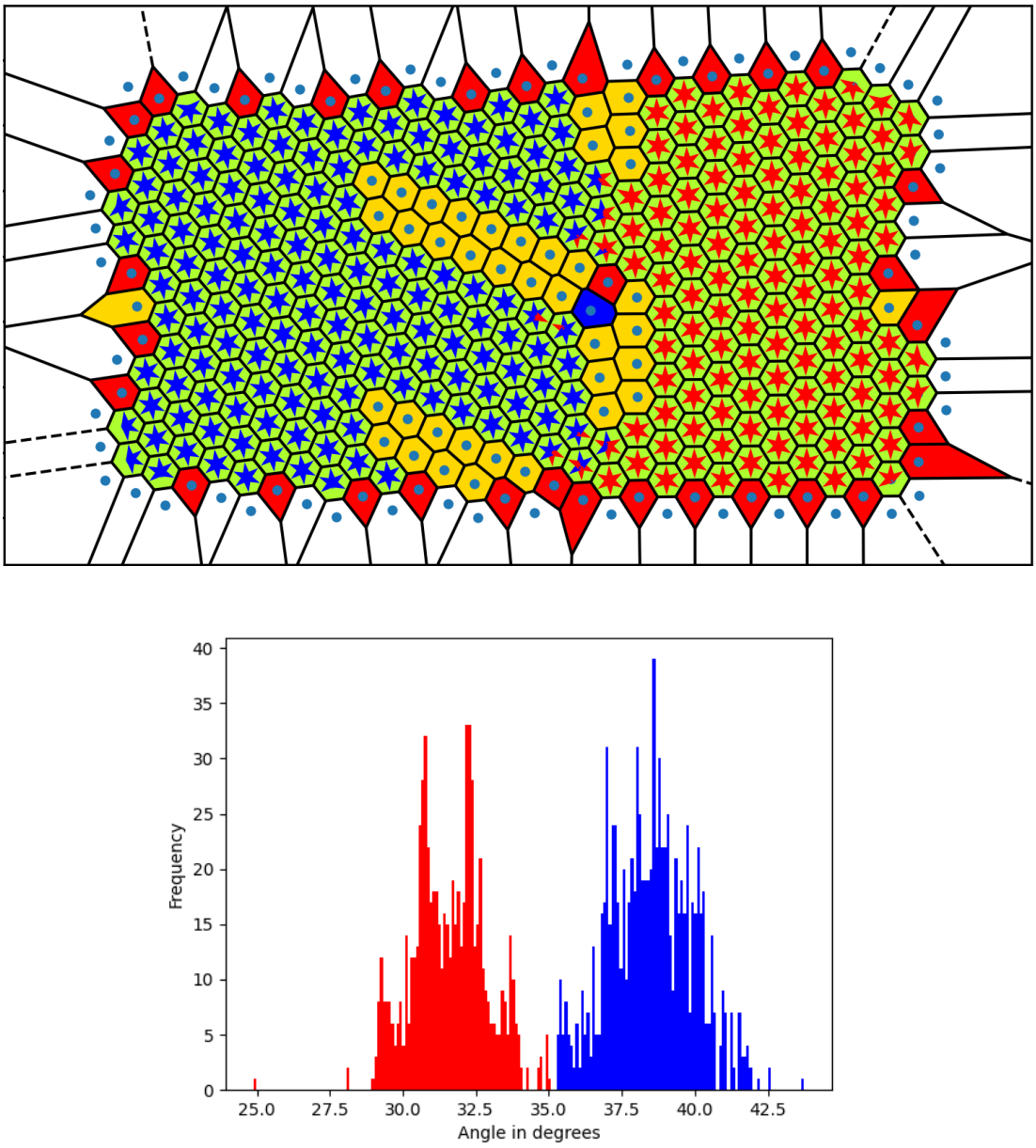

Figure A.9: *A plot of bond vectors in a crystal hosting an L-shaped defect observed at* $\rho = 18$ *and* $\theta_p = 0.5°$ *(*$\theta_{max} = 0.027°$*). The accompanying histogram shows the frequency distribution of angles and the chosen colour scheme. Here the angles are measured in a clockwise direction within their* $60°$ *sector.*

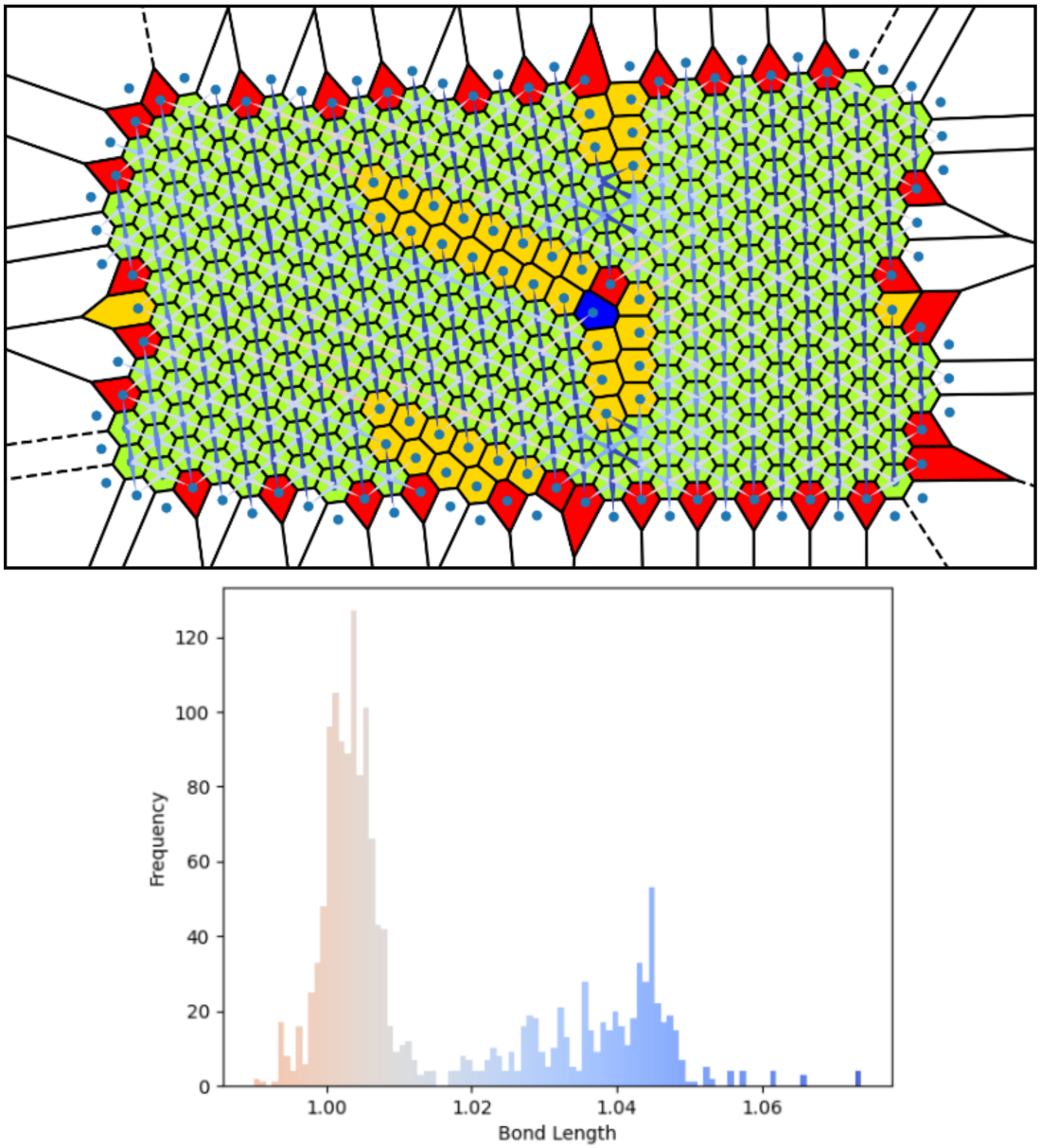

Figure A.10: *A plot of bond lengths in a crystal hosting an L-shaped defect observed at* $\rho = 18$ *and* $\theta_p = 0.5°$ *(*$\theta_{max} = 0.027°$*). The accompanying histogram shows the frequency distribution of bond lengths and the chosen colour scheme.*

A.5 Band Model Derivation 1: Length of Defect

The length L_b of the defect in the model discussed in Section 3.4 and given by Equation 3.2 is derived in this section. The slope length L_b of a band on a cone (i.e. the slope length of a truncated cone) is given by

$$L_\mathrm{b} = L_2 - L_1, \tag{A.1}$$

where L_2 and L_1 are the slope lengths from the apex of the cone to the bottom of the band and the top of the band respectively. The relations between the angle of the cone θ_p and the slope length of the cone L, the radius r and the vertical distance from the apex z at a given point are:

$$\sin\frac{\theta_\mathrm{p}}{2} = \frac{r}{L}, \tag{A.2}$$

$$\cos\frac{\theta_\mathrm{p}}{2} = \frac{z}{L}, \tag{A.3}$$

$$\tan\frac{\theta_\mathrm{p}}{2} = \frac{r}{z}. \tag{A.4}$$

The surface area A of a cone is given by

$$A = \pi r L.$$

and so the area of a band of a cone A_b (a truncated cone) is given by

$$A_\mathrm{b} = \pi r_2 L_2 - \pi r_1 L_1, \tag{A.5}$$

where r_2 and r_1 are the radii at the base of the band and the top of the band respectively. By combining Equation A.2 and Equation A.5, it can be shown that

$$A_\mathrm{b} = \pi L_2 \left(L_2 \sin\frac{\theta_\mathrm{p}}{2} \right) - \pi L_1 \left(L_1 \sin\frac{\theta_\mathrm{p}}{2} \right),$$

which can be rearranged to give

$$A_\mathrm{b} = \pi \sin\frac{\theta_\mathrm{p}}{2} \left(L_2^2 - L_1^2 \right) \tag{A.6}$$

and thus

$$A_\mathrm{b} = \pi \sin\frac{\theta_\mathrm{p}}{2} (L_2 - L_1)(L_2 + L_1).$$

Now, if Equation A.3 rearranged for L and Equation A.1 are substituted in, it can be shown that

$$A_{\mathrm{b}} = \pi \sin\frac{\theta_{\mathrm{p}}}{2} L_{\mathrm{b}} \left(\frac{z_2}{\cos\frac{\theta_{\mathrm{p}}}{2}} + \frac{z_1}{\cos\frac{\theta_{\mathrm{p}}}{2}} \right),$$

and thus

$$L_{\mathrm{b}} = \frac{A_{\mathrm{b}}}{\pi \sin\frac{\theta_{\mathrm{p}}}{2} \left(\frac{z_2}{\cos\frac{\theta_{\mathrm{p}}}{2}} + \frac{z_1}{\cos\frac{\theta_{\mathrm{p}}}{2}} \right)}. \tag{A.7}$$

To remove the dependence on z_2, z_2 as a function of z_1 and band area A_{b} must be found. By starting with Equation A.6 and by substituting in Equation A.3, it can be shown that

$$A_{\mathrm{b}} = \pi \sin\frac{\theta_{\mathrm{p}}}{2} \left[\left(\frac{z_2}{\cos\frac{\theta_{\mathrm{p}}}{2}} \right)^2 - \left(\frac{z_1}{\cos\frac{\theta_{\mathrm{p}}}{2}} \right)^2 \right]$$

which in turn can be rearranged for z_2

$$z_2 = \sqrt{\frac{A_{\mathrm{b}} \cos\frac{\theta_{\mathrm{p}}}{2}}{\pi \tan\frac{\theta_{\mathrm{p}}}{2}} + z_1^2}. \tag{A.8}$$

When substituted into Equation A.7 and z_1 is replaced by z_{t} (the vertical distance from the cone apex to the top of the crystal band), after rearrangement, this gives the result in Equation 3.2:

$$L_{\mathrm{b}} = \frac{A_{\mathrm{b}}}{\pi \tan\frac{\theta_{\mathrm{p}}}{2} \left[z_{\mathrm{t}} + \sqrt{\frac{A_{\mathrm{b}} \cos\frac{\theta_{\mathrm{p}}}{2}}{\pi \tan\frac{\theta_{\mathrm{p}}}{2}} + z_{\mathrm{t}}^2} \right]}.$$

A.6 Band Model Derivation 2: Length of Edges

The length L_c of the edges of the crystal band in the model discussed in Section 3.4 and given by Equation 3.3 is derived in this section. At a given distance z from the apex of cone of angle θ_p down its axis of rotation at which the radius of the cone is r, the circumference of the cone C is given by

$$C = 2\pi r$$

and thus, by combining the above equation and Equation A.4, it can be shown that

$$C = 2\pi z \tan\frac{\theta_p}{2}. \tag{A.9}$$

The total edge length of a band on the cone is given by

$$L_c = C_1 + C_2,$$

where C_1 and C_2 are the circumference of the cone at the top and the bottom of the band respectively. Hence, by substituting in Equation A.9, it can be shown that

$$L_c = 2\pi z_1 \tan\frac{\theta_p}{2} + 2\pi z_2 \tan\frac{\theta_p}{2},$$

where z_1 and z_2 are the vertical distance of top and bottom of the band from the apex of the cone respectively. After rearranging the above equation to

$$L_c = 2\pi \tan\frac{\theta_p}{2}(z_1 + z_2),$$

substituting in Equation A.8 and replacing z_1 with z_t gives the result in Equation 3.3:

$$L_c = 2\pi \tan\frac{\theta_p}{2}\left[z_t + \sqrt{\frac{A_b \cos\frac{\theta_p}{2}}{\pi \tan\frac{\theta_p}{2}} + z_t^2}\right].$$

Bibliography

[1] B. Antonny, *Annual Review of Biochemistry*, 2011, **80**, 101–123.

[2] H. Strahl, S. Ronneau, B. S. González, D. Klutsch, C. Schaffner-Barbero and L. W. Hamoen, *Nature Communications*, 2015, **6**, 8728.

[3] I. K. Jarsch, F. Daste and J. L. Gallop, *Journal of Cell Biology*, 2016, **214**, 375–387.

[4] H. T. McMahon and E. Boucrot, *Journal of Cell Science*, 2015, **128**, 1065–1070.

[5] E. Beltrán-Heredia, V. G. Almendro-Vedia, F. Monroy and F. J. Cao, *Frontiers in Physiology*, 2017, **8**, 312.

[6] G. J. Doherty and H. T. McMahon, *Annual Review of Biochemistry*, 2009, **78**, 857–902.

[7] T. E. Aktepe and J. M. Mackenzie, *Cellular Microbiology*, 2018, **20**, 1–10.

[8] T. Baumgart, S. Hess and W. Webb, *Nature*, 2003, **425**, 821–824.

[9] H. Y. Lou, W. Zhao, Y. Zeng and B. Cui, *Accounts of Chemical Research*, 2018, **51**, 1046–1053.

[10] G. Chang, R. H. Spencer, A. T. Lee, M. T. Barclay and D. C. Rees, *Science*, 1998, **282**, 2220–2226.

[11] A. Koçer, M. Walko, W. Meijberg and B. L. Feringa, *Science*, 2005, **309**, 755–758.

[12] Y. Wei, T. Tang and H. B. Pang, *Nature Communications*, 2019, **10**, 3646.

[13] K. He, Y. Wei, Z. Zhang, H. Chen, B. Yuan, H. B. Pang and K. Yang, *Nanoscale*, 2021, **13**, 9626–9633.

[14] K. Charalambous, P. J. Booth, R. Woscholski, J. M. Seddon, R. H. Templer, R. V. Law, L. M. C. Barter and O. Ces, *Journal of the American Chemical Society*, 2012, **134**, 5746–5749.

[15] E. A. Kim and A. H. Castro Neto, *Europhysics Letters*, 2008, **84**, 57007.

[16] F. Guinea, M. I. Katsnelson and M. A. H. Vozmediano, *Physical Review B - Condensed Matter and Materials Physics*, 2008, **77**, 1–8.

[17] S. Iijima, *Nature*, 1991, **354**, 56–58.

[18] J. W. Mintmire and C. T. White, *Carbon*, 1995, **33**, 893–902.

[19] J. P. Lu, *Physical Review Letters*, 1995, **74**, 1123–1126.

[20] G. Ouyang, C. X. Wang and G. W. Yang, *Chemical Reviews*, 2009, **109**, 4221–4247.

[21] C. Xu, B. Zhang, A. C. Wang, H. Zou, G. Liu, W. Ding, C. Wu, M. Ma, P. Feng, Z. Lin and Z. L. Wang, *ACS Nano*, 2019, **13**, 2034–2041.

[22] G. M. Whitesides and B. A. Grzybowski, *Science*, 2002, **295**, 2418–2421.

[23] V. Vitelli, J. B. Lucks and D. R. Nelson, *Proceedings of the National Academy of Sciences of the United States of America*, 2006, **103**, 12323–12328.

[24] J. Zhan, Y. Cai, S. He, L. Wang and Z. Yang, *Angewandte Chemie*, 2018, **130**, 1831–1834.

[25] V. N. Manoharan, *Science*, 2015, **349**, 1253751.

[26] C. Cummins, R. Lundy, J. J. Walsh, V. Ponsinet, G. Fleury and M. A. Morris, *Nano Today*, 2020, **35**, 100936.

[27] D. A. Walker, E. K. Leitsch, R. J. Nap, I. Szleifer and B. A. Grzybowski, *Nature Nanotechnology*, 2013, **8**, 676–681.

[28] O. D. Velev, *Nature Nanotechnology*, 2013, **8**, 620–621.

[29] F. Li, D. P. Josephson and A. Stein, *Angewandte Chemie - International Edition*, 2011, **50**, 360–388.

[30] O. Kruglova, P. J. Demeyer, K. Zhong, Y. Zhou and K. Clays, *Soft Matter*, 2013, **9**, 9072–9087.

[31] Nature, *Subjects: Colloids*, 2021, `https://www.nature.com/subjects/colloids`.

[32] P. Pawel, *Contemporary Physics*, 1983, **24**, 25–73.

[33] J. K. G. Dhont, *An Introduction to Dynamics of Colloids*, Elsevier Ltd., Amsterdam, the Netherlands, 1st edn., 1996.

[34] D. Frenkel, *Science*, 2002, **296**, 65–66.

[35] T. Hueckel, G. M. Hocky and S. Sacanna, *Nature Reviews Materials*, 2021, 1–17.

[36] B. Peng, H. R. Vutukuri, A. van Blaaderen and A. Imhof, *Journal of Materials Chemistry*, 2012, **22**, 21893–21900.

[37] F. Dekker, R. Tuinier and A. P. Philipse, *Colloids and Interfaces*, 2018, **2**, 44.

[38] S. Sacanna, W. T. M. Irvine, P. M. Chaikin and D. J. Pine, *Nature*, 2010, **464**, 575–578.

[39] M. Jitianu and D. V. Goia, *Journal of Colloid and Interface Science*, 2007, **309**, 78–85.

[40] C. C. Ho, A. Keller, J. A. Odell and R. H. Ottewill, *Colloid Polymer Science*, 1993, **271**, 469–479.

[41] K. V. Edmond, T. W. P. Jacobson, J. S. Oh, G.-R. Yi, A. D. Hollingsworth, S. Sacanna and D. J. Pine, *Soft Matter*, 2021, **17**, 6176–6181.

[42] D. Joshi, D. Bargteil, A. Caciagli, J. Burelbach, Z. Xing, A. S. Nunes, D. E. P. Pinto, N. A. M. Araújo, J. Brujic and E. Eiser, *Science Advances*, 2016, **2**, e1600881.

[43] F. M. Peeters and X. Wu, *Physical Review A*, 1987, **35**, 3109–3114.

[44] K. N. Pham, A. M. Puertas, J. Bergenholtz, S. U. Egelhaaf, A. Moussaïd, P. N. Pusey, A. B. Schofield, M. E. Cates, H. Fuchs and W. C. Poon, *Science*, 2002, **296**, 104–106.

[45] M. E. Leunissen, C. G. Christova, A. P. Hynninen, C. P. Royall, A. I. Campbell, A. Imhof, M. Dijkstra, R. Van Roij and A. Van Blaaderen, *Nature*, 2005, **437**, 235–240.

[46] E. Bianchi, R. Blaak and C. N. Likos, *Physical Chemistry Chemical Physics*, 2011, **13**, 6397–6410.

[47] Y. Wang, Y. Wang, D. R. Breed, V. N. Manoharan, L. Feng, A. D. Hollingsworth, M. Weck and D. J. Pine, *Nature*, 2012, **491**, 51–55.

[48] F. Liang, B. Liu, Z. Cao and Z. Yang, *Langmuir*, 2018, **34**, 4123–4131.

[49] H. Cong, B. Yu, J. Tang, Z. Li and X. Liua, *Chemical Society Reviews*, 2013, **42**, 7774–7800.

[50] E. Greenfield, J. Nemirovsky, R. El-Ganainy, D. N. Christodoulides and M. Segev, *Optics Express*, 2013, **21**, 23785.

[51] Q. Yan, *Crystals Special Issue: Colloidal Crystals*, 2016, `https://www.mdpi.com/journal/crystals/special_issues/colloidal_crystals`.

[52] T. Ding, K. Song, K. Clays and C.-h. Tung, *Advanced Materials*, 2009, **9**, 1936–1940.

[53] A. Stein, B. E. Wilson and S. G. Rudisill, *Chemical Society Reviews*, 2013, **42**, 2763–2803.

[54] H. Munakata, K. Yoshima and K. Kanamura, *IOP Conference Series: Materials Science and Engineering*, 2011, **18**, 8–12.

[55] S. Auer and D. Frenkel, *Nature*, 2001, **409**, 1020–1023.

[56] J. L. Harland and W. V. Megen, *Physical Review E*, 1997, **55**, 3054–3067.

[57] P. N. Pusey and W. van Megen, *Nature*, 1986, **320**, 340–342.

[58] U. Gasser, C. Eisenmann, G. Maret and P. Keim, *ChemPhysChem*, 2010, **11**, 963–970.

[59] J. D. Joannopoulos, S. G. Johnson, J. N. Winn and R. D. Meade, *Photonic Crystals: Molding the Flow of Light*, Princeton University Press, Princeton, New Jersey, USA, 2nd edn., 2008.

[60] Y. Li, J. Jun-Yan Suen, E. Prince, E. M. Larin, A. Klinkova, H. Thérien-Aubin, S. Zhu, B. Yang, A. S. Helmy, O. D. Lavrentovich and E. Kumacheva, *Nature Communications*, 2016, **7**, 12520.

[61] D. Ebert, *Mediterranean Mandarin Oranges in a Box at La Boqueria Market in Barcelona, Spain*, 2021, `https://www.encirclephotos.com/image/mediterranean-mandarin-oranges-in-a-box-at-la-boqueria-market-in-barcelona-spain`

[62] J. J. Thomson, *The London, Edinburgh, and Dublin Philosophical Magazine and Journal of Science*, 1904, **7**, 237–265.

[63] D. S. Roshal, K. Azzag, E. Le Goff, S. B. Rochal and S. Baghdiguian, *Scientific Reports*, 2020, **10**, 1–11.

[64] D. L. D. Caspar and A. Klug, *Cold Spring Harbor Symposia on Quantitative Biology*, 1962, **27**, 1–24.

[65] L. E. Perotti, S. Dharmavaram, W. S. Klug, J. Marian, J. Rudnick and R. F. Bruinsma, *Physical Review E*, 2016, **94**, 1–16.

[66] T. Yoshino, A. Matsuoka, T. Kurihara, N. Ishida, N. Kishimoto, K. Kimoto and S. Matsuura, *Forma*, 2012, **27**, 45–53.

[67] H. W. Kroto, J. R. Heath, S. C. O'Brien, R. F. Curl and R. E. Smalley, *Nature*, 1985, **318**, 162–163.

[68] P. W. Fowler, S. Nikolić, R. De Los Reyes and W. Myrvold, *Physical Chemistry Chemical Physics*, 2015, **17**, 23257–23264.

[69] V. Vadakkumbatt, E. Joseph, A. Pal and A. Ghosh, *Nature Communications*, 2014, **5**, 1–6.

[70] S. Smale, *The Mathematical Intelligencer*, 1998, **20**, 7–15.

[71] N. N. Andreev, *East Journal on Approximations*, 1996, **2**, 459.

[72] W. L. Miller and A. Cacciuto, *Soft Matter*, 2011, **7**, 7552–7559.

[73] L. Euler, *Novi Commentarii academiae scientiarum Petropolitanae*, 1758, **4**, 109–149.

[74] W. T. M. Irvine, V. Vitelli and P. M. Chaikin, *Nature*, 2010, **468**, 947–951.

[75] A. R. Bausch, M. J. Bowick, A. Cacciuto, A. D. Dinsmore, M. F. Hsu, D. R. Nelson, M. G. Nikolaides, A. Travesset and D. A. Weitz, *Science*, 2003, **299**, 1716–1718.

[76] T. Einert, P. Lipowsky, J. Schilling, M. J. Bowick and A. R. Bausch, *Langmuir*, 2005, **21**, 12076–12079.

[77] P. Lipowsky, M. J. Bowick, J. H. Meinke, D. R. Nelson and A. R. Bausch, *Nature Materials*, 2005, **4**, 407–411.

[78] D. J. Wales and S. Ulker, *Physical Review B - Condensed Matter and Materials Physics*, 2006, **74**, 1–4.

[79] M. J. Bowick, A. Cacciuto, D. R. Nelson and A. Travesset, *Physical Review B - Condensed Matter and Materials Physics*, 2006, **73**, 1–16.

[80] M. J. Bowick, D. R. Nelson and A. Travesset, *Physical Review B - Condensed Matter and Materials Physics*, 2000, **62**, 8738–8751.

[81] G. Meng, J. Paulose, D. R. Nelson and V. N. Manoharan, *Science*, 2014, **343**, 634–637.

[82] Annon201, *M. deliciosa fruit growing*, 2008, `https://en.wikipedia.org/wiki/Monstera_deliciosa`.

[83] E. Pairam, H. Le and A. Fernández-Nieves, *Physical Review E - Statistical, Nonlinear, and Soft Matter Physics*, 2014, **90**, 1–4.

[84] A. M. J. Edwards, É. R. Gutiérrez, M. I. Newton, G. Mchale, G. G. Wells, R. L. Aguilar and C. V. Brown, *Scientific Reports*, 2021, **11**, 8120.

[85] I. B. Liu, N. Sharifi-Mood and K. J. Stebe, *Annual Review of Condensed Matter Physics*, 2018, **9**, 283–305.

[86] R. D. Gillette and D. C. Dyson, *Chemical Engineering*, 1970, **2**, 44–54.

[87] J. Sun and V. N. Manoharan, *Unpublished Work*, 2021.

[88] K. R. Mangipudi, V. Radisch, L. Holzer and C. A. Volkert, *Ultramicroscopy*, 2016, **163**, 38–47.

[89] H. Kusumaatmaja and D. J. Wales, *Physical Review Letters*, 2013, **110**, 165502.

[90] J. O. Law, *PhD Thesis*, Durham University, 2020.

[91] J. O. Law, J. M. Dean, M. A. Miller and H. Kusumaatmaja, *Soft Matter*, 2020, **16**, 8069–8077.

[92] Z. Fazli and A. Naji, *Physical Review E*, 2021, **103**, 022601.

[93] D. A. Wood, C. D. Santangelo and A. D. Dinsmore, *Soft Matter*, 2013, **9**, 10016–10024.

[94] A. Luque, D. Reguera, A. Morozov, J. Rudnick and R. F. Bruinsma, *Journal of Chemical Physics*, 2012, **136**, 184507.

[95] N. Tanjeem, W. H. Wilkin, D. A. Beller, C. H. Rycroft and V. N. Manoharan, *ACS Applied Nano Materials*, 2021, **4**, 10682–10691.

[96] Z. Li and H. A. Scheraga, *Proceedings of the National Academy of Sciences of the United States of America*, 1987, **84**, 6611–6615.

[97] D. J. Wales and J. P. K. Doye, *Journal of Physical Chemistry A*, 1997, **101**, 5111–5116.

[98] G. Meng, N. Arkus, M. P. Brenner and V. N. Manoharan, *Science*, 2010, **327**, 560–563.

[99] J. C. Crocker, *Science*, 2010, **327**, 535–536.

[100] A. Malins, S. R. Williams, J. Eggers, H. Tanaka and C. P. Royall, *Journal of Physics Condensed Matter*, 2009, **21**, 5103.

[101] J. Taffs, A. Malins, S. R. Williams and C. P. Royall, *Journal of Physics Condensed Matter*, 2010, **22**, 4119.

[102] F. Calvo, J. P. K. Doye and D. J. Wales, *Nanoscale*, 2012, **4**, 1085–1100.

[103] D. J. Wales, *ChemPhysChem*, 2010, **11**, 2491–2494.

[104] J. M. C. Marques and F. B. Pereira, *Journal of Molecular Liquids*, 2015, **210**, 51–63.

[105] J. W. R. Morgan and D. J. Wales, *Nanoscale*, 2014, **6**, 10717–10726.

[106] D. J. Wales and H. A. Scheraga, *Science*, 1999, **285**, 1368–1372.

[107] D. J. Wales, *Energy Landscapes: Applications to Clusters, Biomolecules and Glasses*, Cambridge University Press, Cambridge, United Kingdom, 1st edn., 2003.

[108] N. Metropolis, *Los Alamos Science*, 1987, **15**, 125–130.

[109] J. Dongarra and F. Sullivan, *Computing in Science and Engineering*, 2000, **2**, 22–23.

[110] E. P. Lafortune, *PhD Thesis*, Katholieke Universiteit Leuven, 1996.

[111] P. P. Boyle, *Journal of Financial Economics*, 1977, **4**, 323–338.

[112] N. Metropolis, A. W. Rosenbluth, M. N. Rosenbluth, A. H. Teller and E. Teller, *The Journal of Chemical Physics*, 1953, **21**, 1087–1092.

[113] S. Kirkpatrick, C. D. Gelatt, Jr. and M. P. Vecchi, *Science*, 1983, **220**, 671–680.

[114] M. C. Prentiss, D. J. Wales and P. G. Wolynes, *Journal of Chemical Physics*, 2008, **128**, 5106.

[115] D. J. Wales, M. A. Miller and T. R. Walsh, *Nature*, 1998, **394**, 758–760.

[116] D. J. Wales, J. P. K. Doye, A. Dullweber, M. P. Hodges, F. Y. Naumkin, F. Calvo, J. Hernández-Rojas and T. F. Middleton, *The Cambridge Cluster Database*, `http://www-wales.ch.cam.ac.uk/CCD.html`.

[117] D. J. Wales and Wales Group University of Cambridge Department of Chemistry, *GMIN Software Package*, `http://www-wales.ch.cam.ac.uk/GMIN/`.

[118] M. A. Miller, J. P. Doye and D. J. Wales, *Journal of Chemical Physics*, 1999, **110**, 328–334.

[119] G. Voronoy, *Journal für die Reine und Angewandte Mathematik*, 1908, **133**, 97–178.

[120] G. Voronoy, *Journal für die Reine und Angewandte Mathematik*, 1908, **134**, 198–287.

[121] Airbus, *Getting to grips with ETOPS*, 1998, `https://www.737ng.co.uk/AIRBUSETOPSGuide.pdf`.

[122] Victoria State Government, *School Zones*, 2020, `https://www.education.vic.gov.au/parents/going-to-school/Pages/zones-restrictions.aspx`.

[123] The Gold Coast Home of the Arts, *HOTA Precinct*, `https://hota.com.au/hota-precinct/`.

[124] P. Virtanen, R. Gommers, T. E. Oliphant, M. Haberland, T. Reddy, D. Cournapeau, E. Burovski, P. Peterson, W. Weckesser, J. Bright, S. J. van der Walt, M. Brett, J. Wilson, K. J. Millman, N. Mayorov, A. R. J. Nelson, E. Jones, R. Kern, E. Larson, C. Carey, I. Polat, Y. Feng, E. W. Moore, J. VanderPlas, D. Laxalde, J. Perktold, R. Cimrman, I. Henriksen, E. A. Quintero, C. R. Harris, A. M. Archibald, A. H. Ribeiro, F. Pedregosa, P. van Mulbregt and SciPy 1.0 Contributors, *Nature Methods*, 2020, **17**, 261–272.

[125] J. D. Hunter, *Computing in Science and Engineering*, 2007, **9**, 90–95.

[126] C. B. Barber, D. P. Dobkin and H. T. Huhdanpaa, *ACM Transactions on Mathematical Software*, 1996, **22**, 469–483.

[127] N. Tanjeem, W. H. Wilkin, D. A. Beller, C. H. Rycroft and V. N. Manoharan, *Unpublished Work*, 2020.

Note: All webpages were last accessed on 27/09/2021